ENTRANCE EFFECTS ON SOLUTION TRANSPORT THROUGH NANOPOROUS MEMBRANES

A THESIS PRESENTED
BY
Daniel J. Rankin
TO
THE SCHOOL OF PHYSICAL SCIENCES

IN PARTIAL FULFILLMENT OF THE REQUIREMENTS
FOR THE DEGREE OF
MASTER OF PHILOSOPHY
IN CHEMICAL SCIENCE

THE UNIVERSITY OF ADELAIDE
ADELAIDE, SOUTH AUSTRALIA
April 2019

DECLARATION

I certify that this work contains no material which has been accepted for the award of any other degree or diploma in my name in any university or other tertiary institution and, to the best of my knowledge and belief, contains no material previously published or written by another person, except where due reference has been made in the text. In addition, I certify that no part of this work will, in the future, be used in a submission in my name for any other degree or diploma in any university or other tertiary institution without the prior approval of the University of Adelaide and where applicable, any partner institution responsible for the joint award of this degree.

I give consent to this copy of my thesis when deposited in the University Library, being made available for loan and photocopying, subject to the provisions of the Copyright Act 1968.

I also give permission for the digital version of my thesis to be made available on the web, via the University's digital research repository, the Library Search and also through web search engines, unless permission has been granted by the University to restrict access for a period of time.

ADELAIDE, SOUTH AUSTRALIA, April 2019

Daniel J. Rankin

ABSTRACT

Solution transport across nanoporous membranes occurs in many different biologically and industrially relevant processes such as filtration of waste by the kidneys and desalination of seawater. The same theoretical framework can be used to understand both of these processes, as well as many others. In general, a flux of solution is driven across a porous membrane due to an externally applied force. This external force can be a gradient in pressure, temperature, concentration, or electrical potential. At the entrance and exit of a pore the fluid streamlines and electric field lines experience a significant constriction in going from the bulk reservoirs to the narrow pores. This effect can become significant for short pores and pores with low friction and thus must be appropriately taken into account to correctly predict solution fluxes.

In the first study, continuum mechanics is used to investigate the entrance effects on charge flux of electrolytes across porous membranes. The access electrical resistance, which is the electrical resistance associated with the electric field lines bending into and out of the pores, has previously been shown to make up a significant fraction of the total electrical resistance when the fluid–pore friction is low.[1] Although several papers have studied the access electrical resistance,[2–5] none has explicitly considered the effect of surface charge on the surfaces of the membrane facing the bulk solution even though this charge has been shown to have a significant effect on the access electrical resistance.[6] In this thesis, finite element method (FEM) calculations are carried out in order to systematically study the access electrical resistance of charged pores in charged and uncharged membranes. The results are compared with predictions from two existing continuum-based theories and a new theory derived in this thesis. It is found that the FEM results agree with different theories depending on whether or not the outer-membrane surface is charged.

In the second study an existing molecular dynamics (MD) algorithm is used to simulate concentration differences across pores connected to bulk reservoirs. The algorithm is found to require a modification at high solute concentrations, which had not previously been considered.

In the third study the modified MD algorithm is used to investigate possible non-continuum and non-ideal effects on concentration-gradient-driven flows at high solute concentrations. Entrance effects are considered in the context of diffusio-osmotic flows, which are flows driven by forces acting on the inhomogeneous fluid layer near the membrane pore surfaces as a result of an applied concentration gradient. The access diffusio-osmotic resistance, which is the resistance to the diffusio-osmotic flux associated with the fluid streamlines bending into and out of the pores, is calculated and compared with a new theory that is derived in this thesis. The assumptions made in deriving the new theory include, amongst others a dilute solution and continuum theory. Despite these assumptions, the theory predicts the correct scaling of the MD results at two different high solute concentrations.

It is found that both electrical and diffusio-osmotic access resistances can be separated from their respective total (access and pore) resistances. Depending on whether the length scales of interest, such as the pore radius, are comparable with the pore length, the access resistance can be a significant factor in determining the total resistance of the system. This is explored in this thesis in the context of both electrical and diffusio-omsotic resistance, which affect a wide range of different systems.

ACKNOWLEDGMENTS

I acknowledge the great help and support that I have received from my supervisor, A/Prof. David M Huang. He has helped me to communicate my ideas clearly in writing by giving guidance on grammar and typography. He has also helped me to develop my research skills by thinking about the physical origins of my problems, and being systematic in my approach to research. In particular, I would like to acknowledge David's work in helping me to derive the necessary equations for this thesis.

I would also like to acknowledge the loving support of my wife, Mrs. Amy Louise Rankin. She has been a source of endless support and encouragement. She has cooked meals for me, and has kept the house beautiful and clean. Furthermore, she kept encouraging me all the way to the end. I am very grateful for her support!

My family has also been a huge support emotionally throughout the process of carrying out the research and writing the thesis. It is great to have so many people who love me and care for me.

Lastly, I would like to thank God for helping me through the whole process. I had often prayed to him for help and he heard me. He is my strength and my shield.

CONTENTS

LIST OF TABLES

ACRONYMS

DCV-GCMD   Dual control volume grand canonical molecular dynamics

EDL   Electric double layer

FEM   Finite element method

GCMC   Grand canonical Monte Carlo

MD   Molecular dynamics

NVE   Microcanonical ensemble

PBC   Periodic boundary condition

PDE   Partial differential equation

PNPS   Poisson–Nernst–Planck–Stokes

PUT   Profile-unbiased thermostat

INTRODUCTION

1.1 SIGNIFICANCE OF SOLUTION TRANSPORT

Solution transport processes occur in a wide range of natural and artificial systems such as cell membranes,[8] kidneys,[9] and membranes for desalination and filtration.[10] In kidneys, urea waste is filtered from water and salt, while in desalination, salt is filtered from water. Both of these processes require energy to produce gradients in electrolyte concentration. Conversely, energy can be produced by mixing solutions of different electrolyte concentration. As an example, this form of energy is harvested in electric eels (*Electrophorus electricus*) to defend themselves and subdue prey.[11] Electrolyte concentration gradients are a source of chemical potential energy. They can be created with an input of energy or converted to different forms of energy. Natural systems are typically more efficient at converting different forms of energy to chemical potential energy than synthetic systems. For example, kidneys reclaim water from waste using 30 times less energy than is required in desalination.[12] These natural systems could be mimicked to build next generation membranes for desalination, filtration, and energy harvesting, which may help to solve some of the world's biggest problems, such as depleting potable water resources,[13] and increasing pollution due to reliance on fossil fuels.[14] Understanding how solutions are transported in both natural and artificial systems is the key to improving membrane-based technologies. One of the barriers to improving these technologies is the significant resistance to solution transport that is encountered at the entrance and exit of the membrane pores.[2,3,7,15–17] This occurs due to the dramatic transition between the bulk solution and the confined fluid within the membrane pores.[17] In this thesis, solution transport phenomena will be examined with a focus on entrance effects, which refer to the effect of both the entrance and the exit of the membrane pores. It is the hope that this knowledge will be used by experimentalists to improve our technology, environment, and quality of life.

1.2 THEORY OF SOLUTION TRANSPORT

All of the processes mentioned above involve the transport of solutions across porous membranes in response to applied forces. For most types of solutions, in general, the forces can be gradients in pressure p, solute concentration c, or electrical potential ϕ (Figure 1.1).[1,18] A gradient in pressure causes solutions to flow from regions of high to low pressure.[19] Similarly, osmotic flows are driven by the osmotic pressure difference arising from different solute concentrations on either side of the membrane.[9,20] When the solute is adsorbed or depleted at the surface of the membrane pores, a secondary flow occurs due to an osmotic–pressure difference that develops within the interfacial fluid layer near the pore surface, in a process known as diffusio-osmosis.[21] For pressure-driven flows, osmosis, and diffusio-osmosis, the solute does not need to be charged.[20,22,23] However, in order for a flow to occur due to an electrical potential gradient (electro-osmosis) the solute must be charged.[24,25]

1.2.1 *Fluid flux: bulk vs surface phenomena*

The most intuitive way to drive a flow of fluid is by applying a pressure gradient. This acts as an internal force on the fluid, which drives it from regions of high to low pressure. Pressure gradients can either be applied mechanically (eg. using a piston), or by using a
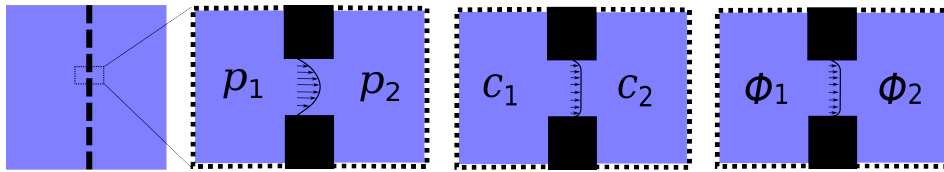
Figure 1.1: Forces driving solution flow through porous membranes. The flows through the pores are driven by differences in pressure p, concentration c, or electrical potential ϕ.
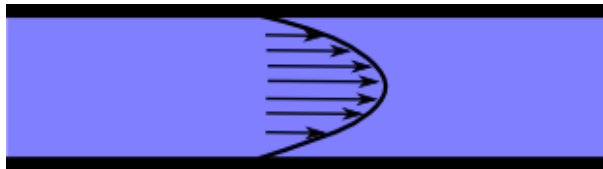
Figure 1.2: Bulk flow profile inside membrane pore.
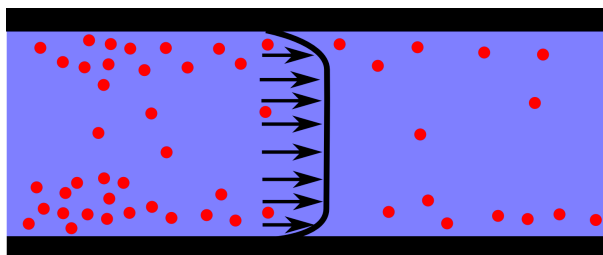
Figure 1.3: In the presence of a concentration gradient, fluid is transported across a pore that has a net solute adsorption (or depletion) at its surface. Due to the inhomogeneity in the fluid at the pore surfaces, an osmotic pressure gradient develops parallel to the wall within the interfacial fluid layer near the surface due to an applied concentration difference. The pressure near the surface is larger at the high concentration side of the surface than at the low concentration side. The difference in pressure along this region pushes the solute, along with the solvent, down the concentration gradient. If there is a net solute depletion then the flow generally reverses.

solute concentration gradient (osmosis). In each case the forces act on the bulk fluid within the pore, which results in a parabolic flow profile (Figure 1.2).[26]

Flows may also be driven by forces acting on the fluid near the pore surfaces, where there are inhomogeneities in solute concentration. These include diffusio-osmosis[23,27,28] and electro-osmosis.[29] Diffusio-osmosis occurs when a concentration gradient is applied across a porous membrane that has a net solute adsorption or depletion at the surface of the membrane pores.[28] Figure 1.3 illustrates diffusio-osmosis. In this diagram, there is a net solute adsorption at the pore surfaces. When a concentration gradient is imposed across the pore, an osmotic pressure gradient develops within the interfacial fluid layer, which drives the fluid through the pore.[23] When the solute is charged, a flow may also be driven by an electric field.[17] Figure 1.4 shows the fluid near the surface for an electrolyte near a charged surface. Due to different interactions of the ions with the surface, the counter-ions (ions of opposite charge to the surface) and co-ions (ions of the same charge as the surface) differ in concentration from the bulk electrolyte far from the pore surfaces. If an electrical potential difference is applied across the pore then a flow arises due to electro-osmosis. Electro-osmosis works by the electric field acting on the predominance of counter-ions close to the pore surfaces.[29] In both diffusio-osmosis and electro-osmosis, the flows are driven by forces acting on the fluid near the pore surfaces. Therefore, they have a characteristically plug-like flow profile[30] (Figure 1.5), with the length scale on which the flow profile varies near the interface related to the length scale on which the solute concentration profile varies.[31]
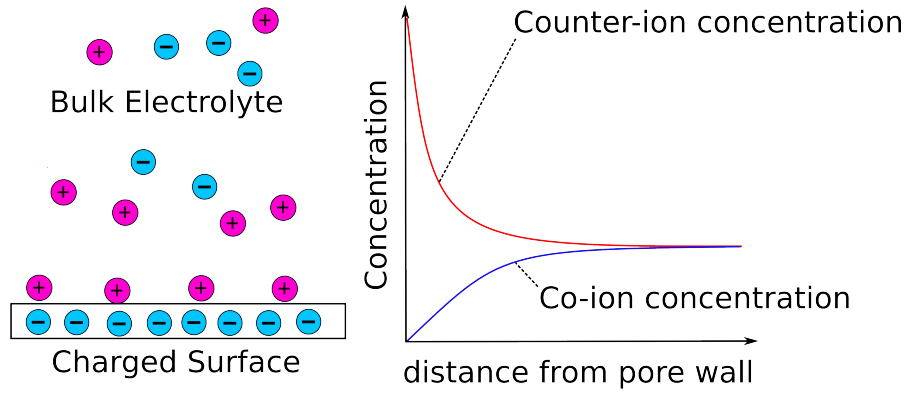
Figure 1.4: Ion distribution away from charged pore wall.
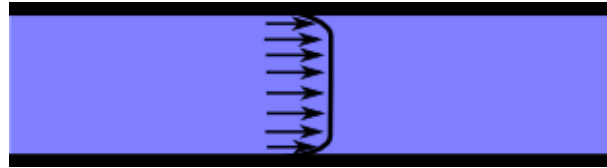
Figure 1.5: Surface-driven flow profile inside membrane pore.

1.2.2 *Solute flux*

When solvents flow through nanoporous membranes, solutes are also transported along with them.[32] Solutes are transported by diffusion down a concentration gradient, convection with the solution, and migration in an electric field (charged solutes only).[33] Figure 1.6 illustrates these different mechanisms of solute transport for a binary electrolyte. In the diagram, both a concentration gradient and an electrical potential gradient are present across the membrane, which drives a flux of solution. In this case there will be a flux of solute due to diffusion, migration in an electric field, and convection.

1.2.3 *Entrance effects*

Both solutes and solvents experience a resistance as they travel through a pore.[34] There is resistance to the fluxes within the pore, which is called the pore resistance, and at the pore entrances, which is called the access resistance.[35] The pore resistance occurs due to viscous frictional, and electrostatic forces acting on the fluid by the pore walls. It is typically significant for long pores and can become negligible for short pores.[36] In contrast, the access
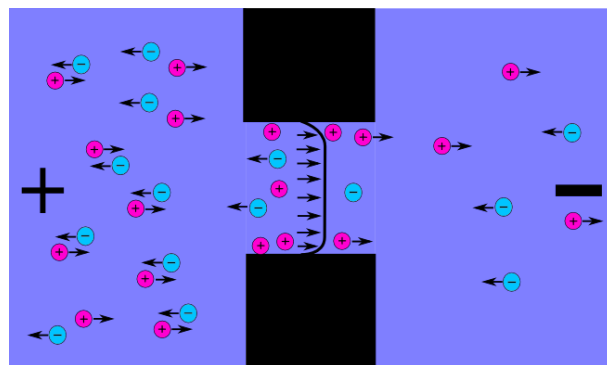
Figure 1.6: Mechanisms of ion flux through nanopores. Ions flow from regions of high to low concentration due to the concentration gradient, the applied electric field, and due to convection with the solvent.
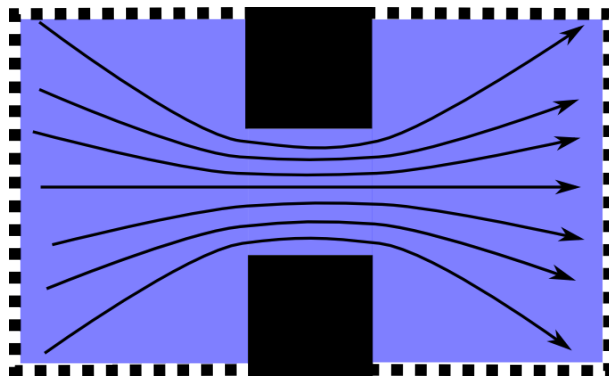
Figure 1.7: Diagram showing fluid streamlines/electric field lines bending into and out of a pore connected to bulk reservoirs.

resistance occurs due to the fluid streamlines and electric field lines bending into and out of the narrow pore from the bulk reservoirs (Figure 1.7).[17,37,38] By definition it does not depend on the length of the pore so it becomes the limiting resistance for short pores[15,17] and pores with low friction (such that the pore resistance is negligible).[1,37] Note well that the separation of the pore and access resistances from the total resistance is an assumption.

1.2.3.1 *Access electrical resistance*

The access electrical resistance is the electrical resistance (resistance to electrical current carried by the solution) encountered at the pore entrance and exit.[2] In 1975 it was considered by Hall[3] to be the convergence resistance from a hemispherical electrode at infinity to an equipotential disk covering the pore surface. The theory by Hall is often used to describe the access electrical resistance.[1,37,39,40] However, it does not take into account surface charge, which is known to affect the access electrical resistance.[6,7,16]

Lee et al.[7] derived an equation for the access electrical resistance of a charged pore. However, this equation was obtained heuristically, and has not been tested systematically against numerical calculations. The derivation did not make any assumptions about the surface charge on the surfaces of the membrane facing the bulk reservoirs, which is known to reduce the access electrical resistance relative to the predictions using the theory by Hall.[6,16]

1.2.3.2 *Access diffusio-osmotic resistance*

Not much is known about the access diffusio-osmotic resistance, being the resistance to diffusio-osmotic flow encountered at the entrance and exit of a pore. However, a similar quantity has been known since the 1800s. In 1891, Sampson[41] calculated the pressure-driven solution flux through a circular orifice in an infinitesimally thin membrane. This has since been used to describe the access hydrodynamic resistance to a pore.[15,37,42–50] However, there is currently no equation to describe the access resistance due to diffusio-osmotic flux.

1.3   CONTINUUM MODELLING OF SOLUTION TRANSPORT

At the scale of a few nanometres or more, it has been found that solution transport phenomena may be adequately described under the continuum assumption, which treats the fluid as a continuous medium.[51]

In the continuum assumption the motion of fluids in response to forces is governed by the laws of fluid mechanics. These are derived from the law of conservation of mass and Newton's second law, which relates the force F to the mass m and acceleration a through the formula $F = ma$. The Navier–Stokes equations relate the external and internal forces on the fluid to its velocity. This assumes that the fluid is a continuous medium and that

molecular effects can be ignored. This is a reasonable assumption at low Knudsen numbers, being the ratio of the molecular interaction length scale to the characteristic length of the system.[52] By this definition the length scale at which continuum hydrodynamics breaks down for liquid water is $\sim 3\,nm$.[52]

For an electrolyte the flow equations may also be coupled with equations for the electrical potential and salt concentration, in which it is generally assumed that the ions are uncorrelated point particles that interact only through electrostatic forces.[53] These are the Poisson equation, which relates the electric field flux to the charge density, and the Nernst–Planck equations, which relate the ion fluxes to the fluid velocity, concentration gradient, and electric field (see chapter 2.1). In addition to ignoring molecular effects these equations also assume an ideal (dilute) solution.

1.4 MOLECULAR EFFECTS ON SOLUTION TRANSPORT

In order to relax the assumptions of continuum hydrodynamics the fluid may be treated explicitly as a collection of molecules through molecular dynamics (MD) simulations. In simulating a molecular fluid in this way, the quantum effects on the dynamics are ignored and the molecules interact with each other as classical particles. Their interactions are defined by an intermolecular potential that generally includes van der Waals, electrostatic, bonded, angle, and dihedral contributions. Newton's equations of motion are then solved numerically using the negative gradient of the intermolecular potential as the force, and the system is evolved with time (see chapter 2.2).[54]

It is not a simple matter to simulate a concentration gradient in MD, especially when using periodic boundary conditions to simulate a bulk fluid. Figure 1.8 illustrates one of the problems for a naive application of periodic boundaries. The periodic boundaries connect the high and low concentration sides of the membrane, allowing them to mix. There are several methods one can use to simulate a concentration-gradient-driven flow in MD. These include transient-flux simulations, stochastic simulations with particle insertions and deletions, and deterministic simulations in which an external field is applied to the system.

The simplest method to simulate a concentration gradient in MD is to use two reservoirs with different solute concentrations on either side of a porous membrane and measure the transient flux through the membrane. Many studies have used this method.[55–57] For example, Kalra et al.[56] simulated the transient flux of water from a pure water reservoir sandwiched between two carbon nanotube membranes towards salt water reservoirs on either side (Figure 1.9). There is a major problem with using this method to simulate concentration-gradient-driven flows, which is that the concentration gradient changes throughout the simulation, so statistical averaging to measure flow properties is poor unless very large reservoirs are used, which is inefficient.

Various Monte Carlo algorithms have been devised to simulate a constant chemical potential gradient in MD.[58–61] For example, Heffelfinger and Swol[58] devised a method called dual control volume grand canonical molecular dynamics (DCV-GCMD). In this method
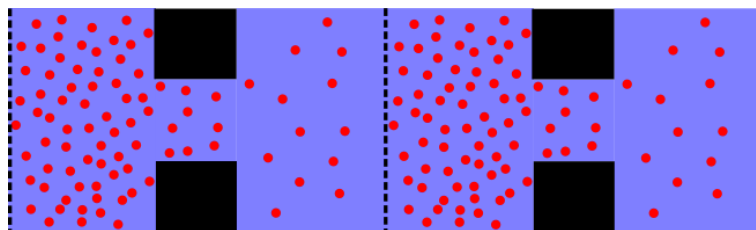
Figure 1.8: Problem with simulating concentration gradient in system with periodic boundaries (denoted by dashed vertical lines). The two bulk solution reservoirs are in direct contact through periodic boundary conditions and will readily mix.
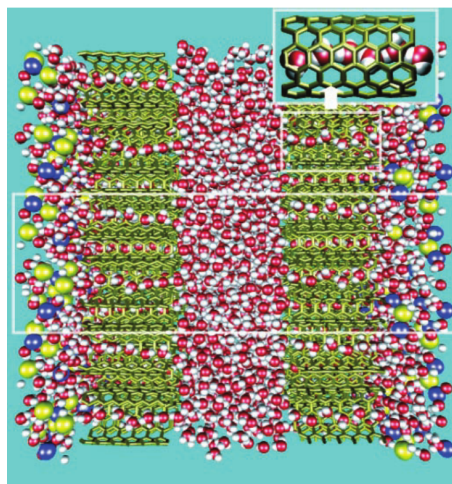
Figure 1.9: Transient flux simulations. Pure water is sandwiched between two carbon nanotube membranes with salt water on either side. The pure water flows through the membrane towards the high solute concentration sides until the water reservoir is depleted. (image source: Kalra, A.; Garde, S.; Hummer, G. *Proceedings of the National Academy of Sciences of the United States of America* **2003**, *100*, 10175–10180.[56])
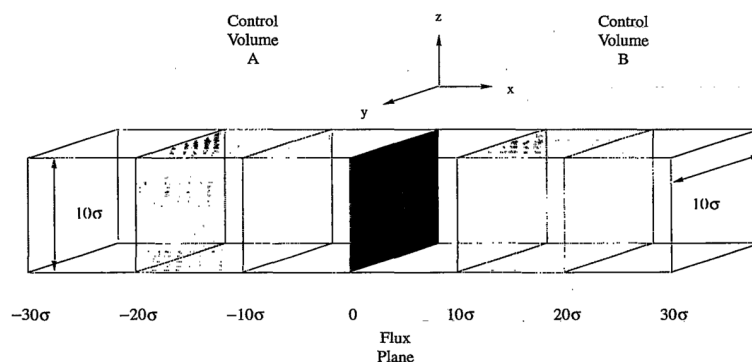
Figure 1.10: Dual control volume grand canonical molecular dynamics. Solute chemical potentials are maintained in the two control regions using a Monte Carlo algorithm. (Image source: Heffelfinger, G. S.; Swol, F. v. *The Journal of Chemical Physics* **1994**, *100*, 7548–7552.[58])

the two reservoirs are maintained at constant chemical potentials using a grand canonical Monte Carlo algorithm, which inserts, deletes, and moves solute particles in the two reservoirs randomly in order to maintain their chemical potentials (Figure 1.10). However, for simulations at liquid densities, these particle insertions are extremely inefficient. For example, in Zheng et al.[62] 100–150 stochastic steps were required for each MD time step. Another problem with DCV-GCMD is that the stochastic nature of these simulations interrupts the course of MD simulations, which are deterministic.

To address the problems with stochastic simulations of concentration gradients, one can use an algorithm that simulates a constant chemical potential gradient by applying an external field to the solute and solvent particles.[8,31,47,63] For example, Liu et al.[47] used forces to model a chemical potential gradient to calculate transport diffusion of methane, and Yoshida et al.[31] used a force on each solute particle, and a counter-force on each solvent particle to model a constant chemical potential gradient. These methods do not explicitly simulate concentration differences. On the other hand, the algorithm by Khalili-Araghi et al.[8] works by applying forces to the solute and solvent particles only within thin regions at the ends of the periodic simulation cell. This method establishes a concentration difference across a membrane, which drives flow of solute and solvent across it. Figure 1.11 illustrates this method. Using this method Khalili-Araghi et al. were able to accurately reproduce experimental results of ion selectivities and open-circuit voltages (applied electrical potential
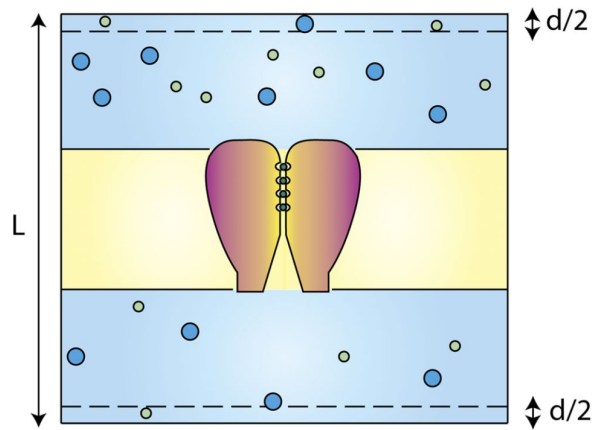
Figure 1.11: Diagram showing transition regions where forces are applied to solute particles for non-periodic energy step method. The force is applied to solute particles at the ends of the simulation cell within thin slabs of width $d/2$ each. The energy step fixes the chemical potential gradient across the membrane. (Image source: Khalili-Araghi, F.; Ziervogel, B.; Gumbart, J. C.; Roux, B. *Journal of General Physiology* **2013**, *142*, 465–475.[8])

differences at zero current) across a bacterial OmpF protein pore, which is a wide cation-selective pore present in the outer membrane of *Escherichia coli*.[53] The algorithm was shown to be able to accurately simulate ion fluxes at low salt concentrations. This algorithm will be explained in more detail in section 2.2.6.

1.5 PROJECT OUTLINE

A wide range of solution transport processes can be described by considering a combination of several general different transport phenomena. Understanding these phenomena using general models has implications for many different processes such as desalination, filtration, and energy harvesting.[12] It is the goal of this thesis to shed some light onto these transport phenomena with a particular focus on entrance effects.

For electrolyte transport, the access electrical resistance caused by the bending of electric field lines into the narrow pore from the bulk reservoirs can become the limiting factor for ion transport in short pores and pores with low friction. There are several theories for the access electrical resistance. The earliest theories assume that the pore is neutral,[2,3] which often does not hold. A more recent theory by Lee et al.[7] considers the pore to be charged but makes no assumptions about the surface charge on the outer-membrane surface. There is currently no general theory for the access electrical resistance of charged pores in charged membranes. Therefore, it is the aim of this thesis to clarify the scaling of the access electrical resistance with surface charge density, salt concentration, and pore radius for pores with charged versus uncharged outer-membrane surfaces. The scaling will then be compared with existing theories, and the deviations from the theories will be discussed. Furthermore, a new theory will be derived that accurately describes the access electrical resistance for charged pores in charged membranes.

The conventional continuum equations for solution transport assume an ideal (dilute) solution.[64] It is difficult to derive continuum equations for studying non-ideal solutions (such as mixtures of arbitrary mole fraction). In this case MD simulations are more amenable to studying solution transport. However, constraining the concentration difference across a membrane pore is difficult to do in MD due to the periodic boundary conditions that are used to simulate a bulk fluid. Due to periodic boundary conditions the two solution reservoirs are in direct contact and are able to mix in the absence of applied forces. Several different strategies have been used to overcome this problem, as outlined above.

In this thesis the algorithm by Khalili-Araghi et al.[8] will be used, but with a modification to allow it to function properly at high solute concentrations. The modified algorithm will be used to simulate diffusio-osmotic flows through pores of different lengths in order to investigate the entrance effects associated with diffusio-osmosis, which has not been previously studied systematically. In particular, the non-continuum and non-ideal effects on the access diffusio-osmotic resistance will be investigated by comparing it with continuum theory. A new continuum-based equation for the diffusio-osmotic flux and solute flux that takes into account the access resistance will also be derived.

COMPUTATIONAL METHODS

2.1 CONTINUUM MECHANICS

The continuum assumption is often used for describing electrolyte transport across nanoporous membranes. In this description, the fluid is considered as a continuous medium. This is a reasonable assumption at a low Knudsen number, which is the ratio of the molecular interaction length scale to the characteristic length of the system. By considering this length scale for liquid water, it was found that the continuum assumption is likely to break down when the smallest dimension of the nanofluidic system (eg. the pore radius) is smaller than ~ 3 nm.[52] To model fluid transport under the continuum assumption the Navier-Stokes equations are generally used. At the nano scale these equations can be simplified by ignoring the inertial terms of the equations. This is justifiable for flows with a low Reynolds number, being the ratio of inertial forces to viscous forces on the fluid. This assumption is justifiable in modelling flows through nanopores as these are generally dominated by viscous forces.[52]

The continuum equations for describing the transport of an electrolyte with equal anion and cation valences (Z:Z electrolyte) are the Poisson equation for the electrostatic potential ϕ, the Nernst–Planck equations for the solute flux j_i of species i, the Stokes equations for the fluid velocity u, and pressure p, along with the continuity equation for an incompressible flow:

$$-\epsilon\epsilon_0\nabla^2\phi = Ze(c_+ - c_-); \tag{2.1}$$

$$\nabla \cdot j_i = \nabla \cdot (c_i u - Z_i e\lambda_i c_i \nabla\phi - D_i\nabla c_i) = 0; \tag{2.2}$$

$$\mu\nabla^2 u = \nabla p + eZ(c_+ - c_-)\nabla\phi; \tag{2.3}$$

$$\nabla \cdot u = 0. \tag{2.4}$$

Here, ϵ is the dielectric constant, ϵ_0 is the permittivity of free space, e is the elementary charge, Z is the absolute valence for a Z:Z electrolyte, Z_i are the ion valences for a Z:Z electrolyte ($Z_+ = -Z_- = Z$), c_+ and c_- are the cation and anion concentrations, respectively, j_i are the ion fluxes ($i = +$ or $-$), c_i are the ion concentrations, λ_i are the ion mobilities, D_i are the ion diffusivities, and μ is the fluid viscosity. The diffusivities are assumed to be related to the mobilities through the Einstein relation ($\lambda_i = D_i/k_B T$, where k_B is Boltzmann's constant, and T is the temperature). These equations are known as the Poisson–Nernst–Planck–Stokes (PNPS) equations. In using these equations a dilute electrolyte is assumed.

2.1.1 *Finite element method*

In general the PNPS equations cannot be solved using analytical methods. Therefore, numerical methods must be used to solve them. In this thesis the finite element method (FEM) was used to solve the PNPS equations via COMSOL Multiphysics ® version 4.3a[65]. In FEM
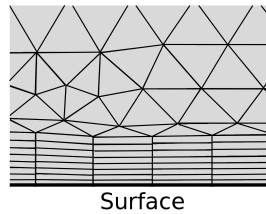
Figure 2.1: Finite element mesh. Thin boundary layers were used at the solid boundary, which is where quantities such as the electrical potential vary sharply.
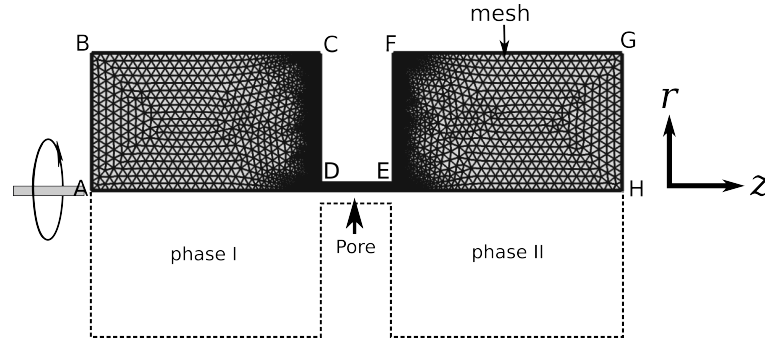
Figure 2.2: Pore geometry for solving PNPS equations via the finite element method. The boundaries CDEF represent the solid membrane and pore surfaces, while the other boundaries are liquid–liquid boundaries. The geometry has rotational symmetry about the boundary AH.

the partial differential equations (PDEs) are discretized into a set of numerical model equations, which are then solved on a compuational grid, called a mesh. A mesh consists of all the points at which the model equations are solved. The solutions to the model equations approximate the true solutions to the PDEs.

In FEM the distribution and density of mesh points is chosen such that, for a given geometry and system of equations, the solutions do not change when the density of the mesh points is increased. A finer mesh is used in regions where the solutions vary sharply. Figure 2.1 shows an example of a mesh composed of thin boundary layers. The mesh is finer in the direction perpendicular to the surface, which is where variables such as the electrical potential and ion concentrations vary sharply.

2.1.2   *Pore model*

To study electrolyte transport across a porous membrane only a single pore was considered. In this thesis it was assumed that the effects of neighbouring pores were negligible and that the pores in the membrane were monodisperse (meaning they were all the same size). Many synthetic pores, such as carbon nanotubes, can be manufactured with a narrow distribution of pore sizes.[66] Furthermore, for a large aspect ratio (length to diameter ratio) of the pores, the effect of neighbouring pores becomes small.[67] Therefore, these are reasonable assumptions to make. Figure 2.2 shows the model that was used in this thesis to study the continuum effects on electrolyte transport with the FEM mesh superimposed. It consisted of a single cylindrical pore between two cylindrical reservoirs. The geometry has rotational symmetry about the boundary AH. This greatly reduces the computational cost of the calculations. The size of the reservoirs was chosen to match those used in a previous study.[1]

In order to solve the PNPS equations a set of boundary conditions are required. The boundary conditions that were used for this study are listed in Table 2.1 with respect to the boundaries in Figure 2.2. Conventionally, the fluid velocity is assumed to be zero at the solid

Table 2.1: Boundary conditions for solving PNPS equations. The vector $\hat{n}$ is the surface normal, while superscripts I and II refer to phases I and II, respectively. In general, the surface charge density σ of the pore was different from the surface charge density σ_m of the membrane.

Boundary	Conditions
AH	$\hat{n} \cdot \nabla \phi = \hat{n} \cdot \nabla c = \hat{n} \cdot \boldsymbol{u} = \hat{n} \cdot \nabla \boldsymbol{u} = 0$
AB	$\phi = \phi^{\mathrm{I}}, c_+ = c_- = c^{\mathrm{I}}, p = 0$
GH	$\phi = \phi^{\mathrm{II}}, c_+ = c_- = c^{\mathrm{II}}, p = 0$
BC & FG	$\hat{n} \cdot \nabla \phi = \hat{n} \cdot \boldsymbol{j}_i = \hat{n} \cdot \boldsymbol{u} = \hat{n} \cdot \nabla \boldsymbol{u} = 0$
CD & EF	$\hat{n} \cdot \nabla \phi = -\sigma_m/(\epsilon\epsilon_0), \hat{n} \cdot \boldsymbol{j}_i = \hat{n} \cdot \boldsymbol{u} = 0$
DE	$\hat{n} \cdot \nabla \phi = -\sigma/(\epsilon\epsilon_0), \hat{n} \cdot \boldsymbol{j}_i = \hat{n} \cdot \boldsymbol{u} = 0, \hat{n} \cdot \nabla \boldsymbol{u} = \boldsymbol{u}/b$

surfaces. However, for low-friction surfaces the fluid velocity at the surface is non-zero due to fluid slip. This effect is particularly relevant to nanoscale flows due to the high surface area to volume ratios. The degree of fluid slip at the surface is quantified by the slip length, being the distance from the surface at which the linearly extrapolated velocity profile goes to zero (Figure 2.3). In this thesis the fluid velocity at the outer-membrane surfaces (CD and EF) was assumed to be zero ($\boldsymbol{u} = 0$), while at the pore surface (DE) the fluid velocity was given by the Navier partial slip condition ($\hat{n} \cdot \nabla \boldsymbol{u} = \boldsymbol{u}/b$ with b the slip length).

2.1.3 *Access electrical resistance*

The total electrical resistance R_T of a nanopore is a combination of the access electrical resistance R_a of each pore end and the pore electrical resistance R_p. It may not be possible to separate these in practice. However, in ref. 1 it was shown that in many cases the access electrical resistance does decouple from the pore electrical resistance. In this case the total electrical resistance is approximated by

$$R_T = 2R_a + R_p. \tag{2.5}$$

In the limit that the pore electrical resistance is negligible, the total electrical resistance is equal to twice the access electrical resistance of a single pore end.
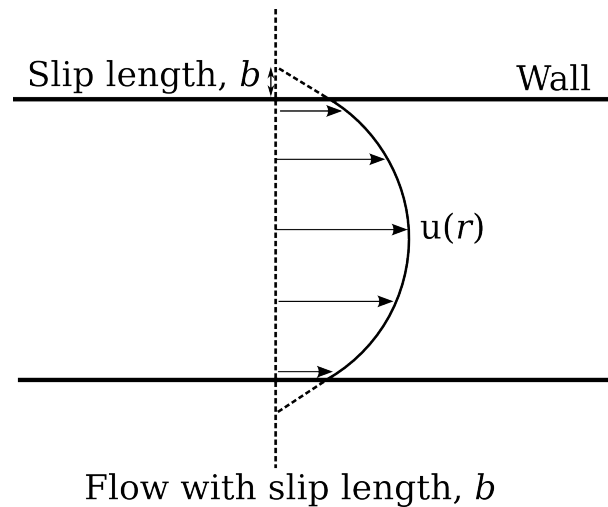
Figure 2.3: Definition of slip length, being the distance from the surface at which the linearly extrapolated velocity profile is equal to zero.
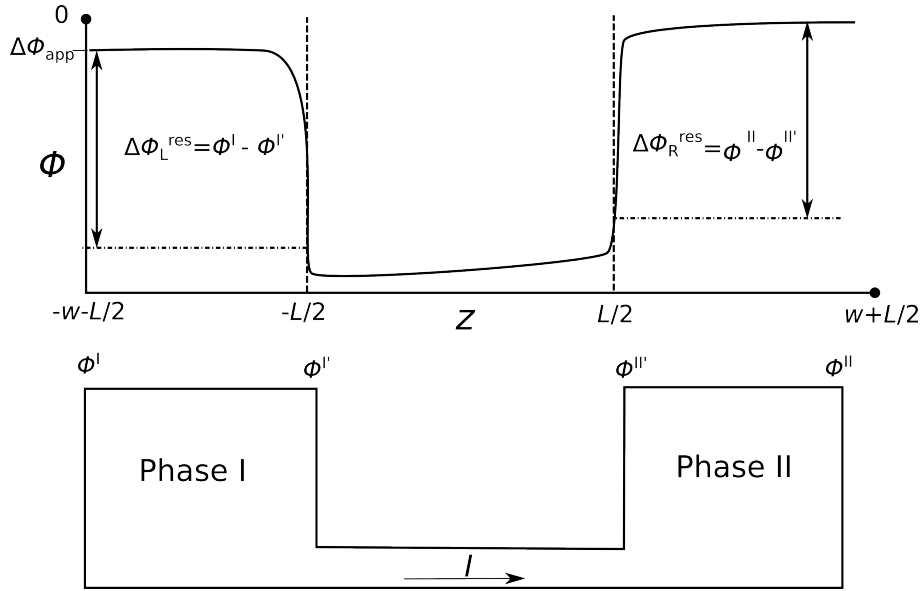
Figure 2.4: Diagram of potential drop over reservoirs.

In calculating the access electrical resistance no gradients of salt concentration or fluid pressure were applied across the pore, but different electrical potential differences were applied and the resulting currents I were calculated by

$$I = 2\pi Ze \int_0^a \mathrm{d}r\, r(\boldsymbol{j}_+ - \boldsymbol{j}_-) \cdot \hat{\boldsymbol{z}}, \tag{2.6}$$

where r was the radial coordinate, defined as the radial distance from the centre of the pore, a was the pore radius, and $\boldsymbol{j}_+$ and $\boldsymbol{j}_-$ were the fluxes of the cations and anions, respectively, and $\hat{\boldsymbol{z}}$ is the unit vector in the axial direction. In this way a current–voltage curve was obtained, which was used to calculate the resistance of the nanopore from the inverse of the slope.

There are several ways that the access electrical resistance can be calculated. The most straightforward way is to calculate the electrical potential drop over the reservoirs and divide it by the current through the pore (cf. Yan et al.[37]), which due to charge conservation is the same as the current through the reservoir. Figure 2.4 illustrates this method, which will be referred to as the "potential drop method". Here L is the pore length, w is the reservoir length, $\Delta\phi_{\mathrm{app}}$ is the applied electrical potential difference, I is the electrical current through the pore, ϕ^{I} and ϕ^{II} are the electrical potentials far from the pore entrances, $\phi^{\mathrm{I'}}$ and $\phi^{\mathrm{II'}}$ are the electrical potentials at the pore entrances, and $\Delta\phi_{\mathrm{L}}^{\mathrm{res}}$ and $\Delta\phi_{\mathrm{R}}^{\mathrm{res}}$ are the electrical potential drops across the left and right reservoirs, respectively. In this method the potential drops over the reservoirs are measured at different applied potentials (and hence different electrical currents), which results in a current–voltage curve for each reservoir. The access electrical resistance for each pore entrance is then calculated from the inverse slope of the current–voltage curves for each of the reservoirs (Figure 2.5). The access resistance for one pore entrance is then given by the average access resistance over the two pore entrances.

Another method for calculating the access electrical resistance is to measure the total resistance ($R_{\mathrm{T}} = \Delta\phi_{\mathrm{app}}/I$) for different pore lengths and extrapolate to zero pore length using a linear fit to the data. This will be referred to as the "length method" (Figure 2.6). In this method the access electrical resistance is approximated by half the total resistance in the limit of zero pore length. This assumes that the access electrical resistance is uncoupled from the pore electrical resistance (does not depend on pore length).

For pores with high slip lengths, the pore resistance becomes negligible.[1,37] Therefore, the access resistance may also be calculated from the total resistance in the limit of infinite slip length. This is accomplished by fitting the total resistance versus slip length data to
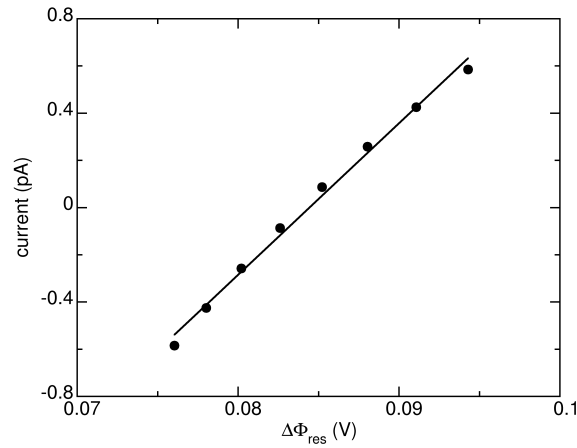
Figure 2.5: Example current–voltage curve for calculating the access resistance via the potential drop method. The points are from numerical calculations while the line is a linear fit.
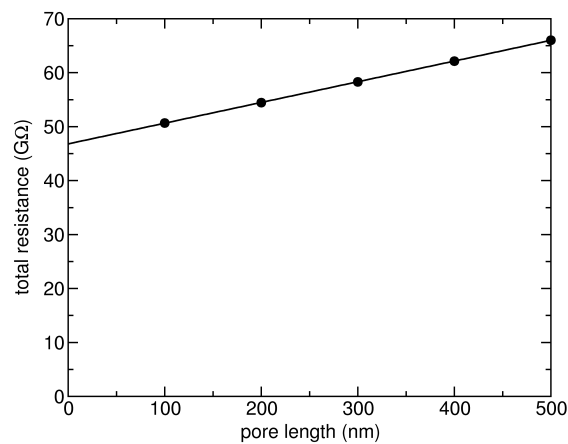
Figure 2.6: Example of total resistance versus pore length. The access resistance for two pore entrances is estimated from the limit of the total resistance as the pore length approaches zero. The points are from numerical calculations while the line is a linear fit.

$R_{\mathrm{T}} = A + (B + Cb)^{-1}$, where A, B, and C are fitting parameters. The access resistance is then given by half the total resistance at infinite slip length (i.e. $A/2$). This scaling of the total resistance with slip length is quite general and holds in many cases for which analytical expressions can be derived, including ion-selective pores, thin electric double layers, and small electrostatic surface potentials, as shown in ref. 1. Figure 2.7 shows an example of calculating the access resistance by this method, which will be referred to as the "slip method".

A comparison of the different methods for calculating the access electrical resistance is given in chapter 3.
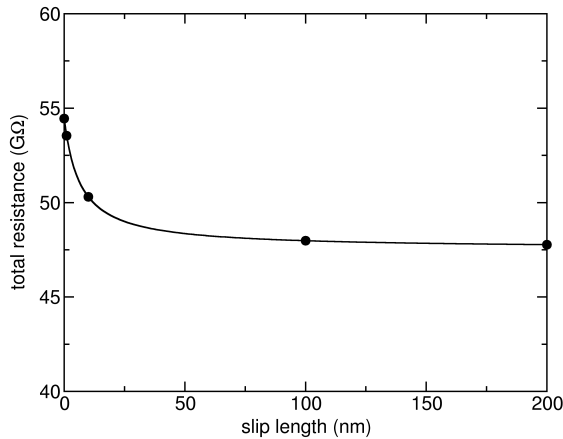
Figure 2.7: Example of total resistance versus slip length. The access resistance is approximated as half the total resistance at infinite slip length. The points are from the numerical calculations while the curve is a fit to $R_T = A + (B + Cb)^{-1}$, where A, B, and C are fitting parameters.

2.2   MOLECULAR DYNAMICS

When modelling flows through nanopores with extreme surface confinement, such as pores with diameters of several solvent molecular diameters, the fluid can no longer be considered as a continuous medium. In this case the molecular nature of the fluid must be taken into account. Furthermore, for non-ideal solutions there is no general analytical equation for the chemical potential of a mixture. In order to relax these assumptions the fluid can be modelled explicitly using molecular dynamics (MD).

In classical MD the solute, solvent, and solid are all treated as explicit classical particles that interact with each other via a realistic intermolecular potential (force field). The parameters used in the force field are often derived from experiments or quantum chemical calculations so as to model a real system. Once the force field has been specified there are four basic steps to an MD simulation:

1. Give the particles initial positions r_i and velocities v_i, which are sampled from a specified distribution (Gaussian distribution used in this thesis) to give the desired temperature T.

2. Calculate the forces on all particles from the negative gradient of the force field $F_i(r^N) = -\nabla_i U(r^N)$, which depends on the positions of all of the N particles, r^N.

3. Numerically integrate Newton's equations of motion

$$F_i(r^N) = m_i \frac{d^2 r_i}{dt^2} = -\nabla_i U(r^N), \tag{2.7}$$

where m_i is the mass of the ith particle with acceleration $\frac{d^2 r_i}{dt^2}$.

4. Increment simulation time by the time step Δt and update r_i and v_i.

The last three steps above are repeated until the properties of the system no longer change with time. This is when the simulation has reached a steady state (eg. equilibrium). After the system has reached a steady state the properties of interest are computed.

The above algorithm is for simulations of systems with a constant number of molecules, volume, and energy (NVE), known as the microcanonical ensemble. To simulate a system that also has a constant temperature, which is how the simulations in this thesis were carried out, a thermostat must be applied to the system. This will be discussed in section 2.2.4.

2.2.1 *Force field*

The force field gives the potential energy due to bonded and non-bonded interactions between atoms. The equation for the total potential is

$$U_{\text{total}} = U_{\text{bonded}} + U_{\text{non-bonded}}, \tag{2.8}$$

where U_{bonded} is the potential for the bonded interactions and $U_{\text{non-bonded}}$ is the potential for the nonbonded interactions. The equation for the bonded potential is

$$U_{\text{bonded}} = U_{\text{bond}} + U_{\text{angle}} + U_{\text{dihedral}}, \tag{2.9}$$

where U_{bond} is the potential due to bond vibration, U_{angle} is the potential due to angle bending, and U_{dihedral} is the potential due to dihedral twisting. The equation for the non-bonded potential is

$$U_{\text{non-bonded}} = U_{\text{vdw}} + U_{\text{electrostatic}}, \tag{2.10}$$

where U_{vdw} is the potential due to van der Waals forces, and $U_{\text{electrostatic}}$ is the potential due to electrostatic interactions. The different interactions contributing to the total potential are illustrated in Figure 2.8.

One of the simplest fluids to model in MD is the Lennard-Jones fluid. In this model only non-bonded (van der Waals) forces between particles are considered. The force field for the Lennard–Jones fluid is given by

$$U(\mathbf{r}^N) = \sum_{j=1}^{N-1} \sum_{i=j+1}^{N} 4\epsilon_{ij} \left[\left(\frac{\sigma_{ij}}{r_{ij}} \right)^{12} - \left(\frac{\sigma_{ij}}{r_{ij}} \right)^{6} \right], \tag{2.11}$$

where r_{ij} is the distance between the ith and j^{th} particle, ϵ_{ij} is the well depth of the potential energy between particles i and j, and σ_{ij} is the distance between them at which the potential is zero. By tuning the ϵ_{ij} and σ_{ij} values different fluids can be modelled.

The Lennard–Jones potential is a reasonably accurate model for the interactions in simple non-polar fluids, such as liquid argon and methane. The benefits of the Lennard–Jones fluid are that it is computationally cheap to run, while still allowing for a systematic study of transport phenomena without reference to any particular real system. Therefore, it is useful for giving qualitative scaling laws, which are applicable to any solute and solvent mixture.
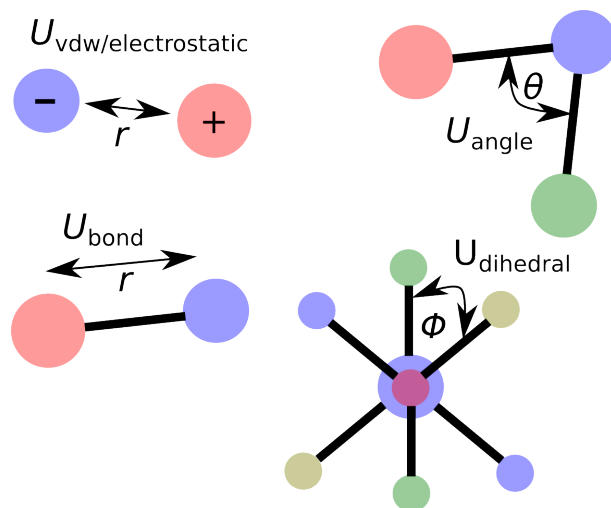
Figure 2.8: Contributions to intermolecular potential.

For the fluids studied in this thesis, a binary mixture of solute and solvent particles that interacted via van der Waals forces only was considered (no Coulombic forces). Therefore, the Lennard–Jones fluid model was employed. The solute and the solvent were identical but for their interaction with the solid surfaces.

2.2.2 *Periodic boundaries*

To simulate a bulk fluid periodic boundary conditions must be used. For simulation box lengths of $L_m(m = x, y,$ or $z)$ the following procedure is followed for the x coordinate of particle i, x_i, with analogous equations applying for the y and z coordinates:

$$if \ x_i > L_x, x_i \rightarrow (x_i - L_x), \tag{2.12}$$

$$if \ x_i < 0, x_i \rightarrow (x_i + L_x). \tag{2.13}$$

Therefore, when a particle travels farther than the box length in any direction, it appears back on the other side of the simulation cell (Figure 2.9). This essentially simulates an infinite number of simulation cells in each direction.

Calculating the non-bonded forces between all particles explicitly in an infinite array of simulation cells would be impossible. Therefore, the minimum-image convention is used to calculate the forces between particles and their periodic images. In this convention only the closest periodic image of the particles contribute to the force. For two particles i and j, and the periodic image of j (j') the minimum image convention is

$$if \ x_{ij} > L_x/2, x_{ij} \rightarrow (x_{ij} - L_x), \tag{2.14}$$

$$if \ x_{ij} < -L_x/2, x_{ij} \rightarrow (x_{ij} + L_x), \tag{2.15}$$

where x_{ij} is the distance between particles i and j in the x direction (similar conditions are used for y_{ij} and z_{ij}). If the distance between particles i and j is larger than half the simulation box length, then the force between particles i and the j' is calculated instead (Figure 2.10).
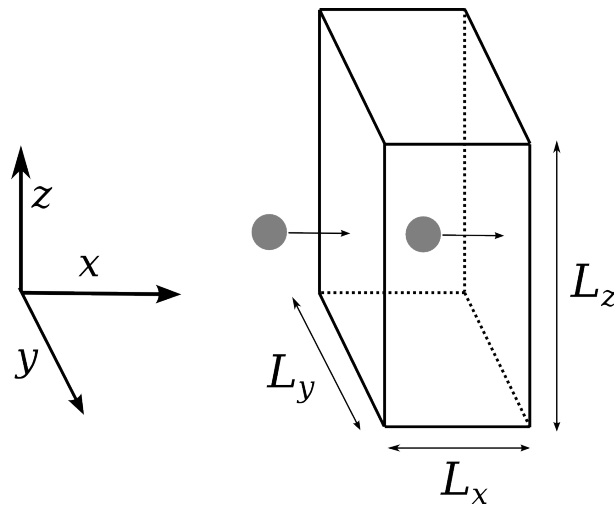
Figure 2.9: Periodic boundary conditions. When a particle travels father than the box length in any direction it appears back on the other side of the simulation cell. This essentially simulates an infinite array of simulation cells in each direction.
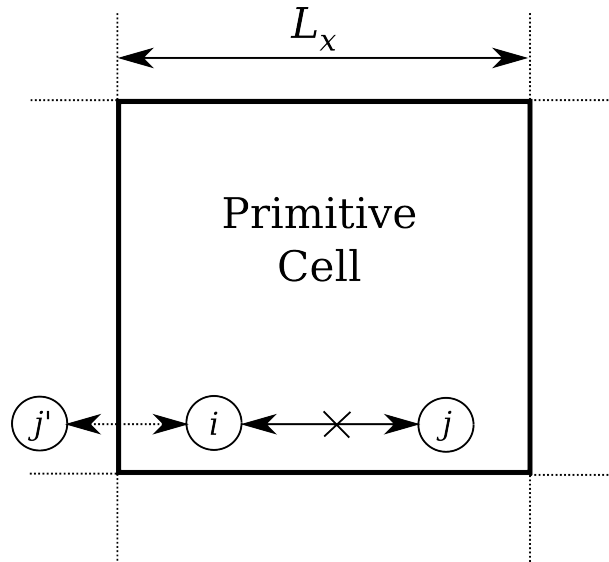
Figure 2.10: Minimum image convention. The force between i and j' is computed instead of the force between i and j, according to the minimum image convention.

2.2.3   Cut-offs

In order to avoid explicitly calculating the non-bonded forces between each particle and all other particles in the system, which would preclude molecular simulations on the scales of interest, forces are only calculated between particles within a cut-off radius r_c. The simplest method of achieving this, which is used in this thesis, is the simple cut-off potential,

$$U_c(r) = \begin{cases} U_{\text{vdw}}(r), & r \leq r_c \\ 0, & r > r_c \end{cases}.$$
(2.16)

2.2.4   Thermostat

The methods described above make it possible to simulate a system with a constant number of particles, volume, and energy (NVE), which is known as the microcanonical ensemble. However, to simulate a realistic experimental system, the number of molecules, volume, and temperature (NVT) should be held constant, which is known as the canonical ensemble. In order to keep the temperature constant a thermostat needs to be applied to the system. The thermostat used in this study is the Nosé–Hoover thermostat.[68] This thermostat works by modifying the equations of motion according to

$$\dot{r}_i = p_i/m_i,$$
(2.17)

$$\dot{p}_i = F(r_i) - \zeta p_i,$$
(2.18)

and

$$\dot{\zeta} = \left[\sum_{i=1}^{N} p_i^2/m_i - Xk_{\text{B}}T\right]/Q.$$
(2.19)

Here, p_i are the particle momenta, X is the number of degrees-of-freedom, $\zeta = \frac{ds}{dt}$ ($s = \frac{d\tau}{dt}$ is a scaling factor for the virtual time τ), and Q is the coupling constant for the heat bath that is in direct contact with the system.[54]

When there is a net flow of fluid ocurring in the system the fluid velocity field should be separated from the particle velocities before computing the temperature to prevent the thermostat from perturbing the fluid flow. To subtract the fluid velocity field it is assumed that the velocity of each particle $\dot{r}_i$ can be broken down into a random thermal velocity v_i, and a streaming velocity $u(r_i)$,

$$\dot{r}_i = v_i + u(r_i). \tag{2.20}$$

The streaming velocity depends on the coordinate r according to

$$u(r) = \frac{\sum_{i=1}^{N} m_i \dot{r}_i \delta(r_i - r)}{\sum_{i=1}^{N} m_i \delta(r_i - r)}, \tag{2.21}$$

where δ is the Dirac delta function. The notation for the density in equation 2.21 is commonly used in statistical physics and implicitly assumes a spatial integral, which is achieved in MD simulations by a spatial average over bins.[19,69] The spatial integral is defined, even though δ may not be defined at a particular point in space. Equation 2.2 is evaluated by splitting the simulation box into finite-sized bins and summing over the bins after each time step. This is only reasonable when there are a large number of particles in each bin. The streaming velocity is then subtracted from the particle velocities at each time step before the temperature is computed. The equation for the temperature is given by

$$\frac{d(N - N_x N_y N_z)}{2} k_B T(r) = \sum_{i=1}^{N} \frac{1}{2} m_i (v_i - u(r))^2, \tag{2.22}$$

where d is the dimensionality of the system, and N_x, N_y, and N_z are the numbers of bins in the x, y, and z directions, respectively.[70] Equation 2.22 suggests that there are three constraints for every bin. The summation in equation 2.21 is an instantaneous sum over the bins. Therefore, using three constraints for each bin in equation 2.22 is only reasonable when there are a large number of particles per bin. When applying a thermostat to a fluid undergoing flow the average fluid velocity field is subtracted from the total particle velocities before the thermostat is applied. After the thermostat is applied the average fluid velocity field is then added back to the particles. In this way the thermostat is applied only to the thermal velocities of the particles, while the streaming velocities remain unchanged. This method is called the profile-unbiased thermostat (PUT).[69] In this thesis the normal Nosé–Hoover thermostat was used for equilibration simulations, while the Nosé–Hoover PUT was used for the concentration-gradient-driven flow simulations.

2.2.5 *Pore model*

The systems considered in this thesis comprised a single nanopore in between two walls, both made of the same solid particles as the pore, with solute and solvent particles on either side. During the simulations a thermostat was applied to the fluid particles but not to the solid particles. Instead, they were frozen in place during the course of the simulation. There are some possible limitations to applying a thermostat directly to the fluid as opposed to applying a thermostat to the wall particles and allowing them to naturally heat the fluid. For example, in ref. 71 different density and velocity profiles were observed for highly confined fluids undergoing Couette flow when a thermostat was applied to the fluid directly, compared with when it was heated naturally by applying a thermostat to the wall. For the systems in this thesis, applying a thermostat to just the wall particles and allowing the fluid to be naturally heated would be very inefficient due to the large number of fluid particles compared with wall particles. However, the effect of applying a thermostat directly to the fluid compared with applying a thermostat to the wall and allowing the wall to heat the
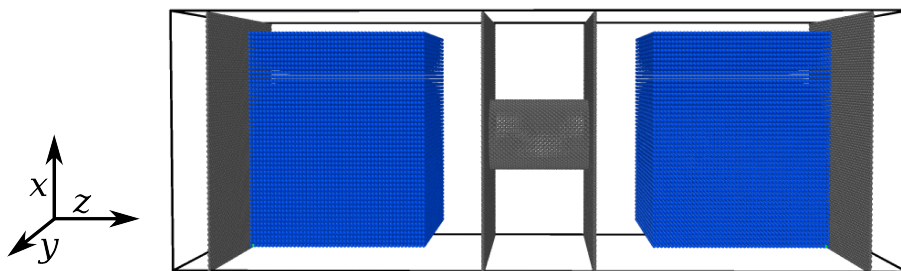
Figure 2.11: Initial particle positions for MD simulation. The blue particles represent the solvent, while the black particles represent the solid.

fluid is unlikely to affect the results presented in this thesis. This is because the smallest pore diameter considered here is larger than the systems in ref. 71, and the fluid velocities are orders of magnitude smaller.

In order to equilibrate the system at the desired pressure, pistons made of solid particles were used on either side of the simulation cell to compress the fluid into the pore such that it was at the desired pressure. The initial positions of the particles were generated using the Moltemplate software package,[72] while the Ovito software package[73] was used to remove wall atoms at the pore ends to open the pore. Figure 2.11 shows an example of one of the simulations before equilibration. Image snapshots were taken using the Ovito software package.

The forces applied to the piston particles were initially set such that the total pressure experienced by the pistons was $\pm p$ for the left and right pistons, respectively, where p was the target pressure of the fluid. As the pistons compress the fluid, the fluid exerts a force back onto them, corresponding to a pressure $\mp p'$. Each time step the force on the piston particles was set such that $p - p' = 0$. After the pistons had reached their equilibrium positions they were then frozen in place and the fluid was allowed to equilibrate (Figure 2.12).

For the equilibration the system was periodic in the lateral (x and y) directions and finite in the axial (z) direction. Once the system had been equilibrated the pistons were removed and the simulation cell was shortened in the z direction such that the system matched up with its periodic image in that direction (Figure 2.13). Particle overlap at the periodic boundary was avoided by making the new simulation cell length in the z direction equal to the distance between the pistons at the end of the equilibration minus σ. The value of σ was chosen as the Lennard–Jones diameter of the solid and the solvent used were both σ. Therefore, when σ was subtracted there were no gaps and also no particle overlap between the periodic images.

The equilibration was initially carried out with only solvent particles in the fluid. Following the equilibration a fraction of the solvent particles were set to be solute particles in each reservoir such that the desired concentration ratio was achieved. To avoid problems associated with shortening the z direction abruptly, the new system that was periodic in
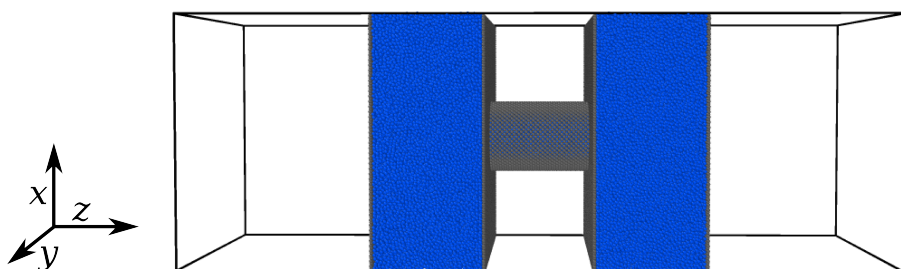
Figure 2.12: Final particle positions after pistons had compressed fluid into nanopore. The blue particles represent the solvent, while the black particles represent the solid.
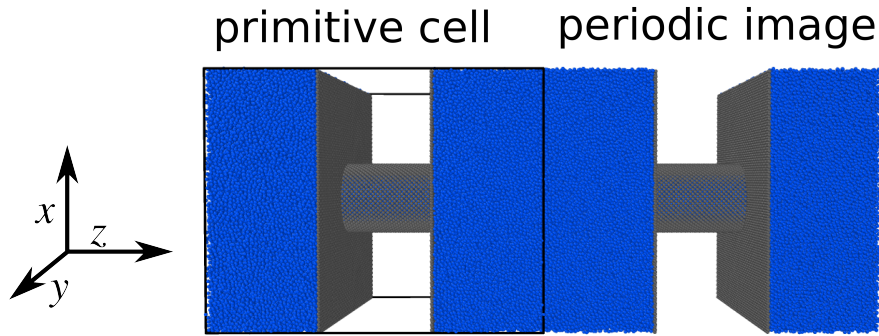
Figure 2.13: Matching simulation cell with periodic images after equilibration in MD. The blue particles represent the solvent, while the black particles represent the solid.

the z direction was allowed to equilibrate further before applying forces to the solute and solvent particles.

2.2.6 *Constrained concentration-difference algorithm*

The method used to constrain the concentration difference in this thesis was that used by Khalili-Araghi et al.[8]. In this method a force is applied to the solute particles at the ends of the simulation box, far from the membrane wall (Figure 2.14). This results in a non-periodic energy step that acts only on the solute particles within this region (called the transition region). The non-periodic energy step modifies the statistical distribution of the particles such that one reservoir has a higher average number of solute particles than the other.[8]

The force to apply to the solute particles within the transition regions in order to maintain a concentration ratio c_H/c_L for an ideal solution of non-interacting particles can be derived from the Boltzmann equation,

$$\frac{N_i}{N} = \frac{1}{e^{(\epsilon_i - \mu_c)/k_B T}}, \tag{2.23}$$
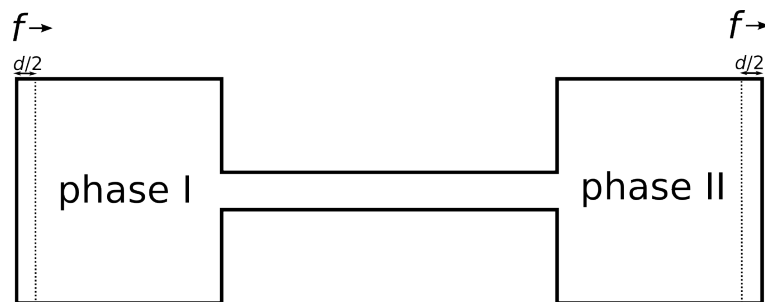
Figure 2.14: Diagram showing region where forces are applied in constrained concentration-difference algorithm. Forces are applied to the solute particles within a thin slab of width $d/2$ at each end of the simulation cell.

where N_i is the number of particles with energy ϵ_i, and μ_c is the chemical potential. Therefore, assuming that the reservoirs have equal volumes the ratio of particles with energy ϵ_i to particles with energy ϵ_j is

$$\frac{c_H}{c_L} = \frac{N_i}{N_j} = e^{(\Delta\epsilon/k_B T)}, \tag{2.24}$$

where c_H and c_L are the target solute concentrations in the high and low concentration reservoirs, respectively, and $\Delta\epsilon = \epsilon_j - \epsilon_i$ is the energy difference between states i and j. Rearranging this equation gives the energy step to apply in order to enforce a concentration ratio of c_H/c_L for a system of non-interacting particles,

$$\Delta\epsilon = k_B T \ln\left(\frac{c_H}{c_L}\right). \tag{2.25}$$

The force to apply within the thin transition regions of width $d/2$ at the ends of the simulation cell can then be given by

$$f = k_B T \ln\left(\frac{c_H}{c_L}\right)/d. \tag{2.26}$$

Khalili-Araghi et al. initially applied this force to the solute particles, but then updated the force every time step to correct for non-ideality of the MD system using the algorithm given by

$$f(t + \Delta t) = f(t) + \Delta f(t)\Delta t/(\alpha\tau), \tag{2.27}$$

where

$$\Delta f(t) = -\frac{k_B T}{d}\left[\left\langle\ln\left(\frac{c_1}{c_2}\right)\right\rangle - \ln\left(\frac{c_H}{c_L}\right)\right]. \tag{2.28}$$

In equation 2.28 c_1 and c_2 are the instantaneous concentrations of the high and low concentration reservoirs, respectively, α and τ are tunable parameters, Δt is the time step, and angle brackets indicate a time average over a period of time τ immediately preceding the current time step. The applied force is gradually adjusted such that the target concentration gradient is reached over a period of $\alpha\tau$. In this thesis, instead of updating the applied force every time step, they were updated every 10 000 time steps. This was determined to be adequate for convergence of the simulations (see chapter 4).

Constraining the solute concentration gradient using this algorithm results in a pressure difference at high solute concentrations (see chapter 4). This can be fixed by constraining the total pressure difference across the pore with the application of a counter-force to the solvent particles within the transition region. A similar algorithm for applying the forces can be used as for the solute, except that the applied force on the solvent is initially set to zero and updated according to equation 2.27 with

$$\Delta f(t) = \frac{\Delta p A}{N_v^T}, \tag{2.29}$$

where Δp is the difference in pressure between the two reservoirs, far from the membrane wall and the region where the forces are applied, A is the cross-sectional area of the simulation cell, and N_v^T is the number of solvent particles within the transition region. The applied force on the solvent particles was updated every 10 000 time steps, as for the solute. Without this correction to the algorithm by Khalili-Araghi et al. at high solute molar fractions the concentration ratio does not converge to the target ratio (see chapter 4). This modification was not discussed by Khalili-Araghi et al. but their algorithm does not restrict the species in the solution to which the energy step can be applied.
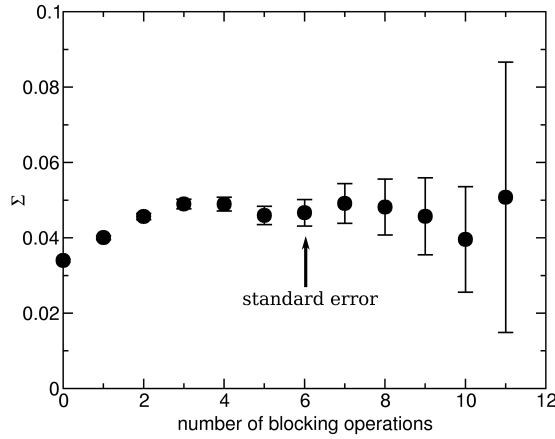
Figure 2.15: Calculation of standard error using the block averaging method. The standard error Σ reaches a plateau with respect to the number of blocking operations when the blocks become uncorrelated from each other. The standard error at the start of the plateau is used as the estimate of the standard error of the mean.

2.2.7   *Error estimates*

In order to calculate the error bars for the MD data the block averaging method from Flyvbjerg and Petersen[74] was used. In this method the data $x_1, \cdots x_n$ is transformed into a new data set that is half as large as the original one, $x'_1, \cdots x'_{n'}$, where $n' = n/2$. This is carried out by averaging adjacent data points using the equation:

$$x'_i = \frac{1}{2}(x_{2i-1} + x_{2i}),\tag{2.30}$$

which is known as a block average. After the block averaging is completed, the average of the new data set remains the same as the average of the original data set. This transformation (blocking operation) is repeated until the data points become uncorrelated from each other. This is determined by estimating the standard error in the mean after each blocking operation using the equation

$$\Sigma = \sqrt{\frac{1}{n'(n'-1)}\sum_{k=1}^{n'}(x_k - \bar{x})^2}\left(1 \pm \frac{1}{\sqrt{2(n'-1)}}\right),\tag{2.31}$$

where

$$\bar{x} = \frac{1}{n}\sum_{i=1}^{n}x_i.\tag{2.32}$$

When the standard error reaches a plateau with respect to the number of blocking operations the block averages become uncorrelated from each other. The true standard error is estimated from the first point at which the blocks become uncorrelated (see Figure 2.15). The error bars used in this thesis are calculated from twice the standard error.

ACCESS ELECTRICAL RESISTANCE

3.1 ABSTRACT

When electrolytes are transported across nanoporous membranes there can be significant electrical resistance at the entrance and exit of the pores called the access electrical resistance. In particular, the access electrical resistance becomes the limiting factor for ion/charge transport for low-aspect-ratio (length-to-diameter ratio) pores or low-friction pores.[1,7,15] The equation that is widely used to describe the access electrical resistance, due to Hall,[3] assumes that the pore is neutral. However, this is often not an adequate assumption. Lee et al.[7] have derived an equation for the access electrical resistance of charged pores but did not consider the effect of the surface charge on the outer surface of the membrane, which is known to reduce the access electrical resistance.[6] Up until now there has been no systematic study of the effect of the pore and membrane surface charge on the access electrical resistance. Here, the access electrical resistance is computed numerically using a continuum theory-based model. The scaling of the access electrical resistance with salt concentration, pore radius, and surface charge density is clarified. Different scaling is observed depending on whether the outer membrane surface is charged, which is not well described by any previously existing theory. In this study an analytical expression is derived for the access electrical resistance of a charged membrane in the regime of low surface potentials. A closed-form equation was then derived assuming both low surface potentials and highly overlapped electric double layers. The expression accounts for the outer-membrane surface charge and gives quantitative agreement with the numerical results.

3.2 INTRODUCTION

In experiments the total electrical conductance (inverse of total electrical resistance) of a porous membrane is often measured to characterise its ability and efficiency to transport ions/charge. For short pores and pores with low friction the total electrical resistance can be limited by the resistance at the pore entrances. This resistance occurs due to the bending of electric field lines from the bulk reservoirs into the narrow pores of the membrane (Figure 3.1). This quantity, called the access electrical resistance, may be separated from the total electrical resistance. The premise of calculating the access electrical resistance of a nanopore is that it is separable from the electrical resistance of the pore. This has commonly been assumed throughout the literature, from the earliest established theories,[2,3] to recent experimental studies carried out on biological pores.[16] It is important to note that the separation of the access and pore contributions to the total electrical resistance is an approximation. This has been shown to previously be a reasonable approximation under many conditions.[1,16,37]

It is often assumed that the total electrical resistance R_T is composed of the pore electrical resistance and access electrical resistance added up in series, i.e.

$$R_T = R_p + 2R_a, \tag{3.1}$$

where R_p is the contribution of the pore to the total electrical resistance and $2R_a$ is the contribution of the two pore entrances, R_a being the electrical resistance of a single pore entrance.

An analytical expression for the access electrical resistance was derived by Hall,[3] considering it to be the convergence resistance from a hemispherical electrode placed in the bulk
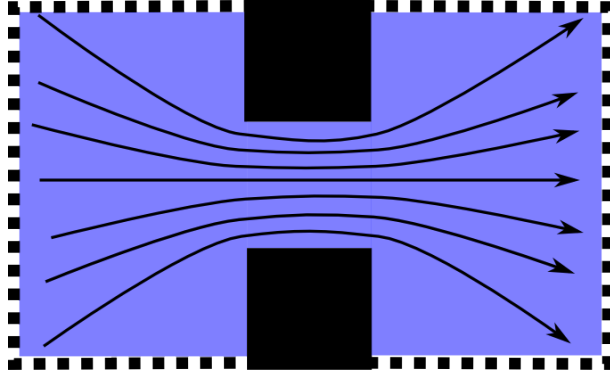
Figure 3.1: The access electrical resistance occurs mainly due to the bending of the field lines from the bulk reservoirs into the pore. The dotted lines show the liquid–liquid boundaries of the system.

electrolyte, far from the pore entrance, to an equipotential disk covering the end of the pore. The equation is

$$R_a = \frac{1}{4\kappa_b a},$$

(3.2)

where κ_b is the bulk electrolyte conductivity and a is the pore radius. The bulk conductivity of a binary Z:Z electrolyte ($Z_+ = -Z_- = Z$) may be written as

$$\kappa_b = e^2 \frac{|Z_+| c_{+\infty} D_+ + |Z_-| c_{-\infty} D_-}{k_B T},$$

(3.3)

where e is the elementary charge, Z_+ is the cation valence, $c_{+\infty}$ is the cation concentration far from any solid surface, D_+ is the cation diffusivity, Z_- is the anion valence, $c_{-\infty}$ is the anion concentration far from any solid surface, D_- is the anion diffusivity, k_B is Boltzmann's constant, and T is the temperature of the solution.

From the Hall equation (equation 3.2) the scaling of the access electrical resistance with pore radius is $R_a \sim 1/a$. The access resistance can become the limiting factor for ion/charge transport through nanoscopic pores, depending on the properties of the system being studied. One such property is the slip length b, which is related to the fluid–surface friction near the pore surface. The slip length is defined as the distance from the pore surface at which the fluid velocity profile within the pore linearly extrapolates to zero. The pore electrical resistance for a pore with a thin electric double layer (EDL) and $b = 0$ scales as $R_p \sim L/a^2$.[7] Therefore, when $L \sim a$ the access electrical resistance becomes of similar order to the pore electrical resistance. Furthermore, for an ion-selective pore with a large slip length the pore electrical resistance scales as $R_p \sim L/(ab\sigma^2)$,[1] where σ is the surface charge density of the pore. Therefore, for large slip lengths the pore electrical resistance can become negligible, and thus the access electrical resistance can dominate.

The Hall equation assumes that the pore entrances are equipotential, perfectly conducting disks, which is only approximate for pores with low aspect ratios, as well as for charged pores where there is no overlap of the EDLs. Nevertheless, Luan[40] found that the assumption of an equipotential disk at the pore ends is sufficient but not necessary for the equation by Hall to be accurate. Luan considered moderately charged pores (surface charge density $\sigma \approx 50 \text{ mC m}^{-2}$) in a neutral membrane (Figure 3.2), and found good agreement between numerical calculations of the electrical current and the theoretical electrical current, which used the access electrical resistance equation by Hall. These calculations were carried out for pores with radii comparable to their lengths, for which the access electrical resistance is expected to be a significant fraction of the total electrical resistance. Furthermore, the salt concentrations ranged from 50 to 1000 mM, which correspond to Debye lengths (characterising the width of the EDL) of 1.3–0.3 nm. The pore radii that were used ranged from
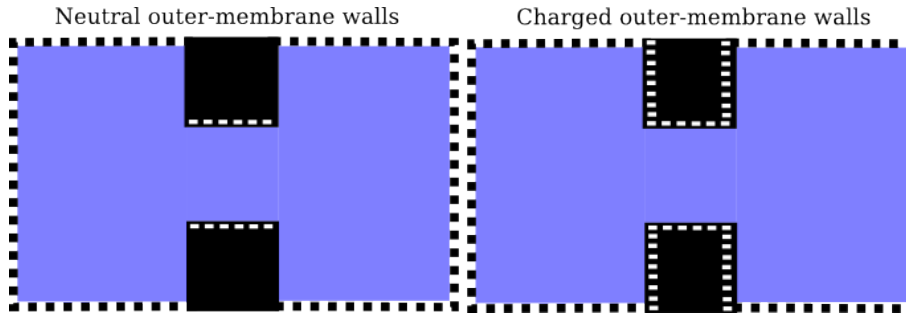
Figure 3.2: Charged pore in neutral (left) and charged (right) membranes. The dotted lines show the liquid–liquid boundaries of the system.

$\approx$1–50 nm, which means that under most conditions there was no EDL overlap. Therefore, the calculations by Luan were carried out under conditions for which the Hall equation is not expected to hold (charged pores with no EDL overlap). Despite this, good agreement with the theory was found, although the access electrical resistance was not calculated separately from the total electrical resistance.

The access electrical resistance is important in determining limiting effects of electrolyte transport. In a recent paper, it was found to severely limit the maximum power output obtainable from mixing salt water with fresh water, in a process known as reverse electrodialysis.[1] It was also found to depend significantly on both the surface charge density of the pore and that of the outer surface of the membrane.

Lee et al.[7] derived an equation heuristically in order to account for the effect of the pore surface charge on the access electrical resistance,

$$R_a = \frac{1}{2\alpha\kappa_b a + \beta\kappa_s},\tag{3.4}$$

where κ_s is the surface conductance, and α and β are numerical constants ($\alpha \sim \beta \sim 1$). This equation can also be written in terms of the Dukhin length, being the ratio of the surface conductance to the bulk conductivity ($l_{DU} = \kappa_s/\kappa_b$), as

$$R_a = \frac{1}{\kappa_b(2\alpha a + \beta l_{DU})}.\tag{3.5}$$

Assuming that the EDL width is small compared with the pore radius the Dukhin length is given by[7]

$$l_{DU} = \frac{|\sigma|}{2c_\infty e}\left[-\frac{l_{GC}}{\lambda_D} + \sqrt{\frac{l_{GC}^2}{\lambda_D^2} + 1}\right],\tag{3.6}$$

where σ is the surface charge density, c_∞ is the average salt concentration far from any solid walls (for a Z:Z binary electrolyte, with ion valences $Z_+ = Z$ and $Z_- = -Z$), λ_{GC} is the Gouy–Chapman length, and λ_D is the Debye length. The Gouy–Chapman length, which is the distance at which the thermal energy balances the ion–surface interaction energy, is given by

$$l_{GC} = \frac{2\epsilon\epsilon_0 k_B T}{Ze|\sigma|},\tag{3.7}$$

while the Debye length, which is the characteristic width of the EDL, is given by

$$\lambda_D = \kappa^{-1} = \sqrt{\frac{\epsilon\epsilon_0 k_B T}{2Z^2 e^2 c_\infty}},\tag{3.8}$$

where κ is the inverse Debye length (not to be confused with the bulk conductivity κ_b or surface conductance κ_s), ϵ is the dielectric constant, and ϵ_0 is the permittivity of free space. Discrepancies between the equations by Lee et al. and Hall are only expected when the Dukhin length is on the order of or larger than the pore radius. The basis for the derivation of these equations was that a discontinuity in surface conductance at a charged surface immersed in an electrolyte solution significantly alters the electric field in the bulk reservoirs.[75] Inside the pore there is a non-zero surface conductance due to the surface charges on the pore walls. However, directly outside the pore there is no surface conductance. Therefore, in order to ensure the continuity of the ion fluxes, extra ions must be supplied from the bulk reservoirs into the EDL of the pore, over a length scale given by the Dukhin length. As ions are supplied to the EDL of the pore, their concentration at the pore ends is increased, thereby reducing the access electrical resistance compared with the equation by Hall. This derivation made no assumptions about the charge on the outer membrane surface. Therefore, it could be expected that the same result would be achieved for a neutral outer membrane surface versus a charged one. In this chapter it is clearly shown that this is not the case.

A few papers have used the equation by Lee et al. to account for the effect of surface conductance on the access electrical resistance of charged pores.[15–17] However, none has systematically studied the effect of the charge on the outer membrane surface on the access electrical resistance, which is known to be significant.[6,16] In this study the access electrical resistance is calculated from numerical solutions to the PNPS equations for a charged pore with neutral or charged outer-membrane surfaces. Firstly, different methods for extracting the access electrical resistance from the total electrical resistance are discussed. Secondly, the predictions of the equations by Hall and Lee et al. are compared with the numerical calculations under a wide range of conditions, and the deviations from the theories are discussed. Lastly, a new theory is derived that specifically accounts for the charge on the outer membrane surface, which is then compared with FEM calculations and the equation by Lee et al.. Good agreement is found between the new theory and the FEM simulations under the conditions for which the theory was derived, whereas there were significant deviations from the equation by Lee et al. under the same conditions.

3.3 COMPUTATIONAL METHODS

In determining the access electrical resistance from the numerical calculations a few simplifying assumptions were made:

1. The electrolyte is a continuous medium and ions are uncorrelated point particles.

2. The Reynolds number (ratio of inertial to viscous forces) is small.

3. The pores are cylindrical and monodisperse (same length and radius).

4. The pore and outer membrane surfaces are perfectly flat and have a uniform surface charge density.

5. Neighbouring pores have no interaction with each other so only a single pore may be considered.

The assumption of continuum hydrodynamics (1) has been previously shown to be accurate by comparison with molecular dynamics simulations.[48,76] In terms of assumption (2) the typical Reynolds number ($Re = \rho u a / \mu$, where ρ is the fluid density, u is the characteristic fluid velocity within the pore, and μ is the viscosity of the fluid) for the systems considered in this study is on the order of 10^{-8}. Assumptions (3) and (4) may be satisfied using modern manufacturing techniques, such as the electrochemical anodisation of

Table 3.1: Parameters used in calculations. Where a range has been specified the values in parentheses were the default values used.

Quantity	Symbol	Value
dielectric constant	ϵ	78.46[79]
temperature	T	298 K
fluid viscosity	μ	0.894 mPa s[80]
cation valence	z_+	1
anion valence	z_-	−1
cation diffusivity	D_+	1.96×10^{-9} m^2 s^{-1}[81]
anion diffusivity	D_-	2.03×10^{-9} m^2 s^{-1}[81]
pore radius	a	2–70 nm (5 nm)
pore length	L	5–500 nm (200 nm)
reservoir radius\width	w	4 μm
surface charge density (pore wall)	σ	-(0–30) mC m^{-2}
surface charge density (membrane walls)	σ_m	0 or σ
slip length (pore wall)	b	0–200 nm (0)
slip length (membrane wall)	b_m	0
salt concentration in both reservoirs	c_s	0.1–30 mM
applied potential difference	$\Delta\phi$	−35–35 mV
pressure difference	Δp	0

aluminium.[77] It is noted that assumption (5) may not always hold, particularly when the inter-pore distance is on the same order as the pore diameter. This has been shown to lead to a non-extensive scaling of the conductance with the number of pores.[67] For simplicity of the theory only a single pore is considered in this study.

To model the electrolyte in this way the coupled PNPS equations, along with the continuity equation for an incompressible flow were solved for a single cylindrical pore between two cylindrical reservoirs using the finite element method (FEM) with COMSOL Multiphysics® version 4.3a[65]. The equations were solved using a fully coupled solver, which is a damped version of Newton's method. The damping option used to achieve convergence was "Automatic highly nonlinear (Newton)". The direct solver that was used is the PARDISO direct solver.[78] In order to vary the parameters in this study a parametric sweep was used to vary parameters that affect geometry and mesh generation, along with the parametric continuation solver for all other parameters.

The partial differential equations and boundary conditions used have already been given in chapter 2.1, so they will not be repeated here. The physical parameters that were used in this study are listed in Table 3.1. The reservoir sizes were chosen to be the same as in ref. 1, in which similar phenomena were studied. In most cases the no-slip condition (zero fluid velocity at solid surfaces) was assumed at the walls of the pore. However, in calculating the access electrical resistance via the "slip method" (see chapter 2.1) the slip length was varied accordingly.

In the present study, different methods of calculating the access electrical resistance were investigated. Each method requires the access electrical resistance to be separable from the electrical pore resistance. In one method a distinction between the pore and access contributions to the total resistance is made by separating the potential drop over the pore from the potential drop over the reservoirs ("potential drop method"). The second assumes that the access electrical resistance does not depend on the pore length and that the electrical

pore resistance approaches zero in the limit of zero pore length ("length method"). The third method assumes that the slip length has no effect on the access electrical resistance, but that the electrical pore resistance approaches zero in the limit that the slip length approaches infinity ("slip method").

3.4   RESULTS AND DISCUSSION

3.4.1   *Charged pore in neutral membrane*

Figure 3.3 shows the access electrical resistance versus surface charge density for several different salt concentrations, calculated using the three methods, for a membrane with a neutral outer wall. The first thing to note is that under no conditions studied here do all three methods for calculating the access electrical resistance agree with each other.

The slip method may be immediately ruled out as a viable method for calculating the access electrical resistance. This is because it gives a much larger estimate of the access electrical resistance than is given by the Hall equation, even at high salt concentrations and low surface charge densities, where the Hall equation is expected to be most accurate. At high salt concentrations the solution at the pore entrances would have a similar conductivity to that of the bulk solution in the reservoirs. Furthermore, at low surface charge densities the assumption of equipotential surfaces at the pore ends is more accurate. The discrepancies may be due to the large solution fluxes that occur at high slip lengths. This would have an effect on the ion concentrations near the pore ends due to concentration polarization, which is an effect that can occur when ions flow at different rates through the pore relative to the bulk solution. This results in either a higher or a lower concentration at the pore entrances, depending on the direction of the flow and on the velocities of the ions in the pore relative to those the bulk reservoirs. Concentration polarization is a known contributor to the access electrical resistance.[37] Furthermore, the regime of infinite slip length is far from that of physical interest. This is because nonlinear effects on the flow are expected at such high flow rates.

The length method agrees reasonably well with the Hall equation for the highest three salt concentrations (3–30 mM), but deviates from it for the lowest two salt concentrations (0.1–1 mM). The salt concentrations at which this occurs correspond to situations where the Debye length is larger than the pore radius. For a salt concentration of 0.1 mM in water at 298 K the Debye length is $\approx$ 30 nm, which is six times the pore radius. When the Debye length is much larger than the pore radius the charge cloud within the pore spills out from
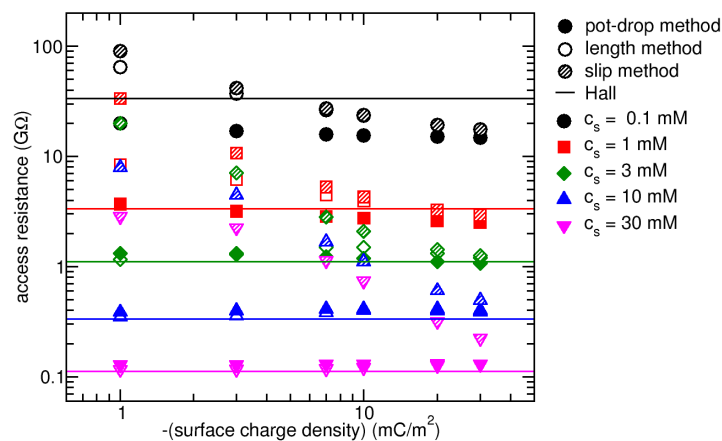
Figure 3.3: Access electrical resistance versus surface charge density for a charged pore in a neutral membrane calculated using different methods. The lines are from the Hall equation (equation (3.2)). The pore radius was 5 nm.

the ends of the pore. In ref. 25 it was shown that the charge spillage is equivalent to having a pore of shorter effective length than the actual pore length. Therefore, extrapolating the total resistance to zero actual pore length is equivalent to extrapolating it to a negative effective pore length. The effective length, as given in ref. 25, depends on the pore radius, the Debye length (which depends on the salt concentration), and on the pore length. So extrapolating with the actual pore length will not lead to accurate values of the access electrical resistance. This effect is less noticeable for the higher salt concentrations studied here, due to the Debye length being smaller than the pore radius.

In contrast to both the slip and length methods, the results of the potential drop method are more reliable as they do not rely on extrapolating the total electrical resistance but are calculated directly for a particular set of pore properties. Any effects of concentration polarization or charge spillage from the pore ends is a constant of the pore properties being studied. It makes no assumptions other than the access electrical resistance being decoupled from the electrical pore resistance. Furthermore, it has the added benefit of requiring less calculations than the previous two methods. The potential drop method also agrees with the Hall equation under the conditions where this equation is expected to be accurate. As a result of these factors, the access electrical resistance as calculated using the potential drop method is used in this analysis.

The potential drop method agrees well with the equation by Hall under all but the lowest salt concentration. At such a low salt concentration the effect of charge spillage from the pore ends has a significant impact on the access electrical resistance. Quantitatively, the amount of charge spilled from both pore ends is (for $\kappa L \gg 1$)[25]

$$q_{\text{overspill}} \approx -\frac{16\pi a \sigma}{4\kappa + \pi a \kappa^2}.$$

(3.9)

Therefore, when $a\kappa \ll 1$, $q_{\text{overspill}} \sim a\sigma/\kappa$, and so the degree of charge spillage has a strong dependence on the pore radius, the Debye length, and the surface charge density. Charge spillage leads to an accumulation of charge at the pore entrances, which reduces the access electrical resistance relative to the equation by Hall. In comparison, in ref. 37 similar salt concentrations were used and the access electrical resistance was calculated using the potential drop method. The results of this study showed that the calculated access electrical resistance was above the prediction given by the Hall equation. The difference between this study and ref. 37 is that the pore radius was comparable or larger than the Debye length in ref. 37, while in this study the pore radii are comparable or smaller than the Debye length. Extreme EDL overlap at the lowest salt concentration, resulting in significant charge spillage from the pore ends, causes a reduction in access electrical resistance relative to the predictions from the Hall equation. Ref. 37 also shows that the access electrical resistance is independent of the surface charge density, which is roughly true for the results obtained here.

Using the results obtained via the potential drop method, the access electrical resistance can seen to be roughly independent of surface charge density for a membrane with an uncharged outer wall. This is the same for all of the salt concentrations that were considered. This conflicts with the results in ref. 1, in which it was shown that the access electrical resistance depends strongly on the surface charge density. The method used to extract the access electrical resistance in that paper was the slip method, which is shown here to be inadequate. Therefore, a re-interpretation of the numerical results for the access electrical resistance in this particular paper are required.

Figure 3.4 shows the scaling of the access electrical resistance (calculated with the potential drop method) with salt concentration for several different pore surface charge densities. The first thing to note is that the equation by Hall agrees well with the FEM data. One of the assumptions made in deriving this equation is that the solution is uniform at the pore entrances. It might be expected that the presence of surface charges on the pore walls
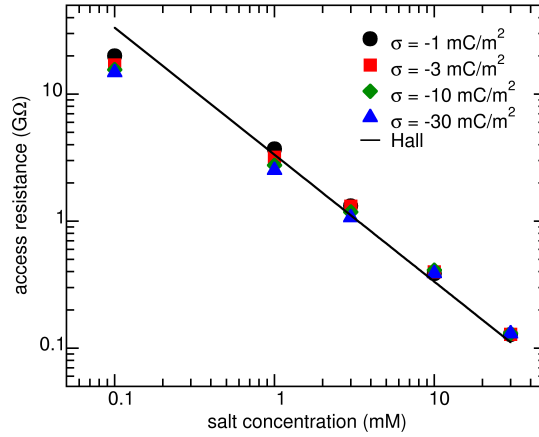
Figure 3.4: Access electrical resistance versus salt concentration for different surface charge densities for a charged pore in a neutral membrane. The points are calculated from FEM simulations using the potential drop method, while the line is from the Hall equation (equation (3.2)). The pore radius was 5 nm.

would affect this assumption. However, the surface charge density of the pore seems to have little effect on the access electrical resistance, particularly at high salt concentrations. At low salt concentrations there is a slight dependence on the surface charge density. As explained before, the degree of charge spillage depends strongly on the surface charge density when the pore radius is much smaller than the Debye length. This would likely explain the slight dependence of the access electrical resistance on the surface charge density at low salt concentrations.

Figure 3.5 shows the scaling of the access electrical resistance with pore radius for a salt concentration of 0.1 mM and a surface charge density of $-20 \, \text{mC m}^{-2}$. For large pore radii the Hall equation adequately describes the scaling of the access electrical resistance with pore radius. However, there are significant deviations from the theory at small pore radii. As explained before, there is a significant dependence of the amount of charge spilled from the pore ends when $a\kappa \ll 1$. On the other hand when $a\kappa \gg 1$, $q_{\text{overspill}} \sim -16\sigma/\kappa^2$ (ie. it reaches a plateau with respect to increasing pore radius). Therefore, the amount of charge spilled from the pore ends becomes insignificant compared with the amount of charge remaining in the pore (which increases with pore radius). This is supported by the fact that when the pore radius is larger than the Debye length ($\lambda_D \sim 30 \, \text{nm}$) the numerical data agrees very well with the theory. In spite of the deviations at low salt concentrations/small pore radii, the Hall equation does at least give an upper bound on the access electrical resistance and describes the scaling adequately under most of the conditions studied here. The conditions studied here correspond roughly to those used in ref. 40, in which it was shown that the Hall equation, along with a model for the pore electrical resistance, adequately describes the total electrical current for charged pores in neutral membranes. While the conditions are similar to those in ref. 40, the dependence of the access electrical resistance on surface charge density, salt concentration, and pore radius was not studied quantitatively in ref. 40, since only the total electrical resistance was measured in the FEM simulations in that work, nor was the effect of charge spillage from the pore ends discussed. The fact that the theory is able to adequately describe both the total electrical resistance and the access electrical resistance, and that the potential drop method agrees reasonably well with the length method under most of the conditions studied, supports the separability of the pore and access contributions to the total electrical resistance.

The main result shown here is that the access electrical resistance does not depend strongly on the pore surface charge density when the outer-membrane wall is neutral. As a result, the Hall equation (equation 3.2), which does not take into account the pore surface
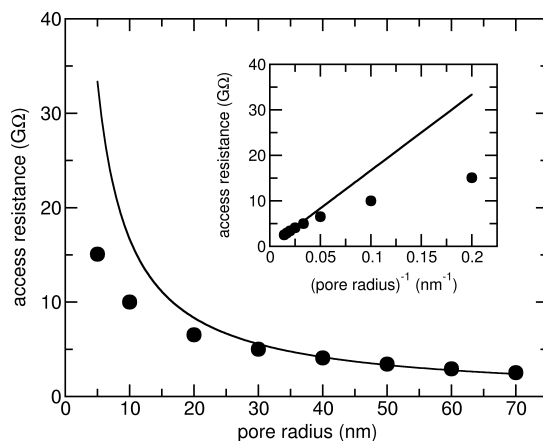
Figure 3.5: Access electrical resistance versus pore radius for a pore with a salt concentration of 0.1 mM, and a surface charge density of $-20\,\mathrm{mC\,m^{-2}}$ on the pore wall. The points are calculated from FEM simulations using the potential drop method, while the line is from the Hall equation (equation 3.2). Inset: access electrical resistance versus inverse pore radius.

charge density, agrees well with the numerical data even when the pore is quite charged. The exception to this is at very low salt concentrations when the Debye length is much larger than the pore radius. In this case the access electrical resistance may be reduced due to charge spillage from the pore ends.

3.4.2 *Charged pore in charged membrane*

When both the pore and outer-membrane walls are charged the situation is quite different. Figures 3.6 and 3.7 show the dependence of the access electrical resistance on surface charge density and salt concentration, respectively. In this case the equation by Hall fails to predict the scaling. On the other hand, the numerical results are adequately described using the equation by Lee et al.[7] (equation 3.4), with a numerical constant β equal to 1 instead of the value of 2 used by Lee et al. In their paper, Lee et al. verified their equation for a limited set of conditions. They considered surface charge densities ranging from 5 to 20 $\mathrm{mC\,m^{-2}}$, salt concentrations from 0.2 to 30 mM, and pore radii from 20 to 300 nm. While most of these conditions are similar to those used in the present study, the pore radii are around an order of magnitude larger than those considered here. Therefore, a different value of β was used here in order to fit the numerical results.

The equation by Lee et al. was derived assuming that the pore walls were charged, but did not take into account the charge of the outer-membrane walls. However, this equation shows significantly different scaling to the equation by Hall, which was shown in the previous section to adequately describe the access electrical resistance when the outer-membrane wall is neutral. The equation by Lee et al. does not make any assumptions about the charge on the outer-membrane wall, so the physical reason for its agreement with the numerical results for a charged-outer membrane wall and disagreement for an uncharged-outer-membrane wall is unclear.

Figure 3.8 shows the dependence of the access electrical resistance on the pore radius for different surface charge densities and a salt concentration of 0.1 mM. The equation by Lee et al. was used with different values of β to fit to the data. In general, a better agreement between the numerical results and the theory was achieved using $\beta = 1$. However, at the highest surface charge density, different values of β are required to achieve agreement with the numerical results for small versus large pore radii. This indicates that β is in fact not a numerical constant but that there is an additional radius-dependent scaling that is not
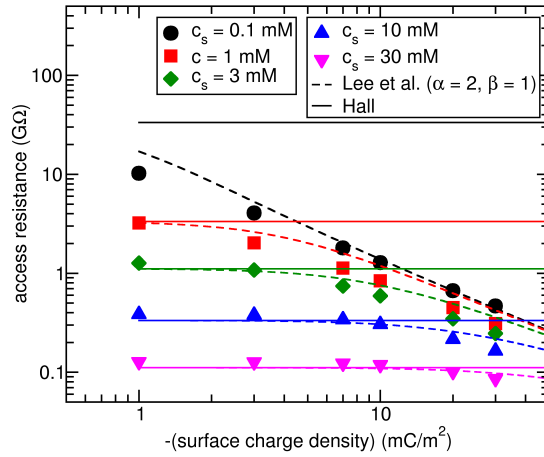
Figure 3.6: Access electrical resistance versus surface charge density using different salt concentrations for a charged pore and membrane wall. The points are calculated from FEM simulations using the potential drop method, while the solid and dashed lines are from the Hall equation (equation 3.2), and from the equation by Lee et al. (equation 3.4), respectively. The pore radius was 5 nm.
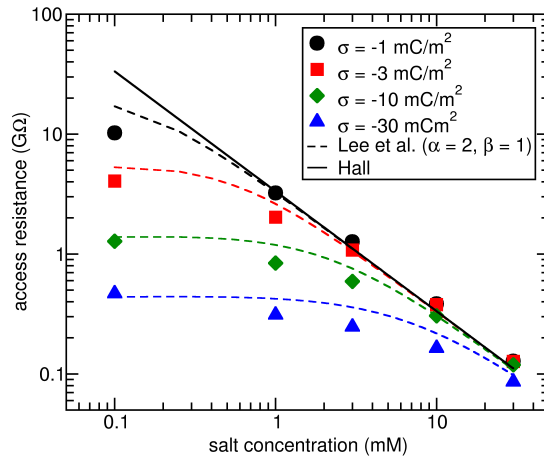
Figure 3.7: Access electrical resistance versus salt concentration for a charged pore and membrane wall. The points are calculated from FEM simulations using the potential drop method, while the solid and dashed lines are from the Hall equation (equation 3.2), and from the equation by Lee et al. (equation 3.4), respectively. The pore radius was 5 nm.
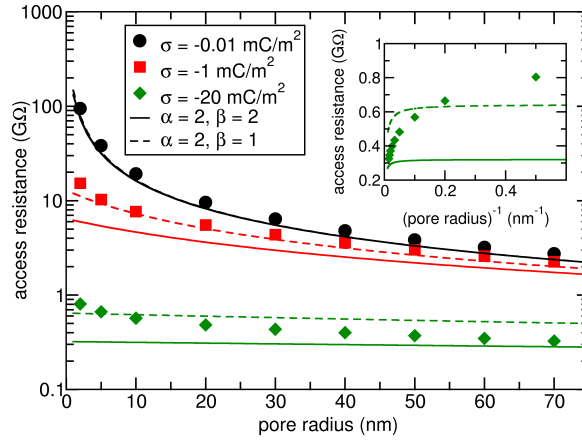
Figure 3.8: Access electrical resistance versus pore radius for different surface charge densities on the pore and membrane walls. The salt concentration was 0.1 mM. The points are calculated from FEM simulations using the potential drop method, while the lines are from the equation by Lee et al. (equation 3.4) with different values of β. Inset: access electrical resistance versus inverse pore radius for surface charge density of $-20\,\mathrm{mC\,m^{-2}}$.

accounted for by the theory. At the highest surface charge density ($-20\,\mathrm{mC\,m^{-2}}$) the Dukhin length is 10–100 times larger than the pore radius. In this regime the scaling is qualitatively incorrect, which is shown by plotting the access electrical resistance versus the inverse pore radius (Figure 3.8(inset)). Therefore, a more complete theory is required in order to properly understand this scaling.

3.4.3 *Theory of access electrical resistance of a charged membrane*

In order to derive an equation for the access electrical resistance of a charged membrane the electrical current through a circular orifice in an infinitesimally thin, charged membrane was considered (Figure 3.9). The total electrical resistance in this case can be considered to be twice the access electrical resistance. An analogous equation has previously been derived for the access hydraulic resistance by considering the fluid flux through a circular orifice due to a pressure gradient across an infinitesimally thin membrane.[41,44,45,82] For the present derivation the membrane is considered to have a surface charge density of σ and a pore radius of a. The current through the pore is I, and the electrical potentials far from the pore in the positive and negative z directions are, respectively, ϕ_+ and ϕ_-. A combination of cylindrical (r, z) and oblate spheroidal (ξ, η, θ) coordinates (Figure 3.10) were used to model the current flux. The relationship between these two coordinate systems is given by $r = a\cosh\xi\sin\eta$ and $z = a\sinh\xi\cos\eta$, where the oblate spheroidal coordinates (ξ, η, θ) are defined on the intervals $0 \le \xi < \infty, 0 \le \eta \le \pi, 0 \le \theta \le \pi$.[82] It is noted that Mao et al.[24] used this same membrane model to derive an equation for electro-osmosis (electric-field-driven fluid flow) across a circular orifice in an infinitesimally thin, charged membrane.

Consider an electrolyte with a fluid velocity $\boldsymbol{u}$, electrical potential ϕ, and salt concentration c_i of the ith ion. If the applied potential is assumed to be small compared with the equilibrium potential, then the lowest order terms of a perturbation expansion of the relevant variables can be considered by expanding in powers of $\gamma = e\Delta\phi/k_{\text{B}}T$:

$$\boldsymbol{u} = \boldsymbol{u}_0 + \gamma\boldsymbol{u}_1 + \gamma^2\boldsymbol{u}_2 + \cdots, \tag{3.10a}$$

$$\phi = \phi_0 + \gamma\phi_1 + \gamma^2\phi_2 + \cdots, \tag{3.10b}$$
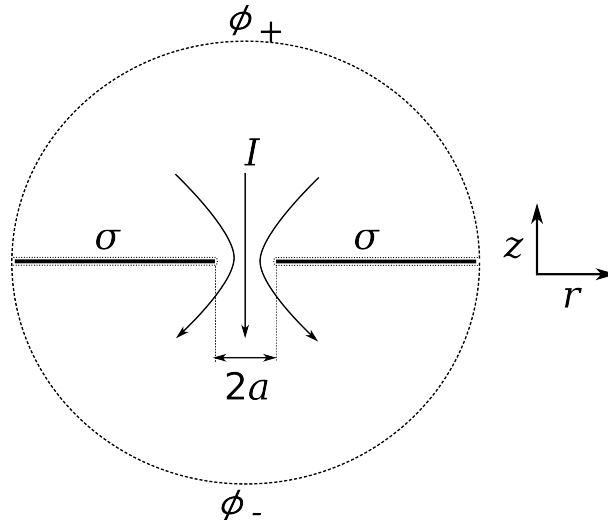
Figure 3.9: Current flow I through a circular orifice in an infinitesimally thin, charged membrane. The potentials far from the membrane pore in the positive and negative z directions are ϕ_+ and ϕ_-, respectively.
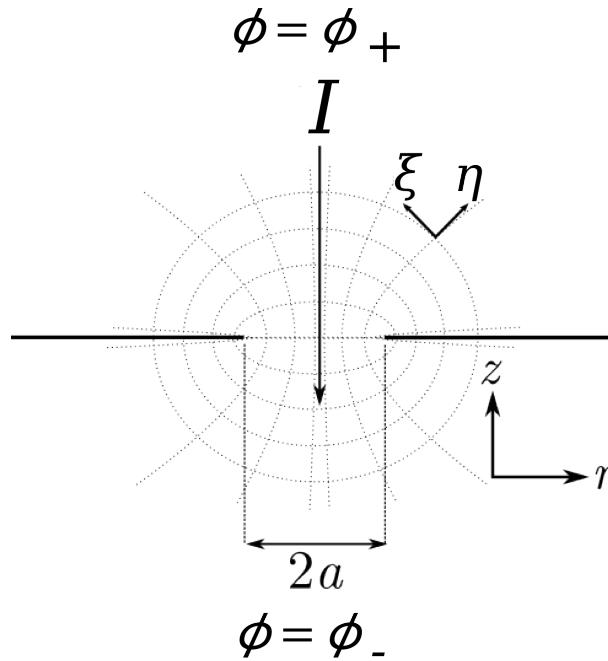
Figure 3.10: Diagram of oblate spheroidal (ξ, η, θ) coordinates.

and

$$c_i = c_{i0} + \gamma c_{i1} + \gamma^2 c_{i2} + \cdots , \qquad (3.10c)$$

where the subscripts refer to the different order terms in the expansion.[24] The subscript 0 refers to equilibrium quantities. The fluid velocity at equilibrium is $u_0 = 0$ because there is no applied field, while ϕ_0 and c_0 are the equilibrium electrical potential and salt concentration, respectively.

The current density of the ith ion j_i is given by the Nernst–Planck equation,

$$j_i = c_i u - Z_i e \lambda_i c_i \nabla \phi - D_i \nabla c_i, \qquad (3.11)$$

where Z_i, D_i, and λ_i are the valence, diffusivity, and the mobility of the ith ion, respectively. Substituting equation 3.10 into equation 3.11, and assuming a low Peclét number, the current density of the ith ion to $\mathcal{O}(\gamma)$ is:

$$j_i = -Z_i e \lambda_i c_{i0} \nabla \phi_1 - D_i \nabla c_{i1}. \tag{3.12}$$

In Mao et al.[24] the terms proportional to ϕ_1 and c_1 were collected into a single effective potential,

$$\chi = \phi_1 + \frac{1}{\kappa^2 k_B T} \sum_{i=1}^{N} e Z_i c_{i1}. \tag{3.13}$$

However, it is assumed that $\phi_0 \ll k_B T / e$. Therefore the second term in equation 3.13 is negligible, which means that $\phi_1 = \chi$. Using this result, and assuming the Einstein relation holds ($\lambda_i = D_i / (k_B T)$), the total electrical current density for a binary $Z{:}Z$ electrolyte with $i = \pm$ is

$$j = -\frac{e^2}{k_B T} (Z_+^2 D_+ c_{+0} + Z_-^2 D_- c_{-0}) \gamma \nabla \phi_1. \tag{3.14}$$

At equilibrium the concentration can be written as

$$c_{\pm 0} = c_{\pm \infty} e^{-Z_\pm e \phi_0 / k_B T}, \tag{3.15}$$

where $c_{\pm \infty}$ are the cation and anion concentrations far from the membrane surfaces, respectively. The current density may then be written as

$$j = -\frac{e^2}{k_B T} (Z_+^2 D_+ c_{+\infty} e^{-Z_+ e \phi_0 / k_B T} + Z_-^2 D_- c_{-\infty} e^{-Z_- e \phi_0 / k_B T}) \gamma \nabla \phi_1. \tag{3.16}$$

To calculate the total electrical current I the current density must be integrated over the entire surface area S of the orifice,

$$I = \iint_S \mathrm{d}s \, j \cdot \hat{n}, \tag{3.17}$$

where $\hat{n}$ is the normal to the orifice. Using the first order term in the electrical potential,[24]

$$\gamma \phi_1 = \frac{\Delta \phi}{2} \left[1 - \frac{2}{\pi} \tan^{-1} \left(\frac{1}{\sinh \xi} \right) \right], \tag{3.18}$$

where $\Delta \phi = \phi_+ - \phi_-$, the gradient in the potential is

$$\gamma \nabla \phi_1 = \hat{\xi} \frac{\Delta \phi}{a \pi} \frac{1}{(\cosh^2 \xi - \sin^2 \eta)^{1/2} \cosh \xi}, \tag{3.19}$$

where $\hat{\xi}$ is the unit vector in the ξ direction. Substituting equation 3.16 into equation 3.17, using equation 3.19 for the gradient in the potential, and integrating over the θ coordinate, the total electrical current through the orifice is given by

$$I = \frac{-2 a \Delta \phi e^2}{k_B T} \int_0^{\pi/2} \mathrm{d}\eta \, \sin \eta \left[Z_+^2 D_+ c_{+\infty} e^{-Z_+ e \phi_0(0,\eta)/k_B T} + Z_-^2 D_- c_{-\infty} e^{-Z_- e \phi_0(0,\eta)/k_B T} \right]. \tag{3.20}$$

The access electrical resistance can be calculated using $R_a = \Delta \phi / 2I$, which gives

$$R_a = \frac{1}{4a} \frac{k_B T}{e^2} \left\{ \int_0^{\pi/2} \mathrm{d}\eta \, \sin \eta \left[Z_+^2 D_+ c_{+\infty} e^{-Z_+ e \phi_0(0,\eta)/k_B T} \right. \right.$$
$$\left. \left. + Z_-^2 D_- c_{-\infty} e^{-Z_- e \phi_0(0,\eta)/k_B T} \right] \right\}^{-1}. \tag{3.21}$$

Equation 3.21 may be simplified by using a Taylor expansion of the exponential terms in the equation for the current density (equation 3.16),

$$
\boldsymbol{j} = -\frac{e^2}{k_\mathrm{B}T}\gamma\nabla\phi_1\left[(Z_+^2 D_+ c_{+\infty} + Z_-^2 D_- c_{-\infty}) - (Z_+^3 D_+ c_{+\infty} + Z_-^3 D_- c_{-\infty})\frac{e\phi_0}{k_\mathrm{B}T}\right.
$$
$$
\left. +\frac{1}{2}(Z_+^4 D_+ c_{+\infty} + Z_-^4 D_- c_{-\infty})\left(\frac{e\phi_0}{k_\mathrm{B}T}\right)^2 - \cdots\right].
\tag{3.22}
$$

The electrical current is then given by

$$
I = \frac{-2a\Delta\phi e^2}{k_\mathrm{B}T}\int_0^{\pi/2}\mathrm{d}\eta\,\sin\eta\left[(Z_+^2 D_+ c_{+\infty} + Z_-^2 D_- c_{-\infty})-\right.
$$
$$
(Z_+^3 D_+ c_{+\infty} + Z_-^3 D_- c_{-\infty})\frac{e\phi_0(0,\eta)}{k_\mathrm{B}T}+
$$
$$
\left.\frac{1}{2}(Z_+^4 D_+ c_{+\infty} + Z_-^4 D_- c_{-\infty})\left(\frac{e\phi_0(0,\eta)}{k_\mathrm{B}T}\right)^2 - \cdots\right].
\tag{3.23}
$$

Using equation 3.23 for the current, the access electrical resistance may be written as

$$
R_\mathrm{a} = \frac{1}{4a}\frac{k_\mathrm{B}T}{e^2}\left\{\int_0^{\pi/2}\mathrm{d}\eta\,\sin\eta\left[(Z_+^2 D_+ c_{+\infty} + Z_-^2 D_- c_{-\infty}) - (Z_+^3 D_+ c_{+\infty}+\right.\right.
$$
$$
\left.\left. Z_-^3 D_- c_{-\infty})\frac{e\phi_0(0,\eta)}{k_\mathrm{B}T} + \frac{1}{2}(Z_+^4 D_+ c_{+\infty} + Z_-^4 D_- c_{-\infty})\left(\frac{e\phi_0(0,\eta)}{k_\mathrm{B}T}\right)^2 - \cdots\right]\right\}^{-1}.
\tag{3.24}
$$

Equations 3.21 and 3.24 rely on an equation for ϕ_0. In the limit of low surface potentials the electrical potential corresponding to the equilibrium charge cloud is[83]

$$
\phi_0(r,z) = -\frac{\sigma a}{\epsilon\epsilon_0}\left[\int_0^\infty \mathrm{d}s\,\frac{J_1(as)J_0(rs)}{(\kappa^2+s^2)^{1/2}}e^{[(-\kappa^2+s^2)^{1/2}z]} - \frac{e^{-\kappa z}}{\kappa a}\right],
\tag{3.25}
$$

where J_0 and J_1 are Bessel functions of the first kind. In the limit of low surface potentials and highly overlapped EDLs ($a/\lambda_\mathrm{D} \ll 1$) the equilibrium potential can be simplified further to

$$
\phi_0 = \frac{\sigma}{\epsilon\epsilon_0\kappa} = \frac{\sigma}{\epsilon\epsilon_0\lambda_\mathrm{D}}.
\tag{3.26}
$$

Therefore, the access electrical resistance can be calculated from the total electrical current through an orifice in an infinitesimally thin charged membrane using different levels of approximations. Using equation 3.21 with equation 3.25 makes the assumption that the surface potential ϕ_surf is much less than the thermal voltage $k_\mathrm{B}T/Ze$ where $Z = \max\{|Z_+|, |Z_-|\}$ $\approx 26\,\mathrm{mV}$ for $Z = 1$ at 298 K. In the limit of low surface potentials the surface potential may be calculated using $\phi_\mathrm{surf} = \sigma\lambda_\mathrm{D}/(\epsilon\epsilon_0)$. This equation can be used to test whether the low surface potential assumption is accurate. Equation 3.21 with equation 3.26 uses this assumption as well as the assumption that the EDLs are highly overlapped inside the pore, which occurs when the Debye length is much larger than the pore radius. Lastly, equation 3.24 may be combined with equation 3.26 for the potential, which assumes a low surface potential, highly overlapped EDLs, and a series expansion for the current density. The regime for which the series expansion to the current density is accurate is investigated in this study. Using this last set of assumptions the access electrical resistance may be written

$$
R_\mathrm{a} = \frac{1}{4\kappa_\mathrm{b}a_\mathrm{eff}},
\tag{3.27}
$$

where a_{eff} is the effective pore radius given by

$$a_{\mathrm{eff}} = a \left[1 - 2 \left(\frac{D_+ - D_-}{D_+ + D_-} \right) \left(\frac{\lambda_{\mathrm{D}}}{l_{\mathrm{GC}}} \right) \mathrm{sgn}(\sigma) + 2 \left(\frac{\lambda_{\mathrm{D}}}{l_{\mathrm{GC}}} \right)^2 - \cdots \right], \qquad (3.28)$$

where $\mathrm{sgn}(\sigma)$ is given by

$$\mathrm{sgn}(\sigma) = \begin{cases} 1, & \sigma > 0 \\ 0, & \sigma = 0 \\ -1, & \sigma < 0 \end{cases}. \qquad (3.29)$$

The access electrical resistance of a charged membrane with low surface potentials and highly overlapped EDLs can therefore be considered equivalent to the Hall equation, but with an effective pore radius that depends on the ratio of the Debye length to the Gouy–Chapman length.

To verify the theory it was compared with FEM calculations of the access electrical resistance using the potential drop method. Figure 3.11 shows the dependence of the access electrical resistance on the surface charge density for a pore radius of 2 nm at three different salt concentrations. Firstly, considering equation 3.21 with equation 3.25 for the potential, which assumes a low surface potential ("low surf pot" in the legend), the theory agrees very well for the highest two salt concentrations, while for the lowest salt concentration the theory is only accurate for the smallest surface charge densities. The agreement between the theory and the FEM simulations is best for the lowest surface potentials (highest salt concentrations and lowest surface charge densities), while for the highest surface potentials (lowest salt concentrations and highest surface charge densities) the agreement is worse. Using equation 3.21 with equation 3.26 for the potential, which assumes low surface potentials and highly overlapped EDLs ("low surf pot + EDL" in the legend) shows similar agreement when the surface potential is low. Although the theory fails at high surface charge densities, this is also the regime where the access electrical resistance is small and can generally be neglected in practice. Importantly, the new theory provides a much better estimate of the access electrical resistance than the equation by Lee et al..

Figure 3.12 compares the theory curves calculated using varying levels of assumptions with the FEM data. Equation 3.21 is used with equation 3.26 for the potential, which assumes low surface potentials and highly overlapped EDLs. In addition to this, theory curves

Figure 3.11: Access electrical resistance versus surface charge density for different salt concentrations. The points are calculated from FEM simulations using the potential drop method. The solid lines are from equation 3.4 ("Lee, $\alpha = 2, \beta = 1$"), the dashed lines are from equation 3.21 with equation 3.25 for the potential ("low surf pot"), while the dash–dotted lines are calculated using equation 3.21 with equation 3.26 for the potential ("low surf pot + EDL"). The pore radius was 2 nm.

Figure 3.12: Access electrical resistance versus surface charge density for different salt concentrations. The points are calculated from FEM simulations using the potential drop method. The solid lines are predictions from the equation 3.21 with equation 3.26 for the potential ("low surf pot + EDL"), while the dashed and dotted lines are predictions using equation 3.24 to second and fourth order, respectively, with equation 3.26 for the potential ("low surf pot + EDL + SE2" and "low surf pot + EDL + SE4", respectively).

are also plotted using equation 3.24 with equation 3.26 for the potential, which as well as the previous assumptions use a series expansion for the exponential terms in the current density. The series expansion is truncated at second and fourth order. For the conditions where the low surface potential assumption holds the series expansion converges at second order, while outside of this regime the series expansion shows divergence. Therefore, the series expansion to the current density is a valid assumption to make when the surface potential is low, which is also the assumption made in calculating ϕ_0 from equation 3.26. Using equation 3.24 to second order with equation 3.26 for the potential, which assumes low surface potentials, highly overlapped EDLs, and a series expansion to the current density, gives similar agreement with the FEM data as equation 3.21 with equation 3.25 for the potential, which only assumes low surface potentials (ie. the theory with the fewest assumptions).

Figure 3.13 shows the access electrical resistance versus pore radius for a salt concentration of 0.1 mM at two different surface charge densities. The theory for a thin orifice in a charged membrane with the low surface potential assumption (equation 3.21 with equation 3.25 for the potential) is compared with the theory by Lee et al. (equation 3.4). The thin orifice theory agrees quantitatively with the FEM data, except for very small pore radii when the surface charge density is $-1\,\mathrm{mC\,m^{-2}}$. The surface potential for this curve is approximately $-44\,\mathrm{mV}$, which is nearly twice the thermal voltage. Therefore the discrepancy at small pore radii could be due to the fact that the low surface potential assumption is not being met. Despite this the thin orifice theory predicts the access electrical resistance much better than the equation by Lee et al. with $\beta = 2$, and interestingly agrees nearly perfectly with the equation by Lee et al. when using $\beta = 1$. This could explain why using the equation by Lee et al. with $\beta = 1$ for this set of parameters resulted fortuitously in the correct prediction for the access electrical resistance.

Both the theory by Lee et al. and the thin orifice theory considers the access electrical resistance to be reduced compared with the Hall equation (equation 3.2) by way of an effective pore radius, which when substituted into equation 3.2 provides the correct estimate of the access electrical resistance. For the theory by Lee et al. this effective pore radius for $\alpha = 2$ and $\beta = 1$ is

$$a_{\mathrm{eff}} = a + \frac{1}{4}l_{\mathrm{DU}}, \tag{3.30}$$
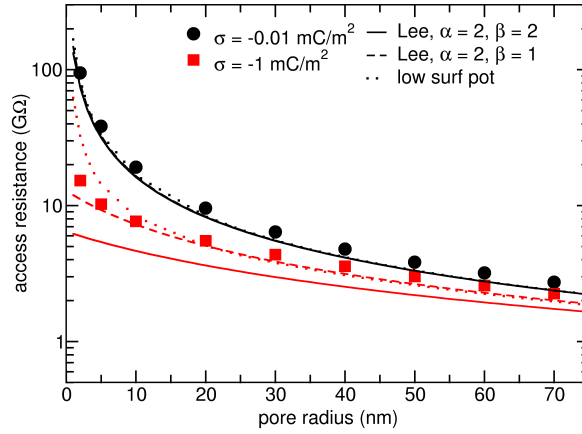
Figure 3.13: Access electrical resistance versus pore radius for different surface charge densities and a salt concentration of 0.1 mM. The points are calculated from FEM simulations using the potential drop method. The solid and dashed lines are predictions from equation 3.4 with $\beta = 2$ and $\beta = 1$, respectively ("Lee, $\alpha = 2, \beta = 2$" and "Lee, $\alpha = 2, \beta = 1$", respectively), while the dotted line is from equation 3.21 with equation 3.25 for the potential ("low surf pot").

while for the thin orifice theory derived in this thesis assuming low surface potentials, highly overlapped EDLs, and a series expansion to the current density, it is given by equation 3.28. Figure 3.14 shows the access electrical resistance divided by the bulk resistivity plotted against the inverse of the effective pore radius. The access electrical resistance is calculated using equation 3.24 with equation 3.26 for the potential ("low surf pot + EDL + SE2") and from equation 3.4 with $\beta = 1$ ("Lee, $\alpha = 2, \beta = 1$"). These are plotted against a_{eff} from the two theories. The surface charge density is $-3\,\text{mC}\,\text{m}^{-2}$, which for the lowest salt concentration corresponds to a surface potential of $-42\,\text{mV}$. Each equation predicts a universal curve for the access electrical resistance divided by the bulk resistivity versus the effective pore radius. However, only the thin orifice theory (equation 3.24 with equation 3.26 for the potential) adequately predicts the FEM results. For this theory the FEM results fall approximately onto a universal curve. Although the agreement is not perfect it does predict the FEM results much better than the equation by Lee et al. (equation 3.4). The scaling is not predicted properly by equation 3.4 for this set of parameters.

In the theory by Lee et al. the access electrical resistance is considered to be reduced compared with the equation by Hall by way of having an effective pore radius that depends on the Dukhin length. With $\beta = 1$ the effective pore radius from this theory is given by equation 3.30. If it is assumed that $l_{\text{GC}} \ll \lambda_{\text{D}}$, the Dukhin length can be written as $l_{\text{DU}} = 2\lambda_{\text{D}}^2/l_{\text{GC}}$. In this regime, the effective pore radius from the theory by Lee et al. is therefore $a_{\text{eff}} = a + \lambda_{\text{D}}^2/(2l_{\text{GC}})$. If equation 3.28 is used for the effective pore radius to first order, then the effective pore radius scales as $a_{\text{eff}} \approx a + \lambda_{\text{D}}a/l_{\text{GC}}$. Therefore, the equation by Lee et al. has an additional factor of $\lambda_{\text{D}}/(2a)$ in the second term in the effective radius, which may explain qualitatively why the access electrical resistance decreases more rapidly with pore radius in Figure 3.8 than what is predicted by equation 3.4. The theory by Lee et al. explains that the reduction in the access electrical resistance compared with the Hall equation is due to the discontinuity in surface conductance at the pore entrance, which results in a perturbation in the electrical field that extends far into the bulk reservoirs over a length scale given by the Dukhin length. Figure 3.15 shows the electric field lines and potential contours for a 5 nm pore with and without charge on the outer-membrane wall, while Figure 3.16 shows the same but for a 50 nm pore. The first thing to notice is that the perturbation in the electric field from the bulk applied field is only significant when the outer-membrane wall is charged, which explains qualitatively why the theory by Lee et al. does not work
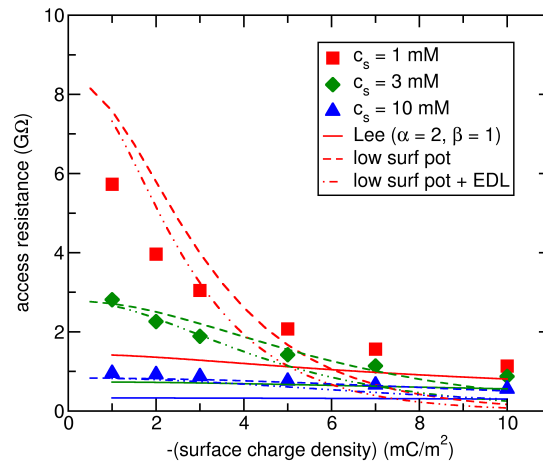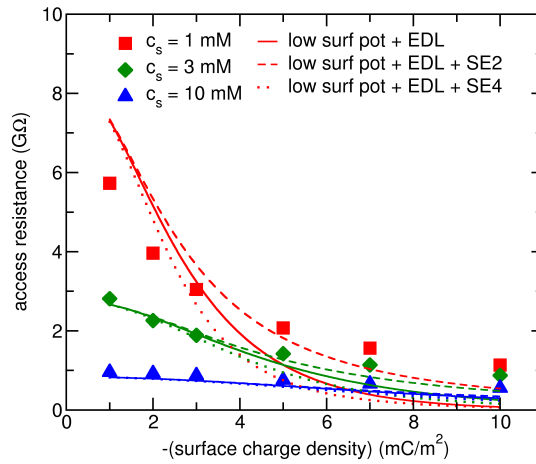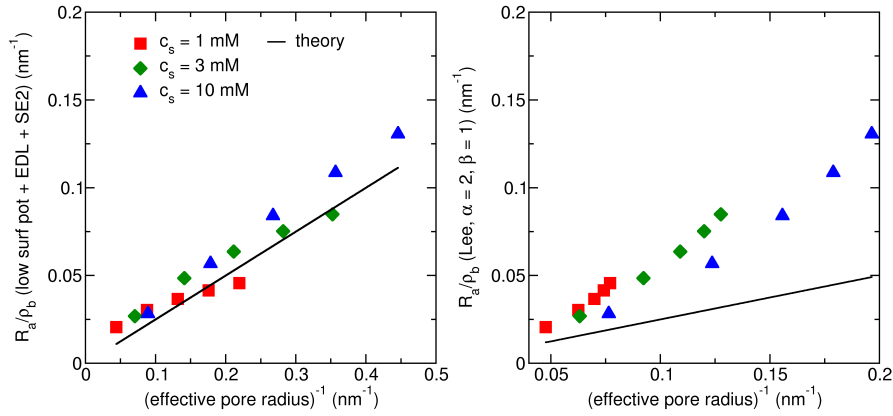
Figure 3.14: Scaled access electrical resistance versus inverse effective pore radius for different salt concentrations. The points are calculated from FEM simulations using the potential drop method, while the solid lines are the predicted universal curves from the two theories. The left subfigure shows the predictions from equation 3.24 with equation 3.26 for the potential, while the right subfigure shows the predictions from equation 3.4. The effective pore radius for the left subfigure was calculated using equation 3.28, while for the right subfigure it was calculated using equation 3.30. The surface charge density was $-3\,\mathrm{mC\,m^{-2}}$.

when the outer-membrane wall is neutral. Secondly, when comparing the perturbation in the electric field for the 5 nm pore with that of the 50 nm pore, the length scale of the decay in the potential it is not just proportional to the Dukhin length, which is constant for the two pores, but also depends on the pore radius. This also shows qualitatively that there is an extra radius-dependent factor that is not accounted for by the theory by Lee et al. but is accounted for by considering the charge flux through an infinitesimally thin orifice in a charged membrane.

The equation that was derived for the access electrical resistance in this study shows that the access electrical resistance depends on the ratio of the Debye length to the Gouy–Chapman length. In the regime where $l_{\mathrm{GC}} \ll \lambda_{\mathrm{D}}$ it was shown to depend on the Dukhin length and the ratio of the Debye length to the pore radius. The equations used to predict the equilibrium potential for the access electrical resistance using this theory assume a low surface potential, which means that the equation for the access electrical resistance cannot be used to adequately predict the access electrical resistance at high surface charge densities. However, if an equation for ϕ_0 is derived in the thin EDL limit, then equation 3.21 could possibly be used to accurately describe the access electrical resistance in the regime of high surface charge density. The thin orifice theory derived in this thesis accounts to some extent for the radius dependence of β shown in Figure 3.8, although the form of the equation that assumes low surface potentials, highly overlapped EDLs, and a series expansion to the current density is different from the equation by Lee et al. The access electrical resistance from the theory derived in this thesis, when scaled by the bulk resistivity and plotted against the effective pore radius forms a universal curve onto which the FEM results approximately fall. When carrying out the same procedure for the theory by Lee et al. the FEM results do not fall onto the universal curve. This verifies that the theory works to describe the access electrical resistance of a charged pore in a charged membrane. Overall the new theory adequately describes the scaling of the access electrical resistance with surface charge density and pore radius. In particular, it accounts for the surface charge on the outer-membrane wall, which is not taken into account in the equations by Hall or Lee et al. This equation shows that the access electrical resistance can be described by the electrical current through a circular orifice in an infinitesimally thin, charged membrane.
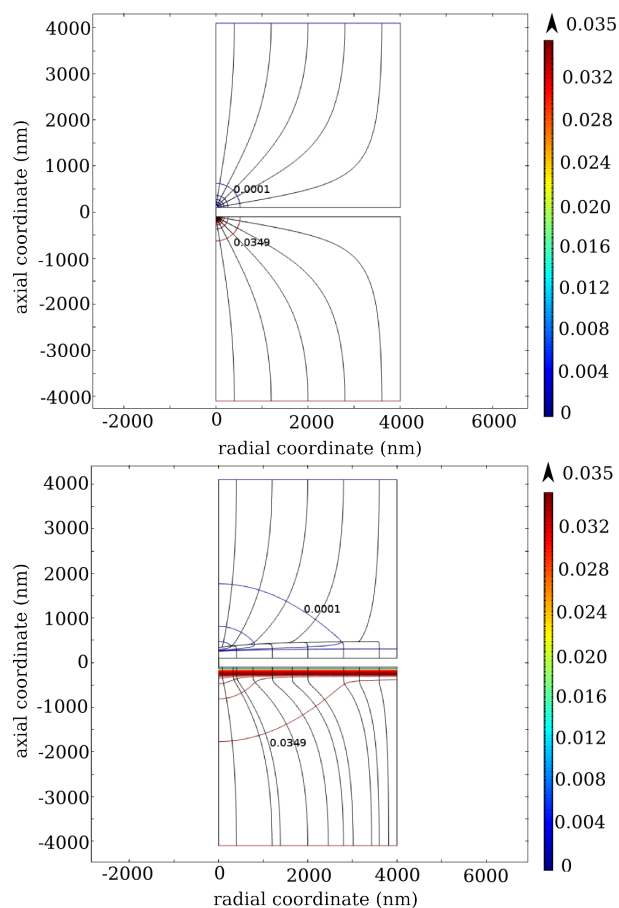
Figure 3.15: Electric field lines and potential contours at an applied potential of 35 mV for a pore with a radius of 5 nm, a length of 200 nm, using a salt concentration of 0.1 mM, and a surface charge density of $-7\,\text{mC}\,\text{m}^{-2}$ on the pore walls (top), and on the pore and membrane walls (bottom). The Dukhin length is 307 nm. The values for the potential in the legend, and on the graph, are in volts.
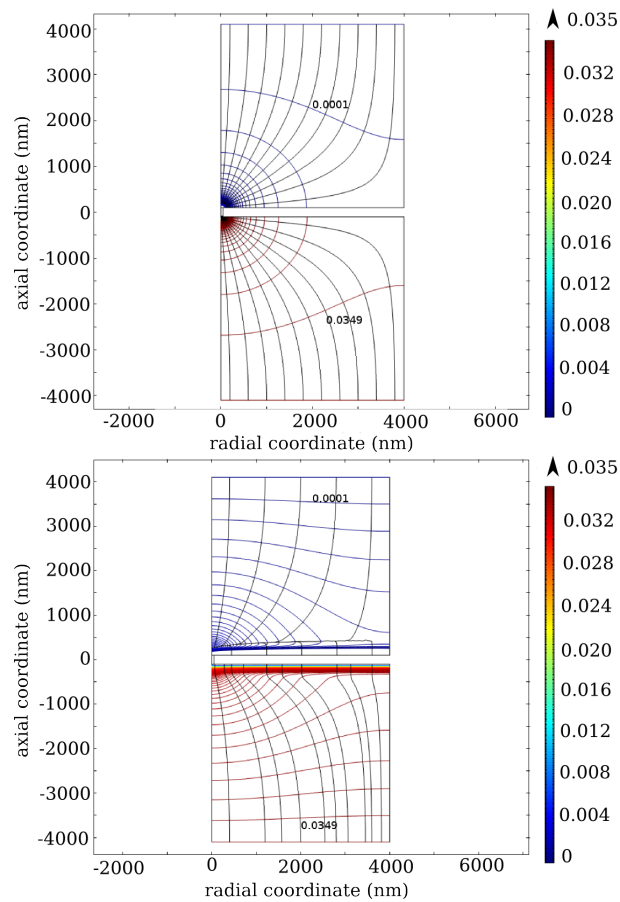
Figure 3.16: Electric field lines and potential contours at an applied potential of 35 mV for a pore with a radius of 50 nm, a length of 200 nm, using a salt concentration of 0.1 mM, and a surface charge density of $-7\,\mathrm{mC\,m^{-2}}$ on the pore walls (top), and on the pore and membrane walls (bottom). The Dukhin length is 307 nm. The values for the potential in the legend, and on the graph, are in volts.

3.5 CONCLUSION

The access electrical resistance of a nanopore immersed in an electrolyte was calculated from numerical solutions to the PNPS equations. Three different methods were used to separate the access electrical resistance from the total electrical resistance. The simplest and most reliable method was the one in which the average potential drop over the reservoirs was divided by the electrical current through the pore, called the potential drop method. This method was then used to calculate the access electrical resistance for different surface charge densities, salt concentrations, and pore radii, for charged pores with charged versus uncharged outer-membrane walls. It was found that, depending on whether or not the outer-membrane surface is charged, different scaling of the access electrical resistance is observed. When the pore is charged but the outer-membrane wall is neutral the access electrical resistance follows the equation derived by Hall for a neutral pore. In contrast to this, when both the pore and outer-membrane walls are charged, the access electrical resistance follows the equation derived by Lee et al., but with a radius-dependent numerical pre-factor. However, this was found to conflict with the assumptions made by Lee et al. in deriving their equation. They assumed that the pore was charged, but did not make any assumptions about the charge of the outer-membrane wall. Despite this, excellent agreement between their equation and the numerical results is shown here. However, the theory fails to describe the radius-dependence of the access electrical resistance when the pore was highly charged and the salt concentration was low. In particular, different values of a numerical pre-factor were required for narrow versus wide pores. As the pre-factor was found to be radius-dependent a more rigorous theory was derived. The access electrical resistance was considered to be half the total electrical resistance of a circular orifice in an infinitesimally thin charged membrane. The theory was found to agree quantitatively with FEM calculations carried out at low surface potentials but fails at high surface potentials, which was due to the assumptions made in calculating the equilibrium potential. Further assumptions were made to derive a closed-form analytical expression, being highly overlapped EDLs and a series expansion for the current density. This approximate theory was found to predict the FEM results better than the theory by Lee et al.. In both theories the access electrical resistance is considered to be reduced compared with the equation by Hall, which can be described by the pores having an effective radius, which when substituted into the Hall equation predict the correct values for the access electrical resistance. Both the theories therefore predict a universal curve when the access electrical resistance scaled by the bulk solution resistivity is plotted against the inverse effective pore radius, however only the thin orifice theory was found to accurately predict the FEM results. For future work, a theory for the access electrical resistance that works in the high surface charge regime may be derived using an equation for the equilibrium potential in the thin EDL regime.

MODIFIED CONSTRAINED CONCENTRATION-DIFFERENCE ALGORITHM

4.1 ABSTRACT

Molecular dynamics (MD) simulations of concentration differences applied across porous membranes can be beneficial for understanding solution transport across both biological and synthetic membranes. This is because concentration gradients are often the driving force for solution flows in these systems of both fundamental and practical interest. However, simulating concentration differences in MD is not straightforward. One of the reasons for this is that when periodic boundary conditions are applied to reduce finite-size effects, the high and low concentration sides of the membrane are in direct contact. This results in mixing across the periodic boundaries, which destroys the concentration difference. In this study a previously published algorithm for simulating a concentration difference in MD,[8] which addresses this issue, is used to simulate concentration-gradient-driven flows in the high solute-concentration regime, which is not well understood using continuum theory. The algorithm is found to require a modification at high concentrations that has not been previously considered. This modification generalises the algorithm for use in simulating concentration differences with arbitrary solute molar fractions.

4.2 INTRODUCTION

Concentration gradients drive flows of solution in natural systems, such as in the kidneys,[9] and in artifical systems, such as in synthetic membranes for harvesting energy from salinity gradients.[84] In general, these flows occur due to a combination of osmosis and diffusio-osmosis. Osmosis is driven by an osmotic pressure difference in the bulk solution, while diffusio-osmosis is driven by an osmotic pressure difference that develops within the thin interfacial fluid layer at the surface of the membrane pores where there is a net solute adsorption/depletion. The models used to understand these phenomena often assume that the fluid is a continuous medium, and that the solute particles are uncorrelated point particles. The latter assumption limits the application of the theory to the dilute (ideal) solution regime. It is difficult to derive accurate and general continuum equations for concentration-gradient-driven flow in the high concentration (non-ideal solution) regime, although recently there has been some progress in this area.[20,31] Furthermore, in pores with diameters less than around $1\,\mathrm{nm}$, or on the order of the solute or solvent molecular diameter, the continuum assumption breaks down. In contrast to continuum theory, molecular dynamics (MD) simulations are more amenable to studying concentration-gradient-driven flows in the non-ideal solution regime. This is because they do not rely on the definition of the chemical potential of the solute, which has no general equation in terms of its concentration in the non-ideal regime. Furthermore, the fluid particles can be considered explicitly, which avoids the need for the continuum assumption, which breaks down when the fluid is under extreme confinement.

In MD it is not trivial to simulate a concentration difference across a porous membrane. This is because the periodic boundaries connect the two solution phases together, which leads to the destruction of the concentration difference through mixing across the periodic boundaries (see chapter 1, Figure 1.8). Various methods exist for circumventing this problem. The simplest method is to restrict the periodic boundary conditions (PBCs) to the

directions lateral to the membrane and measure the transient fluxes of solution as the concentration gradient relaxes to equilibrium.[57] However, this suffers from a time-dependent concentration difference. Large reservoirs would be required in order to minimise this effect. A more feasible approach may be to employ a stochastic algorithm using a mixture of MD and Grand Canonical Monte-Carlo (GCMC) steps.[58–61] However, this relies on stochastically removing and inserting solute particles into a liquid, which is a very inefficient process due to the high rejection rate of particle insertions at liquid densities. On the other hand, there are several deterministic simulation algorithms available that work by applying an external field to the system in order to maintain a concentration difference/gradient.[8,31,63] The benefit of these deterministic algorithms is that they do not require computationally expensive reservoir sizes, the concentration differences are constant (when averaged over time), and there are no stochastic steps to interrupt the course of the deterministic MD simulations.

The previously published algorithm by Yoshida et al.[31] works by applying the same constant force to each solute particle, and the same counter-force to each solvent particle, such that a constant chemical potential gradient is simulated. However, it cannot be used when there are surfaces perpendicular to the applied chemical potential gradient. This is because it introduces a spurious force perpendicular to the surfaces that are not parallel to the applied chemical potential gradient as a result of the depletion or adsorption of solute particles at the surface. Therefore, it cannot be used to study end effects for membrane pores connecting two reservoirs. Furthermore, it does not explicitly simulate a concentration difference, and so cannot model variations in inter-particle correlations with solute concentration. For example, this algorithm would not model variations in the interaction length scale between the pore and an electrolyte solution with electrolyte concentration, which is known to affect flows like diffusio-osmosis.[22,23]

In this study, the deterministic algorithm by Khalili-Araghi et al.[8] is used to simulate concentration-gradient-driven flows across a nanopore connected to bulk solution reservoirs on either side (Figure 4.1). This algorithm, which was originally used to simulate concentration differences across biological pores in the dilute solution regime, is used to simulate concentration-gradient-driven flows in both the low and high concentration regimes in this study. Simulating concentration-gradient-driven flows in the high concentration regime is of interest due to the limitations of the continuum theory in this regime.

In order to test the ability of the algorithm to simulate concentration-gradient-driven flows, a theory for solution transport is required. Recently, Marbach et al.[20] derived equations for the total solution flux across a porous membrane due to a concentration gradient, generalised to the high-concentration regime. The assumptions they made included a fluid that is a continuous medium, a pore much wider than the width of the inhomogeneous
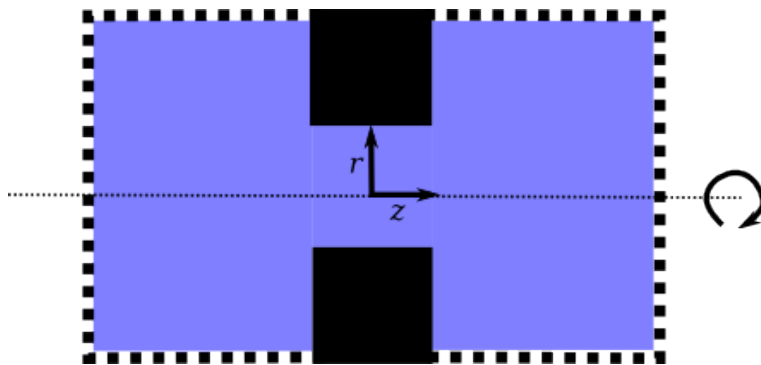

Figure 4.1: Cylindrically symmetric pore geometry for studying concentration-gradient-driven flow in MD. The radial coordinate is r, while the axial coordinate is z. The system is rotated about the axis of symmetry (shown as a dotted horizontal line). Solid lines indicate liquid–solid interfaces, while dashed lines indicate liquid–liquid interfaces.

fluid layer, and local thermodynamic equilibrium. The equations were further simplified by assuming that the solute mobility was independent of its concentration. In their theory they considered the combined effects of osmosis and diffusio-osmosis on the flow. The total solution flux Q from their theory is

$$Q = \mathcal{L}_{\text{hyd}}(\sigma_{\text{DO}} + \sigma_{\text{O}} - \sigma_{\text{DO}}\sigma_{\text{O}})\Delta\Pi, \tag{4.1}$$

where $\mathcal{L}_{\text{hyd}}$ is the permeance of the membrane, σ_{DO} and σ_{O} are the diffusio-osmotic and osmotic reflection coefficients, respectively, and $\Delta\Pi$ is the osmotic pressure difference. The osmotic reflection coefficient satisfies the condition $-1 \leq \sigma_{\text{O}} \leq 1$ and depends on the relative permeability of the membrane to the solvent and the solute. If $\sigma_{\text{O}} > 0$ then the membrane is more permeable to the solute than the solvent. A reflection coefficient of $\sigma_{\text{O}} = 1$ means that the membrane is completely impermeable to the solute. Similarly, if $\sigma_{\text{O}} < 0$ then the membrane is more permeable to the solute. The diffusio-osmotic reflection coefficient determines the strength and direction of the diffusio-osmotic flow, and depends on the degree of solute adsorption/depletion at the surface of the membrane pores. It is positive for a net solute depletion, and negative for a net solute adsorption. The equations for the reflection coefficients can be adapted from those derived in Yoshida et al.[31] for a slit pore, by assuming that the interaction length scale of the potential is small compared with the pore radius. The equation for the osmotic reflection coefficient is

$$\sigma_{\text{O}} = 1 - \frac{L}{\int_0^L \text{d}z \, c_{\infty,\text{res}}/c_{\infty}(z)}, \tag{4.2}$$

where L is the pore length, z is the coordinate along the pore axis, $c_{\infty,\text{res}}$ is the equilibrium solute concentration in the reservoirs far from any solid surfaces, and $c_{\infty}(z)$ is the equilibrium solute concentration far from any solid surfaces, which depends on the axial coordinate z. The equation for the diffusio-osmotic reflection coefficient is

$$\sigma_{\text{DO}} = -\frac{1}{\kappa_{\text{p}}} \int_0^{\infty} \text{d}r \, r \left(\frac{c(r,z)}{c_{\infty}(z)} - 1\right), \tag{4.3}$$

where κ_{p} is the permeability of the membrane ($\kappa_{\text{p}} = \mu L \mathcal{L}_{\text{hyd}}$, where μ is the fluid viscosity), r is the coordinate perpendicular to the pore wall, and $c(r,z)$ is the equilibrium solute concentration, which depends on r and z. The osmotic pressure difference is approximated by the nonlinear van't Hoff law at high concentrations, which was shown by Yoshida et al.[31] to be accurate for a Lennard-Jones fluid with a solute molar fraction of up to 0.48. The nonlinear van't Hoff law is

$$\Delta\Pi = k_{\text{B}}T(\rho_{\text{v,L}} \ln(1 - \chi_{\text{L}}) - \rho_{\text{v,R}} \ln(1 - \chi_{\text{R}})), \tag{4.4}$$

where k_{B} is Boltzmann's constant, T is the temperature, $\rho_{\text{v,L}}$ and $\rho_{\text{v,R}}$ are the solvent densities in the left and right reservoir, respectively, and χ_{L} and χ_{R} are the solute molar fractions in the left and right reservoirs, respectively. In the dilute solution regime the osmotic pressure difference is given by the linear van't Hoff law,

$$\Delta\Pi = k_{\text{B}}T\Delta c, \tag{4.5}$$

where Δc is the concentration difference between the two reservoirs on either side of the pore. In general, the direction of the flow is predicted by the sign of the overall reflection coefficient,

$$\sigma = \sigma_{\text{DO}} + \sigma_{\text{O}} - \sigma_{\text{DO}}\sigma_{\text{O}}. \tag{4.6}$$

If σ is positive, then the flow is from the low-concentration side of the membrane to the high-concentration side, and vice versa for a negative reflection coefficient. For $\sigma_{\text{O}} = 0$,

which is true in this study, since the pore radii are large enough that the pore is fully permeable to both solute and solvent, $\sigma = \sigma_{DO}$. While this theory is not expected to give perfect agreement with the MD results, due to end effects for example, it should at least predict the direction and approximate magnitude of the flow. Once it is verified that the algorithm works to simulate a concentration difference in the high-concentration regime, it can be used to study non-ideal effects on concentration-gradient-driven flows. Furthermore, it will allow the systematic investigation of the impact of entrance effects on concentration-gradient-driven flows (access diffusio-osmotic resistance), which is not taken into account in the theory by Marbach et al.

4.3 COMPUTATIONAL METHODS

4.3.1 *System details*

All MD simulations were performed using the LAMMPS software package (17 Nov 2016).[85] The time integration was carried out using the velocity-Verlet integrator. In this study the Lennard–Jones potential,

$$U_{ij}(r_{ij}) = 4\epsilon_{ij} \left[\left(\frac{\sigma_{ij}}{r_{ij}} \right)^{12} - \left(\frac{\sigma_{ij}}{r_{ij}} \right)^{6} \right], \tag{4.7}$$

was used to describe interactions between particles, where r_{ij} was the distance between particles i and j ($i, j \in w, f, s$, where w corresponded to the solid (wall) particles, f to the solvent (fluid) particles, and s to the solute particles), ϵ_{ij} was the well depth of the potential energy between particles i and j, and σ_{ij} was the distance between them at which the potential was equal to zero. Reduced Lennard–Jones units were used for all quantities such that all masses, distances, and energies were scaled by the reference Lennard–Jones parameters m, σ, and ϵ, respectively. These parameters, along with Boltzmann's constant were all set to 1. The temperature was scaled by ϵ/k_B, and the time units were scaled by the reference time $\tau = \sqrt{m\sigma^2/\epsilon}$. The potential was cut-off at a distance of 4σ, and the time step used in all simulations was 0.005τ.

The system comprised a single cylindrical nanopore between two solid sheets, solution particles on either side of the pore, and solid pistons at the ends of the simulation cell (Figure 4.2). The solid particles were placed on a face-centred cubic (FCC) lattice with a lattice constant of $\sqrt{2}\sigma$, while the solution particles were initially placed on a primitive cubic lattice. The solution initially comprised solvent particles only, a fraction of which were relabelled as solute particles after the equilibration. The Lennard–Jones parameters used for all particle–particle interactions, except for the solid–solute interactions, were set to $\epsilon_{ij} = \sigma_{ij} = 1$. The parameters for the solid–solute interactions were set to $(\epsilon_{sw}, \sigma_{sw}) = (0.5, 0.8)$, which corresponds to those used by Yoshida et al.[31] for repulsive solute–solid interactions. By using this set of parameters the solute and solvent particles were identical, except for their interaction with the solid.
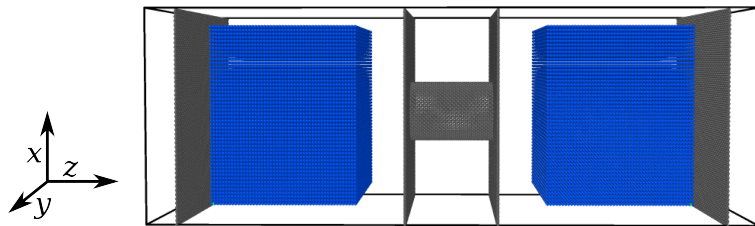
Figure 4.2: Initial particle positions for molecular dynamics simulations. The black particles represent the solid, while the blue particles represent the solution.

4.3.2 *Equilibration*

To equilibrate the system, periodic boundary conditions (PBCs) were used only in the lateral (x and y) directions. The solid pistons were used to compress the fluid into the pore such that it was equilibrated at the target density corresponding to the target pressure of ϵ/σ^3. Throughout the equilibration the temperature of the solution particles was maintained at a temperature of ϵ/k_B using a profile-unbiased thermostat (PUT). This thermostat acted only on the thermal particle velocities by subtracting out a background streaming velocity before the thermostat was applied (see chapter 2.2 for details). Once the system had reached equilibrium the pistons were removed, and the simulation cell was shortened in the axial (z) direction such that there were no gaps between periodic images (PBCs were applied in the axial direction following equilibration). After the equilibration a fraction of solvent particles in each reservoir were relabelled as solute particles. This was done such that both the desired solute molar fraction and concentration ratio was achieved. The system was then further relaxed for 10 000 time steps (no external forces applied). Although changing solvent particles into solute particles may cause the absolute pressure in the reservoirs to change from the set value (ϵ/σ^3) at high concentrations, due to the different interactions of the solute and the solvent with the solid surfaces, the target solution density remains the same. The density and temperature were maintained constant for all simulations.

4.3.3 *Constrained concentration-difference algorithm*

To constrain the concentration difference across the pore the algorithm by Khalili-Araghi et al.[8] was used. In their paper they referred to the algorithm as the non-periodic energy step method. This is because an energy step $\Delta\epsilon$ is applied to solute particles at the ends of the simulation cell over a region of width d in order to maintain a concentration ratio c_H/c_L between the reservoirs on either side of the porous membrane, c_H being the concentration of the high concentration reservoir, and c_L being the concentration of the low concentration reservoir. For a system of non-interacting (ideal) particles, the energy step that will induce this concentration ratio is given by

$$c_H/c_L = e^{\frac{\Delta\epsilon}{k_B T}}.$$
(4.8)

Therefore, an external force

$$f = k_B T \frac{\ln\left(\frac{c_H}{c_L}\right)}{d}$$
(4.9)

was initially applied to the solute particles within thin regions of width $d/2$ at the ends of the simulation cell in the z direction (Figure 4.3). This is the force required for non-interacting particles, which provides a good starting value for the algorithm. However, to account for the effects of particle–particle interactions the forces were adjusted dynamically throughout the course of the simulation according to

$$f(t + \Delta t) = f(t) + \frac{\Delta f(t)\Delta t}{\alpha \tau_c}$$
(4.10)

with

$$\Delta f(t) = -\frac{k_B T}{d}\left[\left\langle \ln\left(\frac{c_1}{c_2}\right)\right\rangle - \ln\left(\frac{c_H}{c_L}\right)\right],$$
(4.11)

where Δt was the time step, α and τ_c were tunable parameters, c_1 and c_2 were the instantaneous concentrations of the high and low concentration reservoirs, respectively, and the
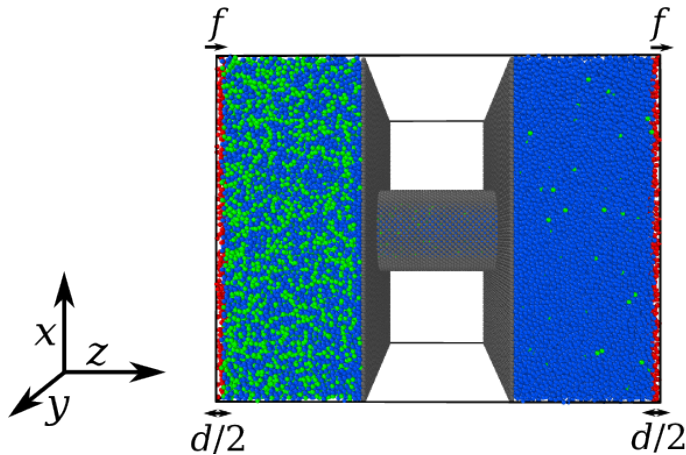
Figure 4.3: Illustration of forces applied to solute particles within transition regions for the constrained concentration-difference algorithm. Forces were applied to the solute particles, only within the regions of width $d/2$ at the ends of the simulation cell (shown in red). The black particles represent the solid, the blue particles the solvent, and the green particles the solute.

angled brackets indicate a time average over the last period of time τ_c. In the original application of the algorithm[8] the forces applied to the solute particles were updated every time step. However, here the forces were updated every $10\,000$ time steps, which was determined to be adequate for convergence of the simulations. The values for α and τ_c were tuned to balance convergence of the concentration gradient with simulation time. The values for α and τ_c used in this study were chosen to be 0.01 and 50, respectively, because they resulted in convergence of the concentration gradient within a reasonable simulation time ($\approx 6000\tau$).

The algorithm by Khalili-Araghi et al. does not refer to applying forces to any one particular species, and so it can be extended to applying forces to multiple species within a mixture. This is required from the Onsager[86] relations between fluid fluxes and external fields. The two fluxes that need to be maintained are the solute flux, and the solution flux. This requires two separate external fields to be constrained (ie. the concentration difference and the pressure difference). This was carried out by constraining the pressure difference to be zero, while constraining the concentration difference to the desired ratio.

To constrain the solution flux a force was also applied to the solvent particles within the transition region such that the pressure difference across the porous membrane was constrained to be zero. This was carried out by applying an initial force of $f = 0$ to the solvent particles within the transition region, and updating it according to equation 4.10, but with $\Delta f(t)$ given by

$$\Delta f(t) = \Delta p A / N_v^T, \tag{4.12}$$

where Δp was the difference in pressure between the reservoirs, A was the cross-sectional area of the simulation cell, and N_v^T was the number of solvent particles within the transition region averaged over the last period of time τ_c. Although this is not a new algorithm, it uses the algorithm by Khalili-Araghi et al. in a different way to the way in which it was applied in their paper (they only applied the forces to solute particles). Particular at high concentrations, applying forces to the solute particles does have an effect on the solution pressure. Therefore, the solution pressure must be constrained. This modified algorithm reduces to the unmodified algorithm (as used by Khalili-Araghi et al.) in the limit of infinitesimal solute molar fractions. This is because the pressure difference between the reservoirs tends to zero at low solute concentrations.

4.4 RESULTS AND DISCUSSION

Figure 4.4 shows the scaled equilibrium solute density profile within a nanopore for different solute molar fractions. The pore has a radius of 10.13σ and a length of 30.4σ, where σ is the Lennard–Jones distance unit. In this case, the total reflection coefficient (approximated by equation 4.6 with equation 4.3 and $\sigma_O \approx 0$) is positive. Therefore, the flow is predicted to go from the low concentration side to the high concentration side of the pore.

After this equilibration, a concentration ratio of $c_H/c_L = 50$ was applied to the system using the original constrained concentration-difference algorithm. However, the concentrations did not converge to those corresponding to the target concentration ratio, and a solution density gradient developed across the pore (Figure 4.5). This happened because at such a high solute concentration, applying a force to the solute particles exerts a net force on the solution, which in turn leads to a density difference across the pore. Figure 4.6 shows the resulting pressure difference between the two reservoirs on either side of the pore versus time. The pressures were measured far from the membrane walls so that they were not affected by the inhomogeneities in the fluid at the solid surfaces, and far from the regions where the external forces were applied. The pressure difference clearly converged to a non-zero value. In contrast, using the modified constrained concentration-difference algorithm resulted in the pressure difference converging to zero after around $40\,000\tau$ (Figure 4.7).

Figure 4.8 compares the axial solute and solution density profiles along the centreline of the nanopore resulting from both the unmodified and modified algorithms using a solute molar fraction of 0.2. From this figure it can be clearly seen that constraints must be applied to both the concentration and pressure differences at high concentrations. If the pressure difference is not constrained, then the concentrations do not converge to the target concentration ratio. Furthermore, a pressure difference is induced due to the force applied to the solute particles within the transition region. This occurs because the solute makes up a significant fraction of the total number of solution particles at high concentrations. In contrast, when the modified algorithm is used the correct concentration ratios and expected concentration variation as a function of the axial coordinate are achieved. Furthermore, there are no solution density gradients across the pore.

An additional test to make sure that the algorithm is producing physically meaningful results is to confirm that it correctly models the fluid dynamics. Under the conditions studied here continuum fluid dynamical equations are expected to be reasonably accurate. This is because the pore size considered is much larger than the characteristic sizes of the solution particles. Furthermore, they have been shown to be reasonably accurate at the high concentrations considered here.[31] One factor that is not considered by the model are end effects
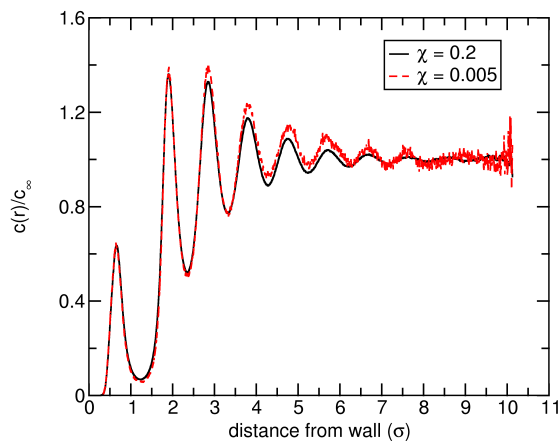
Figure 4.4: Scaled equilibrium solute density within nanopore versus radial distance from pore wall. The pore had a radius of 10.13σ and a length of 30.4σ.
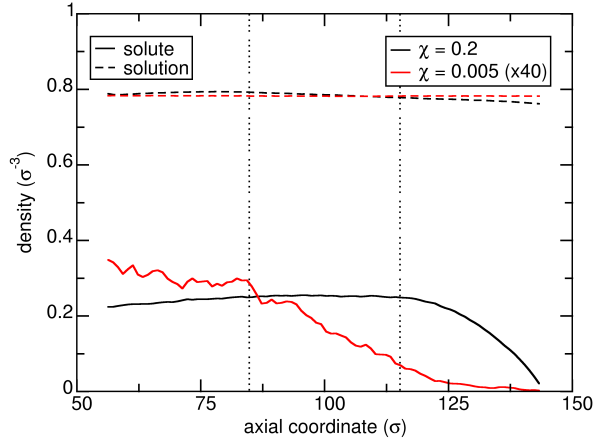
Figure 4.5: Solute/solution density profile along centreline of nanopore resulting from unmodified constrained concentration-difference algorithm at different solute molar fractions. The pore had a radius of 10.13σ and a length of 30.4σ. The applied concentration ratio was $c_H/c_L = 50$. The vertical dashed, black lines indicate the start and end of the nanopore. The solute density profile for $\chi = 0.005$ has been multiplied by 40 so that it can be compared with the results for $\chi = 0.2$.
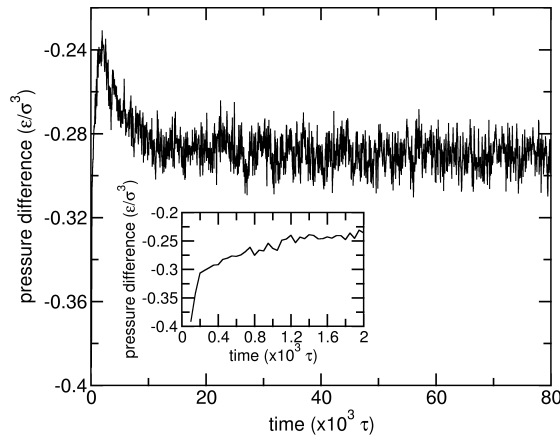
Figure 4.6: Difference in pressure between the reservoirs versus time resulting from the unmodified constrained concentration-difference algorithm with a solute molar fraction of $\chi = 0.2$. The pore had a radius of 10.13σ and a length of 30.4σ. The applied concentration ratio was $c_H/c_L = 50$. Inset: pressure difference at short times.

associated with finite pore lengths. However, for the purposes of validating the modified constrained concentration-difference algorithm they can be ignored, particularly as the pore length is around three times the pore radius. End effects are considered in more detail in chapter 5. Figure 4.9 compares the axial solution velocity profiles from both the unmodified and modified constrained concentration-difference algorithms. Without the modification the axial solution velocity profiles are parabolic (indicating a pressure-driven flow) and in the opposite direction to what is predicted from equations 4.1-4.4. Furthermore, when comparing the direction of flow with the direction of the pressure difference it is evident that these flows are due to the induced pressure differences resulting from the unmodified algorithm. In contrast, when the modified algorithm is used the axial solution velocity profiles agree well with continuum hydrodynamics equations 4.1-4.4 with $\sigma_O = 0$ (Figure 4.10).

Lastly, Figure 4.11 shows the total solution fluxes (scaled by the pore cross-sectional area) versus the continuum hydrodynamics equations for low ($\chi = 0.005$) and high ($\chi = 0.2$) solute molar fractions, with and without the modification to the algorithm. The results of the unmodified algorithm agree reasonably well with the theory for the low solute molar
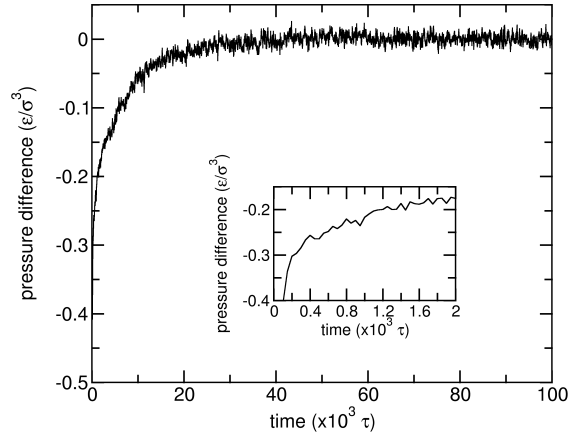
Figure 4.7: Difference in pressure between the reservoirs versus time resulting from the modified constrained concentration-difference algorithm at a solute molar fraction of $\chi = 0.2$. The pore had a radius of 10.13σ and a length of 30.4σ. The applied concentration ratio was $c_H/c_L = 50$. Inset: pressure difference at short times.
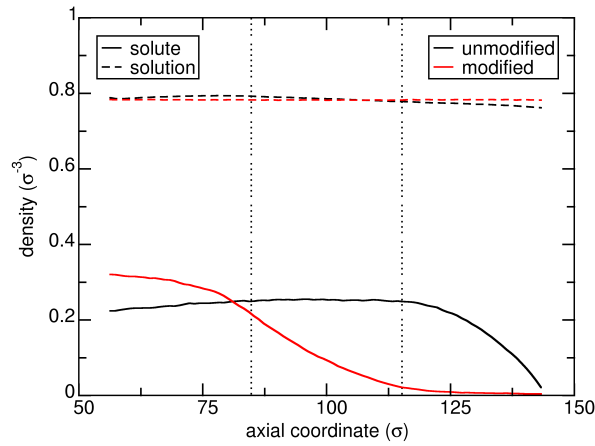
Figure 4.8: Solute/solution density profiles along centreline of nanopore resulting from the constrained concentration-difference algorithm at a solute molar fraction of $\chi = 0.2$, with and without the modification. The pore had a radius of 10.13σ and a length of 30.4σ. The applied concentration ratio was $c_H/c_L = 50$. The vertical dashed, black lines indicate the start and end of the nanopore.

fraction, while the fluxes for the high solute molar fraction are clearly incorrect both in sign and magnitude. On the other hand, the results for both high and low solute molar fractions agree well with the theory for the modified algorithm.

In the original constrained concentration-difference algorithm the pressure difference was not constrained. However, the study for which the algorithm was developed was concerned with simulating a concentration difference across a biological pore at relatively low solute concentrations. In the paper a solute concentration ratio of 1:0.1 M, a pore radius of ≈ 0.55 nm, and a length of ≈ 6 nm was considered. To maintain the concentration ratio across the pore an external force of 0.557 k/mol was applied to the solute particles within 2.5 Å wide regions at the ends of the simulation cell. This created a pressure difference across the OmpF pore of

$$\Delta p = p_T - p_B = nf/A, \tag{4.13}$$

where p_T is the pressure in the top reservoir, p_B is the pressure in the bottom reservoir, n is the number of solute particles within the transition regions, f is the applied force, and A is the cross-sectional area of the transition regions. Using $A = 123.5$ Å $\times$ 123.5 Å, the total
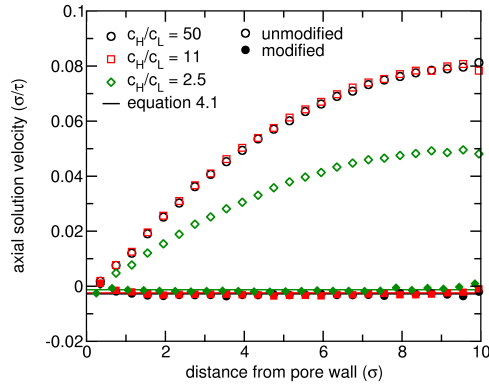
Figure 4.9: Axial solution velocity profiles for unmodified and modified constrained concentration-difference algorithms, using a solute molar fraction of $\chi = 0.2$. The points are from the MD simulations while the lines are the average axial solution velocity estimated from continuum hydrodynamics equations 4.1–4.4 (with $\sigma_O = 0$). The error bars were calculated using the method of block averaging.
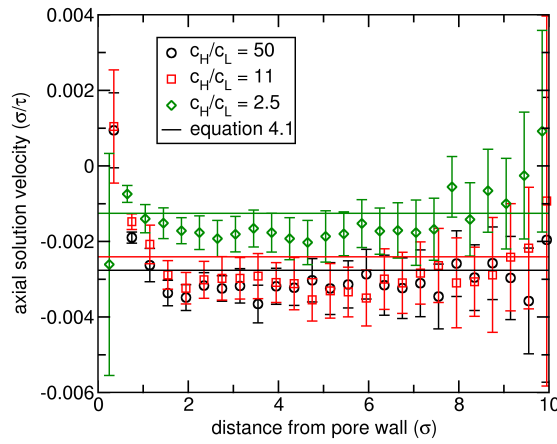
Figure 4.10: Axial solution velocity profiles for modified constrained concentration-difference algorithm, using a solute molar fraction of $\chi = 0.2$. The points are from the MD simulations while the lines are the average axial solution velocity estimated from continuum hydrodynamics equations 4.1–4.4 (with $\sigma_O = 0$). The error bars were calculated using the method of block averaging.
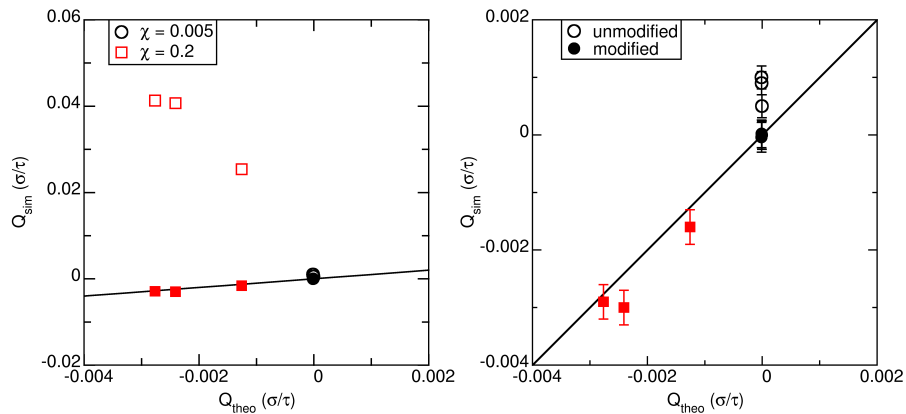
Figure 4.11: Total solution flux divided by pore cross-sectional area versus continuum hydrodynamical predictions from equations 4.1–4.4 (with $\sigma_O \approx 0$) for the unmodified and modified constrained concentration-difference algorithms for low and high solute molar fractions. A line intercepting the origin with a slope equal to unity is shown for the purpose of comparison. The left and right graphs show the same data but with different y-axis scales. The legends also correspond to both graphs. The error bars in the left graph are smaller than the symbols due to the y-axis range chosen.

transition region volume was $V = 5A = 76261$ Å^3 $= 7.626 \times 10^{-23}$ L. The total number of mole of solute in the transition regions was $n = cV = (0.1 + 1)V = 8.389 \times 10^{-23}$ mol ≈ 50 solute particles. Using equation 4.13, the induced pressure difference was $\Delta p = 2537$ Pa. The total flux resulting from Δp may be estimated from the Hagen–Poiseuille law,

$$Q = \frac{\Delta p \pi a^4}{8\mu L}. \tag{4.14}$$

Using this equation the solution flux induced by the algorithm is estimated to be (using $\mu = 8.94 \times 10^{-4}$ Pa s for water[80]) 1.7×10^{-23} m^3 s^{-1}. The average solute concentration is $c_{\text{ave}} = 0.55$ M. Therefore, the convective solute flux is estimated to be $J_{\text{convective}} = c_{\text{ave}}Q = 5630$ s^{-1}. In ref. 8 the lowest total ion current was ≈ 10 pA $= -6.24 \times 10^7$ s^{-1}. The convective flux was therefore only $\approx 0.009\%$ of the total ion flux. Therefore, the results of that paper are unaffected by the induced pressure differences resulting from using the unmodified algorithm. However, to investigate flows of high concentration solutions this modification is essential. This modification, which has not previously been considered, opens the door for simulating concentration-gradient-driven flow phenomena in non-ideal mixtures with arbitrary mole fractions, such as water–ethanol mixtures.[31] Furthermore, simulating a finite pore connected to bulk reservoirs allows for the investigation of end effects on diffusio-osmotic flow (access diffusio-osmotic resistance).

4.5 CONCLUSION

The constrained concentration-difference algorithm by Khalili-Araghi et al.[8] was used to simulate concentration-gradient-driven flows across a nanopore in the regime of high solute concentration. However, using the algorithm under these conditions resulted in a pressure difference across the pore. Due to this pressure difference the flow profile inside the pore was parabolic. This is inconsistent with the model for diffusio-osmosis, which assumes that there is no bulk pressure gradient across the pore. The resulting flow profile contrasted with both the direction and magnitude of the flow that was expected from the theory. By comparing the signs of both the pressure and concentration differences with the flow direction it was determined that the flow was a result of the induced pressure difference and not the concentration difference.

A modification to this algorithm was made that enabled it to be used at high concentrations. In this modification forces were applied to the solvent particles within the transition region such that the pressure difference across the pore converged to zero. Using the modified algorithm resulted in diffusio-osmotic flow profiles that agreed well with the theory. In comparing the total concentration-gradient-driven solution fluxes with the theory at both low and high solute molar fractions, it was found that the modification does not make much of a difference to the fluxes at low solute molar fractions, but is essential at high solute molar fractions. This modification therefore allows the simulation of concentration-gradient-driven flows using arbitrary molar fractions. Furthermore, due to its ability to simulate flow through a pore connected to bulk reservoirs, it allows for the systematic study of entrance effects on concentration-gradient-driven flows.

ACCESS DIFFUSIO-OSMOTIC RESISTANCE

5.1 ABSTRACT

Diffusio-osmosis is a surface-driven phenomenon by which a flow of fluid occurs relative to a solid surface due to a concentration gradient of solute. It differs from osmosis in that it is due to an osmotic pressure difference that develops only within a thin layer of fluid near the pore surface where there is a solute excess or depletion. The equations that are typically used to describe this phenomenon assume an ideal (dilute) solution. Also, entrance effects associated with the bending of fluid streamlines into the membrane pores from the bulk solution are generally not taken into account. In this study a continuum model for diffusio-osmosis is developed that takes into account entrance effects (access diffusio-osmotic resistance). The model uses approximate equations that are derived under the assumption of a dilute solution. The model is first validated by comparing it with finite-element method (FEM) calculations that assume a dilute solution. It is then compared with molecular dynamics (MD) simulations of diffusio-osmosis using a constrained concentration-difference algorithm at two different solute concentrations. This is done to investigate the effect of high solute concentrations and non-continuum effects (if any) on the access diffusio-osmotic resistance. The analytical equations, derived for the first time in this work, are found to show quantitative agreement with the FEM results in terms of the pore diffusio-osmotic resistance, and approximately the correct qualitative scaling for the access diffusio-osmotic resistance. Furthermore, the same scaling as given by the theory holds even for MD simulations carried out at high solute concentrations. Lastly, the relative effect of the access diffusio-osmotic resistance on the total diffusio-osmotic resistance is discussed, so that it can be understood in which regimes the access diffusio-osmotic resistance dominates.

5.2 INTRODUCTION

Diffusio-osmosis is a term given to the surface-driven fluid flux that occurs when a concentration gradient is applied across a porous membrane. The driving force for this flow is an osmotic pressure difference that develops within the inhomogeneous interfacial fluid layer induced by the pore surfaces. In general, whether the solute is adsorbed or depleted at the surface dictates the direction of the diffusio-osmotic flow. For an adsorbed solute the flow is in the opposite direction to the concentration difference (high to low concentration), while for a depleted solute it is in the same direction (low to high concentration).

The continuum theory-based models that are typically used to describe this phenomenon assume an ideal (dilute) solution. Marbach et al.[20] derived a continuum theory-based model that generalised the continuum equations used to model diffusio-osmotic flows at low solute concentrations to high solute concentrations. However, they did not consider entrance effects on solution transport.

For short pores and pores with low friction, solution transport is limited at the pore entrances by the bending of fluid streamlines from the bulk reservoirs into the narrow pore. This effect, called the access resistance, is fairly well understood in the context of pressure and electric-field-driven flows,[15,43,87] but not for diffusio-osmotic flows. In this study a continuum theory-based analytical model for diffusio-osmosis that takes into account the access diffusio-osmotic resistance is derived for the first time. The model is compared with FEM simulations and MD simulations. The MD simulations are carried out using the re-

cently modified constrained concentration-difference algorithm (see chapter 4) using pores of different lengths. These simulations allow the extrapolation of the total diffusio-osmotic resistance to the limit of zero pore length, giving the access diffusio-osmotic resistance. The theory is compared with the FEM and MD results, and any discrepancies are discussed. In this study it is of interest to investigate non-continuum effects (if any). Non-continuum effects have been previously shown to be potentially useful. For example, carbon nanotubes with diameters less than $1\,\mathrm{nm}$, for which the continuum assumption is expected to break down,[51] have been shown to have both high water permeabilities and a high ion selectivity at salinities that exceed that of seawater.[88] This makes them potentially useful for applications such as water desalination. Further to non-continuum effects, it is of interest to study solution transport in the high concentration regime. This is because the equation of state that relates the chemical potential to the concentration is not expected to be accurate at very high concentrations. Lastly, the relative effect of the access diffusio-osmotic resistance on the total diffusio-osmotic resistance will be discussed.

5.3   COMPUTATIONAL METHODS

5.3.1   *Finite element method calculations*

For the continuum model, a low Reynolds number was assumed, $Re = \rho u_0 a / \mu$, where ρ is the fluid density, u_0 is the characteristic fluid velocity within the pore, a is the pore radius, and μ is the fluid viscosity. This is justifiable for nanoscale flows as these are generally dominated by viscous forces. An incompressible Newtonian fluid was also assumed, which means that the shear stress was assumed to be linearly related to the strain rate, a reasonable assumption for liquids such as water. Lastly, the flow was assumed to be steady. The Stokes equation for the fluid velocity is

$$-\nabla p - c\nabla U + \mu \nabla^2 \boldsymbol{u} = 0, \tag{5.1}$$

the continuity equation for incompressible fluid flow is

$$\nabla \cdot \boldsymbol{u} = 0, \tag{5.2}$$

and the continuity equation for the solute current (for a single neutral solute) is

$$-\nabla \cdot \boldsymbol{j} = -\nabla \cdot (-D\nabla c - \lambda c \nabla U + \boldsymbol{u}c) = 0, \tag{5.3}$$

where p is the fluid pressure, c is the solute concentration, U is the potential acting on the solute by the surface of the membrane pores, μ is the shear viscosity of the solution, $\boldsymbol{j}$ is the solute flux density, D is the solute diffusivity, and λ is the solute mobility. The interaction potential between the pore/membrane walls and the solute was modelled using a hyperbolic tangent function,

$$U(r_{\mathrm{w}}) = \frac{\epsilon_{\mathrm{sw}}}{2}\left[-1 + \tanh\left(\frac{r_{\mathrm{w}} - \sigma_{\mathrm{sw}}}{\sigma_{\mathrm{sw}}}\right)\right], \tag{5.4}$$

where r_{w} is the distance from the membrane surfaces, and ϵ_{sw} and σ_{sw} are the parameters describing the strength and range of the potential between the solute and the wall. The values of ϵ_{sw} and σ_{sw} were chosen to represent a solute depletion at the pore and outer-membrane surfaces.

Equations 5.1–5.4 were solved using FEM calculations with COMSOL Multiphysics® version 4.3a[65]. The equations were solved using a fully coupled solver, which is a damped version of Newton's method. The damping option used to achieve convergence was "Automatic highly nonlinear (Newton)". The direct solver used was the MUMPS direct solver.[89] A

Table 5.1: Boundary conditions used to solve continuum equations for diffusio-osmosis of a neutral solute. The energy and length values are in units of ϵ and σ, respectively. The vector $\hat{n}$ is the surface normal, while superscripts I and II refer to phases I and II, respectively.

Boundary	Conditions
AH	$\hat{n} \cdot \nabla c = \hat{n} \cdot \boldsymbol{u} = \hat{n} \cdot \nabla \boldsymbol{u} = 0$
AB	$c = c_L,\ p = \Delta p$
GH	$c = c_R,\ p = 0$
BC and FG	$\hat{n} \cdot \boldsymbol{j} = \hat{n} \cdot \boldsymbol{u} = \hat{n} \cdot \nabla \boldsymbol{u} = 0$
CD, DE, and EF	$\hat{n} \cdot \boldsymbol{j} = \hat{n} \cdot \boldsymbol{u} = 0$

parametric sweep was used to vary parameters that affect geometry and mesh generation, and the parametric continuation solver was used to vary all other parameters. Figure 5.1 shows the geometry that was used to solve equations 5.1–5.4. The corners D and E were given a radius of curvature to avoid discontinuities in the potential. The radius of curvature was chosen to be much smaller than the length scale of the potential between the solute and the solid surfaces. Table 5.1 lists the boundary conditions that were used to solve the equations. The parameters used in the simulations are listed in Table 5.2.

To check that the FEM simulation results are correct the diffusio-osmotic resistance was calculated using both concentration-gradient-driven and pressure-driven flow simulations. This is possible using the Onsager reciprocity relations,[86] which allow the total solution flux due to a concentration difference to be related to the excess solute flux due to a pressure difference in the regime where the fluxes respond linearly to the applied fields. The solution and solute fluxes are related to the pressure and concentration differences by[23]

$$\begin{bmatrix} Q \\ J - c_\infty Q \end{bmatrix} = \begin{bmatrix} M_{11} & M_{12} \\ M_{21} & M_{22} \end{bmatrix} \begin{bmatrix} -\Delta p \\ -k_B T \Delta c / c_\infty \end{bmatrix}, \tag{5.5}$$

where Q is the solution flux, J is the solute flux, c_∞ is the average solute concentration far from any solid surfaces, M_{ij} are the transport coefficients, p is the fluid pressure, and c is the solute concentration. Using the Onsager reciprocity relations the relationship between the transport coefficients for the pressure-driven solute excess flux ($J - c_\infty Q$) and the diffusio-
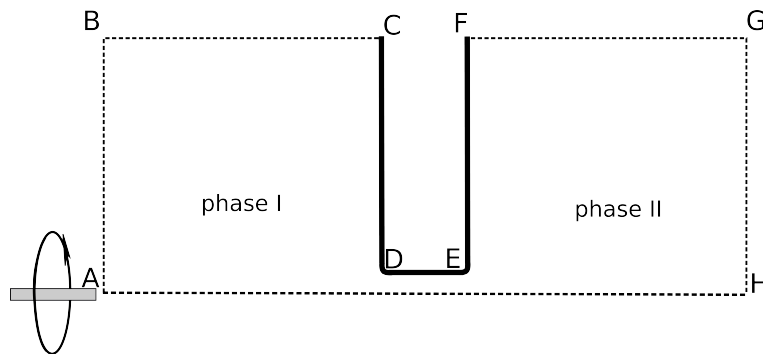

Figure 5.1: Cylindrical pore geometry used to solve continuum equations for diffusio-osmosis of a neutral solute. The boundaries CDEF represent the solid membrane and pore surfaces (solid lines), while the other boundaries are liquid–liquid boundaries (dashed lines). The geometry has rotational symmetry about the boundary AH. The points D and E have a radius of curvature.

Table 5.2: Parameters used for FEM calculations of diffusio-osmotic flows. Specific values are specified in the main text. Lengths and energies are given in Lennard-Jones units of σ and ϵ, respectively.

Quantity	Symbol	Value
pore radius	a	1.84–10.13σ
pore length	L	0.2σ, 30.4σ
potential well depth	ϵ_{sw}	-2.84–-1.42ϵ
potential length parameter	σ_{sw}	0.52–1.52σ
solution density	ρ	$0.78\sigma^{-3}$
solution temperature	T	ϵ/k_{B}
solution viscosity	μ	$1.8\epsilon\tau\sigma^{-3}$
diffusivity of solute	D	$0.079\sigma^2/\tau$
average concentration	c_{ave}	$0.00285\sigma^{-3}$
applied concentration difference	Δc	0–$0.04c_{\text{ave}}$
applied pressure difference	Δp	0–$4\times10^{-6}\sigma^{-3}$
radius of curvature	a_{curve}	0.092σ
reservoir radius	W_{res}	4000σ
reservoir length	L_{res}	4000σ

osmotic solution flux is $M_{12} = M_{21}$. The total diffusio-osmotic resistance can be defined in terms of the fluid flux Q induced by a concentration gradient by

$$R_{\text{T}} = \frac{\Delta c}{Q}. \tag{5.6}$$

Therefore, from equation 5.5 and the reciprocity relation, by measuring the solute excess flux $J - c_\infty Q$ for different applied pressure differences in the absence of a concentration difference the total diffusio-osmotic resistance can also be calculated from

$$R_{\text{T}} = \frac{c_\infty}{k_{\text{B}}T} \frac{\Delta p}{(J - c_{\infty Q})}. \tag{5.7}$$

To calculate the access diffusio-osmotic resistance from the FEM simulations the total diffusio-osmotic resistance was calculated using equations 5.6 and 5.7 for a circular orifice in a very thin membrane ($L = 0.2\sigma$), the width of which was smaller than σ_{sw}. This was done by fitting a line to the solution flux versus concentration difference data, or the solute excess flux versus pressure difference data, and taking the inverse of the slope of the line. The total diffusio-osmotic resistance across the thin orifice was then halved to give the access diffusio-osmotic resistance of a single pore entrance.

5.3.2 *Molecular dynamics simulations*

The details of the systems simulated are equivalent to those in chapter 4, but in this study the pore length, pore radius, and solute concentration were varied systematically in order to investigate the effect of the access diffusio-osmotic resistance. Table 5.3 lists the parameters used in the MD simulations in this study. For comparison with continuum theory the pore radii were defined as $a = a_{\text{c}-\text{c}} - d_{\text{shear}}$, where $a_{\text{c}-\text{c}}$ was the pore radius defined by the radial distance from the pore centre to the centre of the solid particles of the pore wall, and d_{shear} was the distance of the shear plane from the wall (the distance from the walls at which the fluid velocity vanished). Similarly, the lengths were calculated using $L = L_{\text{c}-\text{c}} + 2d_{\text{shear}}$,

Table 5.3: Parameters used in MD simulations of diffusio-osmosis. The pore radii and lengths listed are those measured with respect to the shear plane in order to compare with the continuum simulations and theory. All Lennard–Jones length parameters and well depths were equal to σ and ϵ, respectively, except for the solute–wall parameters.

Quantity	Symbol	Value
Lennard–Jones length parameter (solute–wall)	σ_{sw}	0.8σ
Lennard–Jones well depth (solute–wall)	ϵ_{sw}	0.5σ
pore radius	a	$4.48\text{–}9.43\sigma$
pore length	L	$3.52\text{–}31.8\sigma$
solution density	ρ	$0.78\sigma^{-3}$
solution temperature	T	ϵ/k_{B}
solution viscosity	μ	$1.8\epsilon\tau\sigma^{-3}$
diffusivity of solute	D	$0.079\sigma^2/\tau$
solute molar fraction	χ	$0.1, 0.2$
concentration ratio (high:low)	R	50
reservoir lateral width/height	W_{res}	70.7σ
reservoir length	L_{res}	50σ

where $L_{\text{c−c}}$ was the centre-to-centre distance between the wall particles comprising the solid membranes on either side of the pore. The distance of the shear plane from the wall was determined from the solution velocity profiles within the pores (Figure 5.2). Its value was found to be 0.7σ.

To calculate the total diffusio-osmotic resistance from the MD simulations the total solution flux was plotted against the applied concentration difference. The total diffusio-osmotic resistance was then calculated from the inverse of the slope of a linear fit to the data using equation 5.6. The total solution flux was calculated from the average solution particle velocity in the pore multiplied by the pore cross-sectional area,

$$Q = \frac{A}{N_{\text{pore}}} \sum_{i \in \text{pore}} v_{z,i}, \tag{5.8}$$

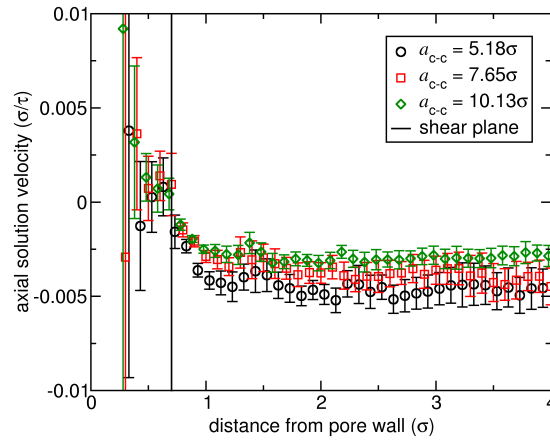Figure 5.2: Solution velocity versus distance from pore wall and location of shear plane for different pore radii. The pore length was 30.4σ, the solute molar fraction was 0.2, and the solute concentration ratio was $c_{\text{H}}/c_{\text{L}} = 50$. The distance of the shear plane from the pore wall was found to be 0.7σ.

where N_{pore} is the total number of solution particles in the pore, $v_{z,i}$ is the velocity of the ith particle in the z (axial) direction, and A is the pore cross-sectional area.

For the total resistance to the solute flux $R_{\text{T,s}}$ only the diffusive solute flux J_{diff} was used as the solute concentrations were high enough that the low Péclet number assumption did not hold. The total resistance to the solute flux was calculated using the equation

$$R_{\text{T,s}} = \frac{\Delta c}{J_{\text{diff}}}. \tag{5.9}$$

The diffusive solute flux was calculated from

$$J_{\text{diff}} = J - c_\infty Q, \tag{5.10}$$

while the total solute flux was calculated from the sum of the solute particle velocities in the pore divided by the pore length,

$$J = \frac{1}{L} \sum_{i \in \text{pore} \cap \text{solute}} v_{z,i}. \tag{5.11}$$

The access diffusio-osmotic resistance was calculated by extrapolating the total resistance to the limit of zero pore length and dividing the result by two,

$$R_{\text{a}} = \frac{1}{2} \lim_{L \to 0} R_{\text{T}}(L), \tag{5.12}$$

where R_{a} is the access diffusio-osmotic resistance and $R_{\text{T}}(L)$ is the total diffusio-osmotic resistance that depends on the pore length L, and similarly for the access resistance to the solute flux.

5.4   THEORY

To derive transport equations for diffusio-osmosis that take into account entrance effects, the resistance of a long cylindrical pore and of a circular orifice in an infinitesimally thin membrane were considered. The total resistance of a membrane comprising a single pore of finite length was approximated as the resistance of a cylindrical pore with no ends of the same length as the pore in the membrane added in series to the resistance of a circular orifice in an infinitesimally thin membrane.

5.4.1   *Fluxes through long, cylindrical pore*

Consider the fluxes through a cylindrical pore with no ends (Figure 5.3). The pore length L is assumed to be much larger than the pore radius ($L \gg a$).

The radial solute flux is assumed to be much smaller than the axial solute flux ($j_r \ll j_z$), and the radial solution velocity is assumed to be negligible and much smaller than the axial
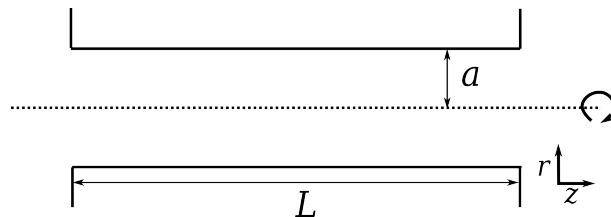

Figure 5.3: Cylindrical pore geometry for deriving fluxes through long pore. The pore has a radius of a and a length of L. The dashed line indicates the axis of symmetry.

solution velocity ($0 \approx u_r \ll u_z$). These assumptions are expected to be accurate for $a \ll L$. Then equation 5.3 can be solved for the solute flux, giving

$$j_r \approx -D\frac{\partial c}{\partial r} - \frac{Dc}{k_B T}\frac{\partial U}{\partial r} \approx 0, \tag{5.13}$$

where the fluid–surface potential U is assumed to depend only on the radial coordinate r. Integrating this equation with respect to r, the solute concentration is

$$c = c_s(z)e^{-U/k_B T}, \tag{5.14}$$

where $c_s(z)$ is the solute concentration when $U = 0$.

If it is assumed that the Péclet number is much less than 1 then the solute flux density is

$$j_z = -D(\nabla c_s)e^{-U/k_B T}. \tag{5.15}$$

Integrating equation 5.15 over the pore cross-section then gives the solute flux as

$$J_P = 2\pi \int_0^a dr\, rj_z, \tag{5.16}$$

where the subscript z refers to the z component of the flux. Substituting equation 5.15 into equation 5.16 gives

$$J_P = -2\pi D\nabla c_s \int_0^a dr\, re^{-U/k_B T}. \tag{5.17}$$

Using $e^{-U/k_B T} = c(r,z)/c_s(z)$ this can be re-written as

$$J_P = -2\pi D \int_0^a dr\, rc(r,z)\frac{d(\ln c_s(z))}{dz}. \tag{5.18}$$

To derive simple scaling laws for the fluxes in terms of the pore radius and solute–wall interaction range the solute excess/depletion at the membrane surface was approximated by a step function in the potential,

$$e^{-U/k_B T} = \begin{cases} 1, & 0 \leq r < a-d \\ \alpha, & a-d \leq r \leq a \end{cases}, \tag{5.19}$$

where d is the length scale of interaction of the potential acting on the solute by the membrane surface, and α characterises the solute excess close to the membrane surface. Using equation 5.19 the solute flux can be written in terms of α and d as

$$J_{P,step} = -\pi D\frac{dc_s}{dz}\left[(a-d)^2 + \alpha d(2a-d)\right]. \tag{5.20}$$

As assumed earlier, $u_r \approx 0$, which when substituted into equation 5.1 gives

$$-\frac{\partial p}{\partial r} - c\frac{\partial U}{\partial r} \approx 0. \tag{5.21}$$

Re-arranging equation 5.13 gives

$$k_B T\frac{\partial c}{\partial r} = -c\frac{\partial U}{\partial r}. \tag{5.22}$$

Then, substituting equation 5.22 into equation 5.21, and integrating gives

$$p = p_\infty + k_B Tc_s(z)\left(e^{-U/k_B T} - 1\right). \tag{5.23}$$

Taking the derivative of equation 5.23 with respect to z, substituting it into the z component of equation 5.1, and integrating twice (assuming fluid velocity at pore surface vanishes) gives

$$u_z(r) = \frac{-k_B T}{\mu} \frac{dc_s}{dz} \int_r^a \frac{dr'}{r'} \int_0^{r'} dr'' \, r'' \left(e^{-U(r'')/k_B T} - 1 \right),$$ (5.24)

where $u_z(r)$ is the axial component of the solution velocity field. Integrating $u_z(r)$ over the pore cross-section gives the solution flux as

$$Q_P = \frac{-\pi}{2\mu} k_B T \frac{d \ln c_s}{dz} \int_0^a dr \, r(a^2 - r^2) \left[c(r,z) - c_s(z) \right].$$ (5.25)

Finally, using the α and d variables, to determine the diffusio-osmotic flux for a step function potential

$$Q_{p,step} = \frac{-\pi}{2\mu} k_B T \frac{dc_s}{dz} (\alpha - 1) \frac{d^2}{4} (2a - d)^2.$$ (5.26)

In the limit that $d \ll a$ equation 5.26 may be written as

$$Q_{p,step} \approx \frac{-\pi a^2}{2\mu} k_B T \frac{dc_s}{dz} (\alpha - 1) d^2.$$ (5.27)

5.4.2 *Fluxes through circular orifice in infinitesimally thin membrane*

The fluxes through a circular orifice in an infinitesimally thin membrane (Figure 5.4) were used to derive equations for the access diffusio-osmotic resistance and the access resistance to the solute flux. The derivation assumes a dilute solution, and a sufficiently small concentration gradient such that the perturbation expansion of the flow variables can be truncated at first order with respect to their equilibrium values. A combination of cylindrical (r, z, θ) and oblate spheroidal (ν, ζ, θ) coordinates (Figure 5.5) were used in the derivation. The coordinate r is the radial distance from the pore surface to the centre of the pore, z is the distance along the pore axis (parallel to the pore), and θ is the angle about the z axis. The coordinates are defined on the intervals $0 \le r \le a$, $-\infty < z < \infty$, and $0 \le \theta \le 2\pi$. The relationship between the cylindrical and oblate spheroidal coordinates is[82,90]

$$z = a\nu\zeta$$ (5.28)

and

$$r = a\sqrt{(1 + \nu^2)(1 - \zeta^2)},$$ (5.29)

where ν and ζ are defined on the intervals $0 \le \nu < \infty$ and $-1 \le \zeta \le 1$, respectively (note these coordinates are different from the oblate spheroidal coordinates used in chapter 3). In this model the solute flux is J, and the solution flux is Q. The concentrations far from the membrane in the positive and negative z directions are c_H and c_L, respectively. The solution pressures far from the membrane on both sides are the same (p_∞).

Let the concentration difference between the two sides of the membrane be $\Delta c = c_H - c_L$, and the average concentration far from the membrane be $c_\infty = (c_H + c_L)/2$. Then the boundary conditions far from the membrane (ie. at infinity) are

$$c \to c_\infty + \tfrac{\Delta c}{2}, \quad \nu \to \infty \quad \text{(in upper reservoir)},$$ (5.30)

$$c \to c_\infty - \tfrac{\Delta c}{2}, \quad \nu \to \infty \quad \text{(in lower reservoir)},$$ (5.31)
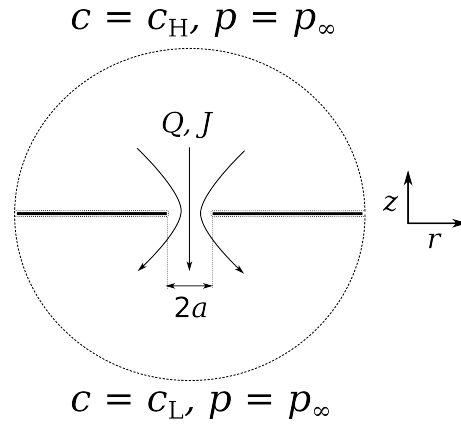
Figure 5.4: Solution flux Q and solute flux J through a circular orifice in an infinitesimally thin membrane. The solute concentrations far from the membrane in the positive and negative z directions are c_H and c_L, respectively, while the solution pressures are p_∞ in both directions. The pore radius is a.
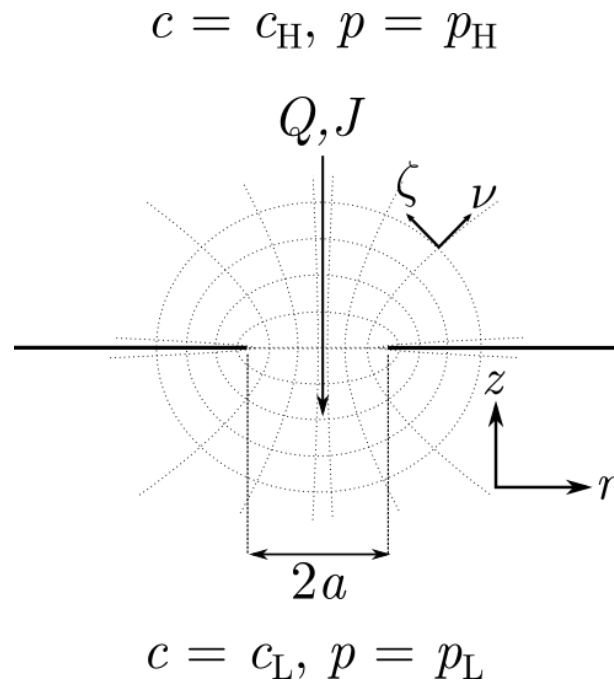
Figure 5.5: Diagram of oblate spheroidal (ν, ζ, θ) coordinates.

and

$$p \to p_\infty \quad \nu \to \infty \quad \text{(in both reservoirs).} \tag{5.32}$$

The solution velocity and solute flux at the membrane surface satisfy the relationships

$$\hat{n} \cdot v = 0 \tag{5.33}$$

and

$$\hat{n} \cdot j = 0, \tag{5.34}$$

respectively, where $\hat{n}$ is the unit vector normal to the membrane surface.

The solute diffusivity is assumed to be related to the solute mobility by the Einstein relation,

$$\lambda = \frac{D}{k_B T}, \tag{5.35}$$

where k_B is Boltzmann's constant, and T is the temperature of the solution. By assuming that the solution velocity field does not greatly affect the solute current (ie. assuming a low Peclét number), and using equation 5.35, equation 5.3 can be re-written as

$$\nabla \cdot \boldsymbol{j} = \nabla \cdot \left(-D\nabla c - \frac{Dc}{k_B T} \nabla U \right) = 0. \tag{5.36}$$

Putting $\boldsymbol{j} = 0$ into this equation the equilibrium solute concentration (ie. in the absence of the concentration difference Δc) can be written as

$$c = c_\infty e^{-U/k_B T}. \tag{5.37}$$

A perturbation expansion of the variables from equilibrium can be used to derive the solute and solvent fluxes for sufficiently small concentration gradients. The expanded variables are

$$p = p_0 + p_1 + \cdots, \tag{5.38}$$

$$c = c_0 + c_1 + \cdots, \tag{5.39}$$

and

$$\boldsymbol{u} = \boldsymbol{u}_0 + \boldsymbol{u}_1 + \cdots, \tag{5.40}$$

where the subscript 0 refers to the respective equilibrium fields, and the subscript 1 represents the first terms in the expansion away from equilibrium.

Truncating the expansion for the solute concentration (equation 5.39) at first order, and using it in the equation for the solute current (equation 5.3) gives

$$\nabla \cdot \boldsymbol{j} = \nabla \cdot \left(-\nabla c_1 - \frac{c_1}{k_B T} \nabla U \right) = 0. \tag{5.41}$$

Assuming that $j_{xi} \ll j_v$,

$$c_1(\nu, \zeta) = c_{1s}(\nu) e^{-U(\nu,\zeta)/k_B T}. \tag{5.42}$$

Assume that the potential is a function of the distance from the membrane surface. For small values of ζ the distance from the membrane surface depends only on ζ. Therefore, if the potential is assumed to be very short ranged compared with the pore radius, then

$$U(\nu, \zeta) = U(\zeta). \tag{5.43}$$

Using equations 5.41, 5.42, and 5.43, the concentration, c_{1s}, where $U = 0$ may be given by the solution to the Laplace equation,

$$\nabla^2 c_{1s} = 0. \tag{5.44}$$

Equation 5.44 is subject to the boundary conditions at infinity,

$$c_{1s} \rightarrow \begin{cases} \frac{\Delta c}{2}, & \nu \rightarrow \infty \quad \text{(in upper reservoir)} \\ -\frac{\Delta c}{2}, & \nu \rightarrow \infty \quad \text{(in upper reservoir)} \\ \hat{\boldsymbol{n}} \cdot \nabla c_{1s} = 0 & \text{(at membrane surface)} \end{cases} \tag{5.45}$$

The solution to equation 5.44 for $0 \leq \nu < \infty$ is, subject to the boundary conditions in equation 5.45,[90]

$$c_{1s}(\nu) = \frac{\Delta c}{2} \left[1 - \frac{2}{\pi} \tan^{-1} \left(\frac{1}{\nu} \right) \right]. \tag{5.46}$$

From equations 5.42 and 5.46,

$$c(\nu,\zeta) = c_s(\nu)e^{-U/k_B T} = \left\{ c_\infty + \frac{\Delta c}{2} \left[1 - \frac{2}{\pi} \tan^{-1}\left(\frac{1}{\nu}\right) \right] \right\} e^{-U/k_B T}, \nu > 0. \tag{5.47}$$

The gradient in c_{1s} is

$$\nabla c_{1s} = \hat{\nu} \left(\frac{\Delta c}{\pi a} \right) \left(\frac{1}{\sqrt{(\nu^2 + \zeta^2)(1 + \nu^2)}} \right), \nu > 0, \tag{5.48}$$

where $\hat{\nu}$ is the unit vector in the ν direction. The solute flux density may then be written as (using equations 5.36 and 5.42)

$$\boldsymbol{j} = -De^{-U/k_B T}\nabla c_{1s}. \tag{5.49}$$

The solute flux across the pore is then given by

$$J_a = \iint_S ds\, \boldsymbol{j} \cdot \hat{\boldsymbol{n}}, \tag{5.50}$$

where $\hat{\boldsymbol{n}}$ is the normal to the orifice, and the integral is over the entire surface area of the orifice. Through using the definitions of the gradient and Laplacian in oblate spheroidal coordinates (see Appendix A), equation 5.50 can be written as

$$J_a = -2aD\Delta c \int_0^1 d\zeta\, e^{-U(\nu,\zeta)/k_B T}. \tag{5.51}$$

At $\nu = 0$, $\zeta^2 = 1 - \left(\frac{r}{a}\right)^2$ so the solute flux in cylindrical coordinates is

$$J_a = -2D\Delta c \int_0^a \frac{dr\, re^{-U/k_B T}}{\sqrt{a^2 - r^2}} = -2D\Delta c \int_0^a \frac{dr\, rc(r, z = 0)}{c_\infty \sqrt{a^2 - r^2}}. \tag{5.52}$$

To derive the solution flux it is assumed that $u_\nu \gg u_\zeta$. Then, taking the ζ component of the Stokes equation (equation 5.1) and using equation 5.47, the solution pressure is

$$p = p_\infty + k_B T c_s(\nu) \left[e^{-U/k_B T} - 1 \right]. \tag{5.53}$$

Taking the derivative of the pressure with respect to ν, and substituting it into the ν component of equation 5.1 gives

$$-\frac{1}{a}\sqrt{\frac{1 + \nu^2}{\nu^2 + \zeta^2}} \frac{\partial p}{\partial \nu} + \mu \nabla^2 u_\nu = 0. \tag{5.54}$$

Due to the symmetry of the system in the θ coordinate, $\frac{\partial u_\nu}{\partial \theta} = 0$. Assuming that $\frac{\partial u_\nu}{\partial \nu} \ll \frac{\partial u_\nu}{\partial \zeta}$, using equation 5.47, assuming that the fluid velocity is zero at the membrane surface, and integrating twice, the fluid velocity at the orifice ($\nu = 0$) is

$$u_\nu(\zeta) = \frac{k_B T \Delta c a}{\mu \pi} \int_0^\zeta \frac{d\zeta'}{(1 - \zeta'^2)} \int_1^{\zeta'} d\zeta''\, \zeta'' f(\zeta''), \tag{5.55}$$

where

$$f(\zeta) = e^{-U(\zeta)/k_B T} - 1. \tag{5.56}$$

The solution flux is then given by

$$Q = \iint_S ds\, \boldsymbol{u} \cdot \hat{\boldsymbol{n}}. \tag{5.57}$$

Using equations 5.55–5.57, the solution flux is

$$Q_a = \frac{-k_B T \Delta c a^3}{\mu} \int_0^1 d\zeta \, \zeta^2 \left(e^{-U/k_B T} - 1 \right). \tag{5.58}$$

In terms of cylindrical coordinates (using equation 5.29) the solution flux through the orifice (at $z = 0$) is

$$Q_a = \frac{-k_B T \Delta c}{\mu} \int_0^a dr \, r \sqrt{a^2 - r^2} \left(e^{-U/k_B T} - 1 \right). \tag{5.59}$$

This can be written in terms of the equilibrium concentration profile as

$$Q_a = \frac{-k_B T \Delta c}{\mu} \int_0^a dr \, r \sqrt{a^2 - r^2} \left(c(r, z = 0) - c_\infty \right) / c_\infty \tag{5.60}$$

Using the additional approximation of a step potential (equation 5.19), equations 5.52 and 5.60 can be written in terms of the variables α and d as

$$J_{a,\text{step}} = -2D\Delta c \left[1 + (\alpha - 1)\sqrt{d(2a - d)} \right] \tag{5.61}$$

and

$$Q_{a,\text{step}} = \frac{-k_B T \Delta c}{\mu} \frac{(\alpha - 1)}{3} \left[d(2a - d)) \right]^{3/2}, \tag{5.62}$$

respectively. Furthermore, in the limit that $d \ll a$ equations 5.61 and 5.62 may be written as

$$J_{a,\text{step}} \approx -2D\Delta c \left[1 + (\alpha - 1)\sqrt{2a} d^{3/2} \right] \tag{5.63}$$

and

$$Q_{a,\text{step}} \approx \frac{-2^{3/2} k_B T}{\mu} a^{3/2} \frac{(\alpha - 1)}{3} d^{3/2}, \tag{5.64}$$

respectively.

5.4.3 *Transport equations for diffusio-osmosis including access resistance*

To derive the transport equations for diffusio-osmosis, it will be assumed that the total diffusio-osmotic resistance R_T and the total resistance to the solute flux $R_{T,s}$ can be separated into pore and access contributions. Let the pore diffusio-osmotic resistance be R_p and the access diffusio-osmotic resistance be R_a. Furthermore, let the pore resistance to the solute flux be $R_{p,s}$ and the access resistance to the solute flux be $R_{a,s}$. Then the total diffusio-osmotic resistance and the total resistance to the solute flux are assumed to be related to the respective pore and access resistances by

$$R_T = R_p + 2R_a \tag{5.65}$$

and

$$R_{T,s} = R_{p,s} + 2R_{a,s}, \tag{5.66}$$

respectively. This assumes that the resistances can be added in series, and that they are separable from each other.

Assuming that the fluxes respond linearly to the applied external forces the pore resistance to the solute flux may be defined in terms of the concentration difference (Δc) divided by the solute flux through a long, cylindrical pore,

$$R_{\mathrm{p,s}} = \frac{-\Delta c}{J_{\mathrm{p}}}. \tag{5.67}$$

Equation 5.16 is defined in terms of the concentration gradient, so it must first be integrated along the pore length, assuming that U has no z dependence. It is then given by

$$R_{\mathrm{p,s}} = \frac{L}{2\pi D} \left[\int_0^a \mathrm{d}r \; r e^{-U(r)/k_{\mathrm{B}}T} \right]^{-1}, \tag{5.68}$$

or in terms of the solute concentration,

$$R_{\mathrm{p,s}} = \frac{L}{2\pi D} \left[\int_0^a \mathrm{d}r \; r \frac{c(r,z)}{c_{\mathrm{s}}(z)} \right]^{-1}. \tag{5.69}$$

In terms of the step-function potential (using equation 5.20),

$$R_{\mathrm{p,s,step}} = \frac{L}{\pi D} \left[\frac{1}{(a-d)^2 + d\alpha(2a-d)} \right]. \tag{5.70}$$

Similarly, the access resistance to solute flux may be defined in terms of half the concentration difference divided by the solute flux through an orifice in an infinitesimally thin membrane,

$$R_{\mathrm{a,s}} = \frac{-\Delta c}{2J_{\mathrm{a}}}. \tag{5.71}$$

This is because there are two pore ends to the infinitesimally thin membrane. Using the full theory

$$R_{\mathrm{a,s}} = \frac{1}{4D} \left[\int_0^a \frac{\mathrm{d}r \; r e^{-U(r)/k_{\mathrm{B}}T}}{\sqrt{a^2 - r^2}} \right]^{-1}, \tag{5.72}$$

or using equation 5.37 and assuming z independence of $c(r,z)/c_{\mathrm{s}}(z)$ (see Appendix A),

$$R_{\mathrm{a,s}} = \frac{1}{4D} \left[\int_0^a \frac{\mathrm{d}r \; r c(r,z)}{c_{\mathrm{s}}(z)\sqrt{a^2 - r^2}} \right]^{-1}. \tag{5.73}$$

For a step-function potential (using equation 5.61),

$$R_{\mathrm{a,s,step}} = \frac{1}{4D} \left[1 + (\alpha - 1)\sqrt{d(2a-d)} \right]^{-1}. \tag{5.74}$$

Applying the same method to the solution flux the pore diffusio-osmotic resistance (using equation 5.25) is

$$R_{\mathrm{p}} = \frac{2\mu L}{\pi k_{\mathrm{B}}T} \left[\int_0^a \mathrm{d}r \; r(a^2 - r^2) \left(e^{-U(r)/k_{\mathrm{B}}T} - 1 \right) \right]^{-1}, \tag{5.75}$$

and in terms of the solute concentration is

$$R_{\mathrm{p}} = \left[\frac{2\mu L}{\pi k_{\mathrm{B}}T} \right] \left[\int_0^a \mathrm{d}r \; r(a^2 - r^2) \left[(c(r,z) - c_{\mathrm{s}}(z)) / c_{\mathrm{s}}(z) \right] \right]^{-1}. \tag{5.76}$$

Then, using equation 5.26 for a step-function potential

$$R_{\text{p,step}} = \frac{8\mu L}{\pi k_{\text{B}} T} \left[\frac{1}{(\alpha - 1) d^2 (d - 2a)^2} \right]. \tag{5.77}$$

If $d \ll a$ then

$$R_{\text{p,step}} \approx \frac{2\mu L}{\pi k_{\text{B}} T (\alpha - 1) a^2 d^2}. \tag{5.78}$$

Similarly, the access diffusio-osmotic resistance is, using equation 5.60,

$$R_{\text{a}} = \frac{\mu}{2k_{\text{B}} T} \left[\int_0^a dr \left(r \sqrt{a^2 - r^2} \left(e^{-U(r)/k_{\text{B}} T} - 1 \right) \right) \right]^{-1}, \tag{5.79}$$

which in terms of the solute concentration profile is

$$R_{\text{a}} = \frac{\mu}{2k_{\text{B}} T} \left[\int_0^a dr \left(r \sqrt{a^2 - r^2} \left[(c(r, z) - c_{\text{s}}(z)) / c_{\text{s}}(z) \right] \right) \right]^{-1}. \tag{5.80}$$

Then, using a step-function potential (equation 5.62),

$$R_{\text{a,step}} = \frac{3\mu}{2k_{\text{B}} T} \left[\frac{1}{(\alpha - 1) \left[(2a - d) d \right]^{3/2}} \right]. \tag{5.81}$$

In the regime where $d \ll a$,

$$R_{\text{a,step}} \approx \frac{3\mu}{2^{5/2} k_{\text{B}} T (\alpha - 1) a^{3/2} d^{3/2}}. \tag{5.82}$$

The fluxes may then be given in terms of the pore and access resistances as

$$J = \frac{-\Delta c}{R_{\text{p,s}} + 2R_{\text{a,s}}} \tag{5.83}$$

and

$$Q = \frac{-\Delta c}{R_{\text{p}} + 2R_{\text{a}}}. \tag{5.84}$$

The approximate scaling of the different types of pore and access resistances in terms of the pore radius and the range of the solute–wall potential can be derived from the simplified equations that use a step-function potential. From equation 5.70 the approximate scaling of the pore resistance to the solute flux in terms of a and d is $R_{\text{p,s}} \sim \left[(a - d)^2 + d\alpha(2a - d) \right]^{-1}$. From equation 5.74 the approximate scaling of the access resistance to the solute flux is $R_{\text{a,s}} \sim \left[1 + (\alpha - 1) \sqrt{d(2a - d)} \right]^{-1}$. In terms of the pore diffusio-osmotic resistance the scaling is $R_{\text{p}} \sim \left[d^2 (d - 2a)^2 \right]^{-1}$, which when $d \ll a$ is simplified to $R_{\text{p}} \sim a^{-2} d^{-2}$. Lastly, for the access diffusio-osmotic resistance, $R_{\text{a}} \sim \left[(2a - d) d \right]^{-3/2}$, which when $d \ll a$ simplifies to $R_{\text{a}} \sim a^{-3/2} d^{-3/2}$.

5.5   RESULTS AND DISCUSSION

5.5.1   *Finite element method results*

To validate the theory, FEM simulations were carried out through pores with different radii and solute–wall interaction parameters (ϵ_{sw} and σ_{sw}). To check the accuracy of the FEM simulations, both concentration-gradient-driven and pressure-driven FEM simulations were

carried out. The Onsager reciprocity relations were used to relate the pressure-driven solute excess flux with the diffusio-osmotic flux. In order for the Onsager reciprocity relations to be correct, the fluxes must be in the linear response regime. Figure 5.6 shows the total solution flux and total solute flux through a very thin orifice versus the applied concentration difference. As linear response holds for a very thin orifice, where deviations might be expected to be more significant than for finite-length pores due to the larger fluxes, it is expected to hold for pores of any length for these set of parameters. The access diffusio-osmotic resistance calculated using both the concentration-gradient-driven and pressure-driven simulations were found to be exactly the same. As both simulations gave the same results, only the concentration-gradient-driven FEM simulation results are shown in this thesis.

To compare with the theory the pore diffusio-osmotic resistance was calculated from the FEM simulations for finite length pores by subtracting twice the access diffusio-osmotic resistance from the total diffusio-osmotic resistance. The result was then divided by the pore length and compared with equation 5.75. Figure 5.7 shows a comparison of the theory with the FEM simulations for different pore radii and solute–wall interaction strengths. The theory shows quantitative agreement with the FEM results and the same scaling from the simplified theory (equation 5.78) holds when $d \ll a$. The length scale of interaction of the potential d is directly proportional to the parameter σ_{sw}. For these set of parameters the scaling from the simplified theory holds for pore radii larger than around 5σ.

Figure 5.8 shows the access diffusio-osmotic resistance versus the pore radius. The theory approximately shows the correct scaling of the access diffusio-osmotic resistance with pore radius but there is a quantitative difference. To reconcile this disagreement further work on the theory is required. Nevertheless, the approximate scaling from the simplified theory (equation 5.82) holds in the limit that $d \ll a$ (pore radii larger than around 5σ).

By comparing the approximate scaling of the access diffusio-osmotic resistance from the simplified theory with the approximate scaling of the pore diffusio-osmotic resistance, it can be calculated when the access diffusio-osmotic resistance becomes important. Immediately from comparing Figure 5.7 with Figure 5.8 it can be ascertained that the pore and access diffusio-osmotic resistances are on the same order for most of the pore radii considered when the pore length is σ. For the set of parameters considered here this equates to pore aspect ratios (length to diameter ratios) of $\approx 1/4$, which could be easily realised using available materials such as porous graphene.[91]

Figures 5.9 and 5.10 show the pore diffusio-osmotic resistance per unit length and the access diffusio-osmotic resistance versus σ_{sw}, respectively. The theory again agrees quantitatively with the FEM results for the pore diffusio-osmotic resistance, including the approx-
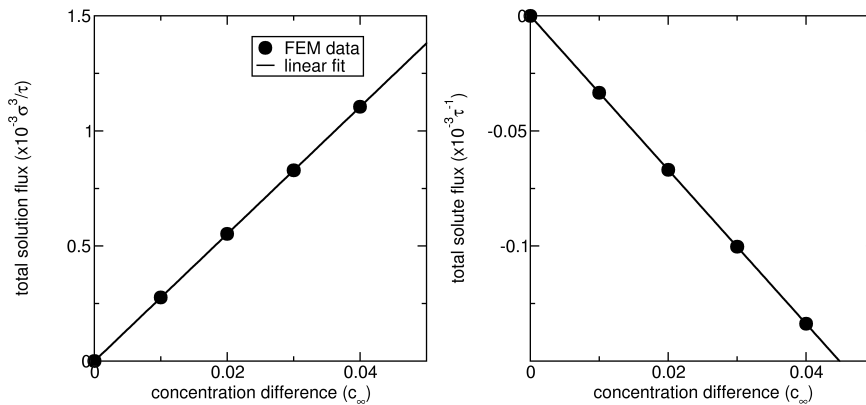

Figure 5.6: Total solution flux (left) and total solute flux (right) versus applied concentration difference. The pore length was 0.2σ, the pore radius was 10.13σ, the solute concentration was $2.85 \times 10^{-3}\sigma^{-3}$, and the solute–wall interaction parameters were $(\epsilon_{sw}, \sigma_{sw}) = (-2.84\epsilon, 0.92\sigma)$.
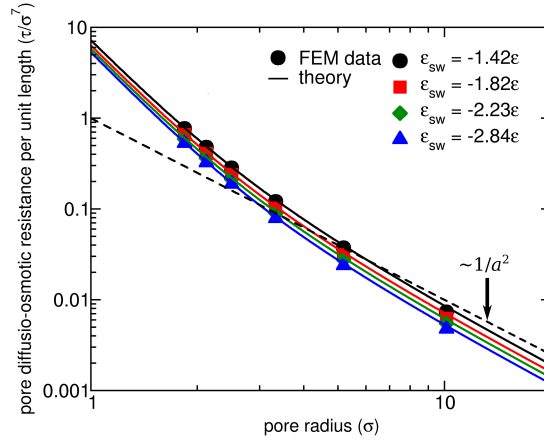
Figure 5.7: Pore diffusio-osmotic resistance per unit length versus pore radius for different solute–wall interaction strengths. The points are from the FEM simulations, the solid lines are predictions using equation 5.75, while the dashed line shows the approximate scaling from the simplified theory (equation 5.78) in the limit that $d \ll a$. The pore length used in the FEM simulations was 30.4σ, while the solute–wall interaction length scale parameter was 0.92σ.
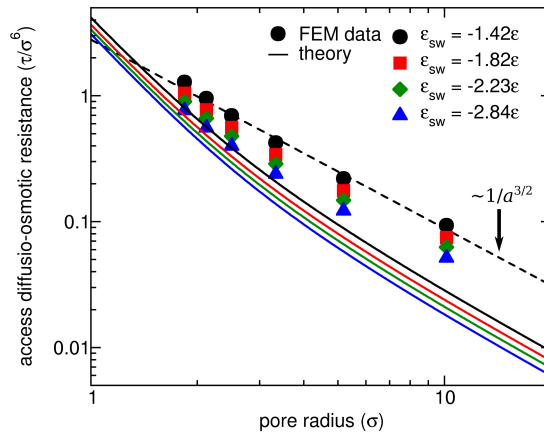

Figure 5.8: Access diffusio-osmotic resistance versus pore radius for different solute–wall interaction strengths. The points are from the FEM simulations, the solid lines are predictions using equation 5.79, while the dashed line shows the approximate scaling from the simplified theory in the limit that $d \ll a$ (equation 5.82). The pore length used in the FEM simulations was 0.2σ, while the solute–wall interaction length scale parameter was 0.92σ.

imate scaling in the limit of $d \ll a$. For the access diffusio-osmotic resistance, the approximate scaling from the simplified theory in the limit of $d \ll a$ holds for solute–wall interaction length scales smaller than around 0.72σ. However, a similar disagreement between the theory and the simulation results is seen as with the results of the access diffusio-osmotic resistance versus pore radius. There is a quantitative disagreement between the theory and the simulation results. Also, different scaling is observed when σ_{sw} is larger than around 0.72σ.

The simplified theory shows that the diffusio-osmotic resistances have the same scaling with the solute–wall interaction length scale as they do with the pore radius for $d \ll a$. Therefore, increasing the solute–wall interaction length scale by a factor of 10 is equivalent to increasing the pore radius ten-fold in terms of its effect on the diffusio-osmotic resistance. A comparison can be drawn to diffusio-osmosis of an electrolyte. For weakly charged surfaces the length scale of interaction of the potential is approximately half the Debye length ($d \approx \lambda_D/2$),[23] which depends on the salt concentration. The salt concentration also affects the
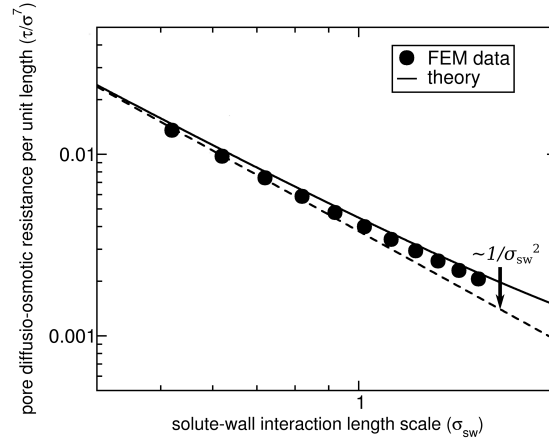
Figure 5.9: Pore diffusio-osmotic resistance per unit length versus solute–wall interaction length parameter σ_{sw}. The points are from the FEM simulations, the solid lines are predictions using equation 5.75, while the dashed line shows the approximate scaling from the simplified theory in the limit that $d \ll a$ (equation 5.78). The pore radius was 10.13σ, the solute–wall interaction strength was -2.84ϵ, and the pore length used in the FEM simulations was 30.4σ.
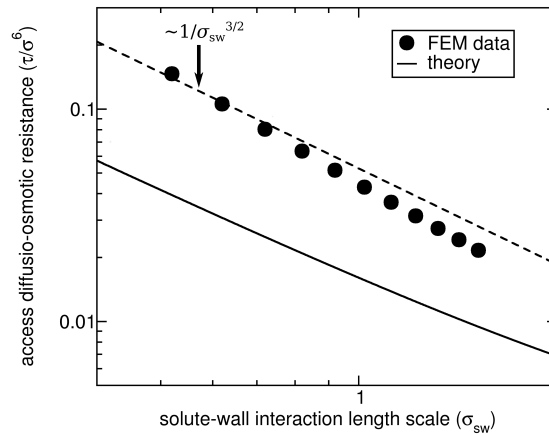

Figure 5.10: Access diffusio-osmotic resistance versus solute–wall interaction length parameter σ_{sw}. The points are from the FEM simulations, the solid lines are predictions using equation 5.79, while the dashed line shows the approximate scaling from the simplified theory in the limit that $d \ll a$ (equation 5.82). The pore radius was 10.13σ, the pore length was 0.2σ, the solute–wall interaction strength was -2.84ϵ.

fluid–surface interaction strength (α) due to the dependence of the surface potential on the salt concentration. For a weak potential, the $(\alpha - 1)$ term in equations 5.78 and 5.82 is proportional to the Debye length. The Debye length is proportional to $1/\sqrt{c_\infty}$, which means that the scaling of the access diffusio-osmotic resistance with salt concentration is $R_a \sim c_\infty^{5/4}$, while the scaling of the pore diffusio-osmotic resistance is $R_p \sim c_\infty^{3/2}$. In particular, this shows that the access diffusio-osmotic resistance scales more weakly with salt concentration than the pore diffusio-osmotic resistance. So by decreasing the salt concentration, the access diffusio-osmotic resistance decreases more slowly than the pore diffusio-osmotic resistance.

In this study concentration-gradient-driven FEM simulations were used to validate the theory for the pore and access diffusio-osmotic resistances. It was found that the theory for the pore diffusio-osmotic resistance agrees quantitatively with the FEM results, while the theory for the access diffusio-osmotic resistance shows a quantitative disagreement with the FEM results but approximately the correct scaling, particularly when the pore radius

is small compared with the solute–wall interaction range. To fix the disagreement between the theory and the FEM simulation results, further work on the theory is required.

The main results shown here are that the approximate scaling relations from the simplified theory in the limit that $d \ll a$ agrees with the FEM simulations and shows that the access diffusio-osmotic resistance can be on the same order as the pore diffusio-osmotic resistance for experimentally realisable conditions. Furthermore, increasing the interaction length scale of the potential effectively increases the pore radius in terms of its effect on the diffusio-osmotic resistance. For an electrolyte, it was shown that the access diffusio-osmotic resistance has a weaker scaling with salt concentration than does the pore diffusio-osmotic resistance. Therefore, the access diffusio-osmotic resistance can become the main contributor to the total diffusio-osmotic resistance at low salt concentrations.

5.5.2   *Molecular dynamics results*

One of the challenges in using MD to simulate solution fluxes through pores connected to reservoirs is the possible effect of reservoir sizes on the results. In this study the reservoir volume was chosen to be around $2.5 \times 10^5 \sigma^3$. For this reservoir size for the solution flux was found to be converged as a function of reservoir size (Figure 5.11).

Figure 5.12 shows the concentration-gradient-driven solution velocity profile inside the widest simulated pore for both the largest and smallest pore lengths. The first thing that can be seen is a plug-like flow for the long pore and a slightly parabolic flow inside the short pore. This parabolic velocity profile inside the short pore is not unlike the one found for MD simulations of planar Poiseuille flow of polymers through slit nanopores.[92] In particular, in ref. 92 a weak parabolic flow was observed towards the middle of a 14σ wide nanoslit. However, the flow-driving mechanism and pore geometry are different in ref. 92 to what is studied here. The parabolic flow for the short pore in Figure 5.12 is due to end effects instead of a variation in fluid density across the pore, as in ref. 92. This is clear when comparing with the velocity profile inside the long pore, which does not have any statistically significant parabolic flow in the middle of the pore. The flow profile of the short pore is similar to the one observed in ref. 17 for electro-osmosis across a thin orifice. This was a result of an induced pressure difference across the thin orifice. It is likely that similar end effects are occurring in Figure 5.12 for the short pore. This confirms that the MD simulations are capturing end effects.

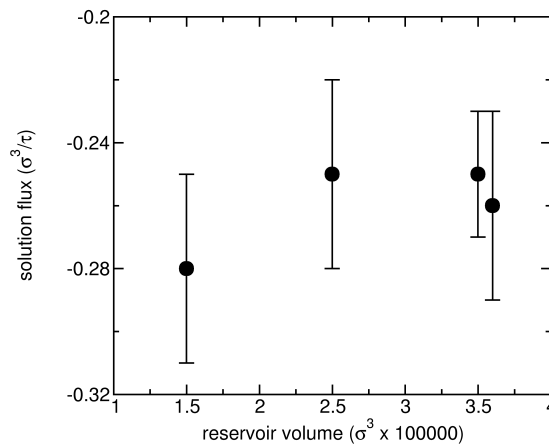Figure 5.11: Total solution flux versus reservoir volume for MD simulations. The pore radius was 9.43σ, the pore length was 30.4σ, the solute concentration was $1.64 \times 10^{-1}\sigma^{-3}$, and the solute concentration ratio was $c_H/c_L = 50$.
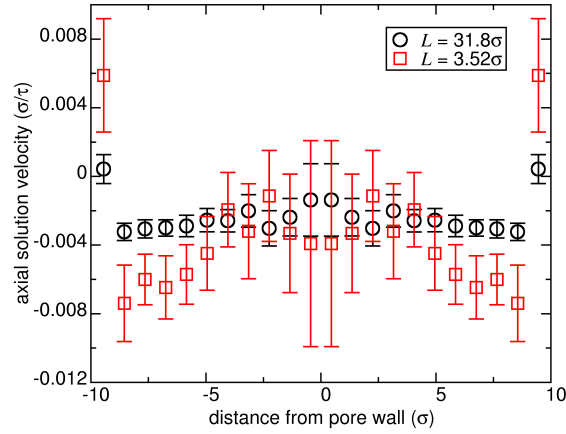
Figure 5.12: Solution velocity versus distance from pore centre for two different pore lengths. The pore radius was 9.43σ, the solute concentration was $1.64 \times 10^{-1}\sigma^{-3}$, and the solute concentration ratio was $c_{H}/c_{L} = 50$.
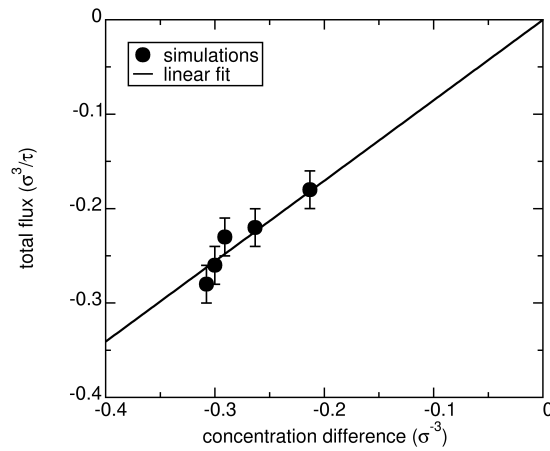

Figure 5.13: Total solution flux versus applied concentration difference from MD simulations. The points are from the MD simulations, while the line is a linear fit. The pore radius was 4.48σ, the pore length was 31.8σ, and the solute concentration was $1.64 \times 10^{-1}\sigma^{-3}$.

To compare the diffusio-osmotic transport theory with the MD results it should first be verified that linear response holds in these simulations. Figure 5.13 shows the total solution flux versus the applied concentration difference for a pore with a radius of 4.48σ, a pore length of 31.8σ, and a solute concentration of $1.64 \times 10^{-1}\sigma^{-3}$. The solute flux could not be plotted versus the applied concentration difference due to the standard deviation being comparable with the mean at the lower concentration differences. In order to reduce the standard deviation the simulation time would need to be very long, which was found to be computationally infeasible. As linear response holds at a solute concentration of $1.64 \times 10^{-1}\sigma^{-3}$ it is also expected to hold for the lower solute concentration simulations. Although linear response holds, the low Péclet number assumption does not hold as the total and diffusive solute fluxes are not comparable (Figure 5.14). As a result of this only the diffusive solute fluxes were used in calculating the resistances to the solute flux.

The pore resistance to the solute flux per unit length was calculated by dividing the total resistance to the solute flux minus twice the access resistance to the solute flux by the pore length. Figure 5.15 shows the pore resistance to the solute flux per unit length from the MD simulations and from the theory. The theory shows quantitative agreement with the MD results for a solute concentration of $8.24 \times 10^{-2}\sigma^{-3}$. For the MD results carried out at a solute concentration of $1.64 \times 10^{-1}\sigma^{-3}$ the pore resistance to the solute flux per unit length is overestimated by the theory. However, at such high solute molar fractions, where
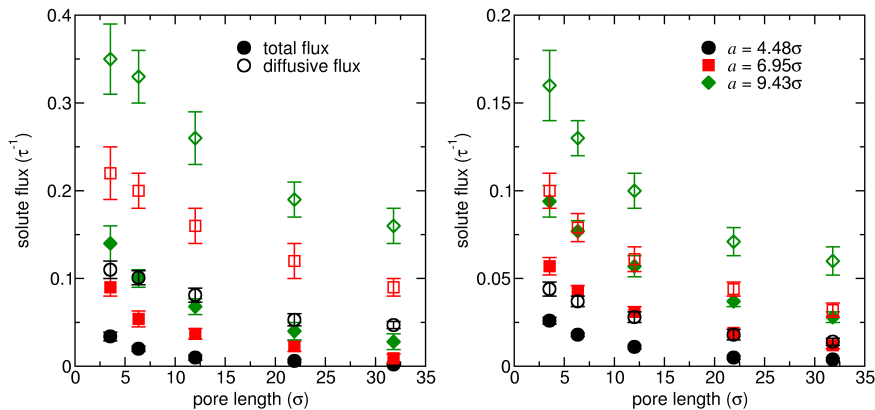
Figure 5.14: Total and diffusive solute fluxes versus pore length for different pore radii using solute concentrations of $1.64 \times 10^{-1}\sigma^{-3}$ (left) and $8.24 \times 10^{-2}\sigma^{-3}$ (right). The points are from the MD simulations (dotted lines are a guide to the eye). The closed symbols are the total solute fluxes, while the open symbols are the diffusive solute fluxes. The pore length was 31.8σ and the concentration ratio was $c_\mathrm{H}/c_\mathrm{L} = 50$.
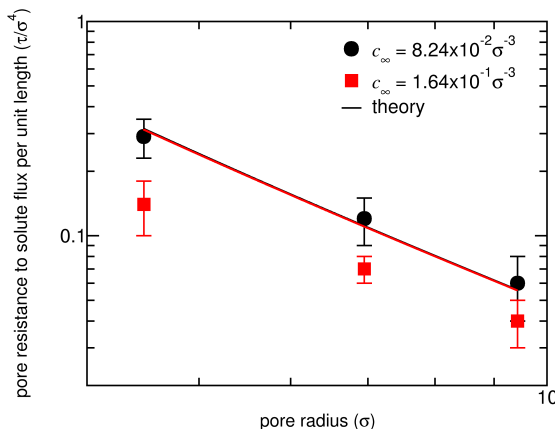

Figure 5.15: Pore resistance to the solute flux per unit length versus pore radius. The theory lines, which are overlapping in the figure, were calculated from the MD concentration profiles using equation 5.69. The solute fluxes used to calculate the resistances to the solute flux were calculated using the diffusive solute fluxes only. The pore length was 31.8σ and the applied concentration ratio was $c_\mathrm{H}/c_\mathrm{L} = 50$.

the solute makes up 20% of the total number of solution particles, the solution may not be ideal, which is one of the assumptions made in the continuum theory. The agreement with the theory at lower solute concentrations also suggests that the discrepancy may be due to non-ideal effects. Despite the discrepancy the MD results show the same scaling as is predicted by the theory.

Figure 5.16 shows the access resistance to the solute flux versus pore radius. The theory only slightly overestimates the MD results but shows the same scaling. In this case the access resistance for both solute concentrations are overlapping, which contrasts with the results of the pore resistance to the solute flux per unit length. Therefore, the possible non-ideal effects mentioned in regards to the pore resistance to the solute flux do not have an effect on the access resistance to the solute flux.

Figure 5.17 shows the pore diffusio-osmotic resistance per unit length versus pore radius. The theory does not agree quantitatively with the MD results, which is in contrast with the comparison between the FEM results and the theory in the previous section. One potential issue is that the theory curves were calculated using a spline fit to the MD concentration profiles. The spline fit was calculated using only the concentration profile for the largest
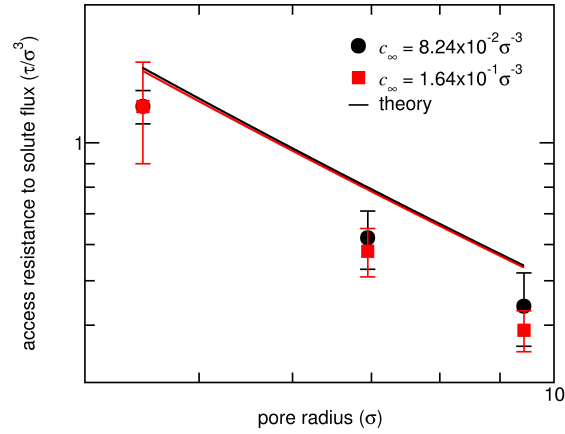
Figure 5.16: Access resistance to the solute flux versus pore radius. The theory lines, which are overlapping in the figure, were calculated from the MD concentration profiles using equation 5.73. The solute fluxes used to calculate the resistances to the solute flux were calculated using the diffusive solute fluxes only. The applied concentration ratio was $c_H/c_L = 50$.
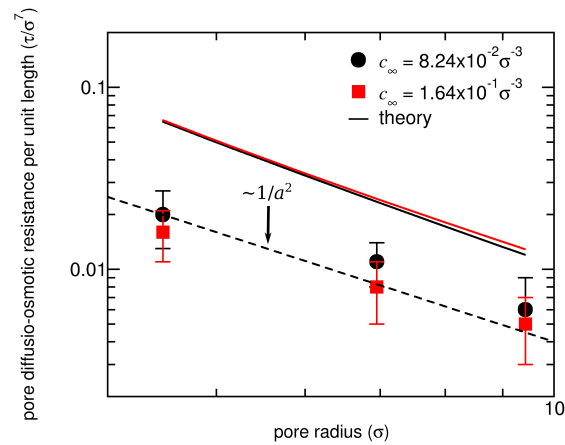

Figure 5.17: Pore diffusio-osmotic resistance per unit length versus pore radius for MD simulations. The theory lines, which are overlapping in the figure, are calculated from the MD concentration profiles at two different solute concentrations using equation 5.76. The pore length was 31.8σ and the applied concentration ratio was $c_H/c_L = 50$.

pore radius as an input, while the smaller pore radii were interpolated from the spline fit. This is a potential source of error. However, the MD simulations also show a significant degree of layering close to the pore wall, which is shown by the solute concentration profile (Figure 5.18). It is likely that non-continuum effects due to molecular layering close to the pore surfaces is causing this disagreement with the theory. Nevertheless the results agree well with the approximate scaling given by the simplified theory in the limit that $d \ll a$. As demonstrated in the last section these approximate scaling relations can be used to understand where the access diffusio-osmotic resistance becomes a significant contributor to the total diffusio-osmotic resistance.

Figure 5.19 shows the access diffusio-osmotic resistance versus pore radius from the MD simulations. The theory does not agree quantitatively with the MD results but the approximate scaling from the simplified theory holds in the limit that $d \ll a$. The quantitative disagreement is more severe than that between the FEM results and the theory discussed in the previous section. The MD results are a whole order of magnitude from the theory, while the FEM results in the previous section are mostly within the same order of magni-
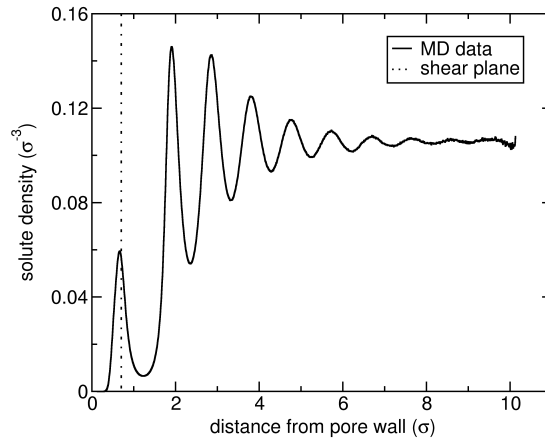
Figure 5.18: Solute density versus distance from pore wall for MD simulations. The pore length was 31.8σ, the pore radius was 9.43σ, and the concentration ratio was $c_H/c_L = 50$.
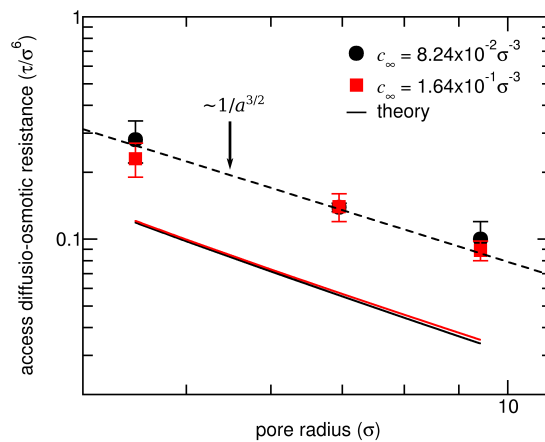

Figure 5.19: Access diffusio-osmotic resistance versus pore radius for MD and theory. The applied concentration ratio was $c_H/c_L = 50$. The theory lines, which are overlapping in the figure, are calculated from the MD concentration profiles at two different solute concentrations using equation 5.80.

tude. This larger disagreement is likely due to the same non-continuum effects that cause the discrepancy between the pore diffusio-osmotic resistance and the theory.

The main result shown in this section is that the MD simulations show the same scaling behaviour predicted by the theory, but there is quantitative disagreement, likely due to the inaccuracy of the continuum assumption. It is noted that there is also a quantitative disagreement between the theory and the FEM simulation results for the access diffusio-osmotic resistance shown in the last section. However, there was no disagreement between the pore diffusio-osmotic resistance from the FEM results and the theory. Furthermore, the theory is within an order of magnitude of the access difffusio-osmotic resistance from the FEM simulations whereas there is more than an order of magnitude difference between the theory and the access diffusio-osmotic resistance from the MD simulations. Therefore, the quantitative disagreement between the MD results and the theory is likely due to non-continuum effects and not for the same reasons as the disagreement between the FEM simulations and the theory.

5.6   CONCLUSION

A complete analytical theory for diffusio-osmotic transport including entrance effects was presented. The theory uses the solution and solute fluxes through a long cylindrical pore

with no ends with the same length as the pore in the membrane to calculate the pore resistance, and the fluxes through a circular orifice in an infinitesimally thin membrane to calculate the access resistance. It assumes that the solution is dilute and that it can be described using continuum theory. Simple scaling laws of the pore and access diffusio-osmotic resistances were derived from the theory by assuming that the solute concentration profile is a step-function, and that the interaction length scale of the solute–wall potential is much smaller than the pore radius. In this regime, the pore diffusio-osmotic resistance scales as $\sim a^{-2}d^{-2}$, where a is the pore radius and d is the range of the fluid–surface interactions, while the access diffusio-osmotic resistance scales as $\sim a^{-3/2}d^{-3/2}$. The significance of this scaling is that the diffusio-osmotic resistances depend similarly on the pore radius and on the length scale of interaction of the potential, and that there is different scaling with these parameters for the pore and access resistances. By considering an electrolyte, the range and strength the potential can be related to the Debye length, which depends on the salt concentration. The diffusio-osmotic resistance decreases with decreasing salt concentration but the access diffusio-osmotic resistance decreases more slowly than does the pore diffusio-osmotic resistance. Therefore, the access diffusio-osmotic resistance can dominate the total diffusio-osmotic resistance for low salt concentrations.

When the theory was compared with FEM simulations of concentration-gradient-driven flow, the theory showed quantitative agreement for the pore diffusio-osmotic resistance and approximately the same qualitative scaling for the access diffusio-osmotic resistance. There was a quantitative difference between the access diffusio-osmotic resistance from the FEM simulations and from the theory, and a difference in scaling when the solute–wall potential interaction length scale was not small compared with the pore radius. Further work on the theory is required in order to fix this discrepancy. When the theory was compared with the MD simulations the same scaling was observed as for the FEM results and the theory, although there was quantitative disagreement between the pore diffusio-osmotic resistance and the theory, and an even larger discrepancy between the theory and the access diffusio-osmotic resistance compared with the FEM results. This disagreement is likely due to non-continuum effects. The models used in the FEM simulations and the MD simulations are quite different. In the FEM simulations the fluid is treated as a continuum and the solute interacts with the solid walls using a simple function of the distance from the solid walls. The total solution flow is calculated by integrating the Stokes equations with a body force that depends on the solute–wall interaction and on the solute concentration gradient. On the other hand, in the MD simulations the fluid is treated as explicit particles. The force on each particle is the force due to all other particles in the system, within a pre-defined cut-off distance. The solute–wall potential develops due to different interactions between solute particles, wall particles, and solvent particles. The flow is calculated by measuring time-averaged particle velocities within a specified region (the pore). When taking into account these differences it is significant that the MD results still agree qualitatively with the theory.

CONCLUSION

In this thesis, the entrance effects on concentration-gradient-driven flows were studied using computation and theory. The phenomena that were investigated have very general applications due to their presence in many different systems of interest such as desalination, filtration, and energy harvesting. In the first study, entrance effects were considered in the context of a porous membrane immersed in an electrolyte solution. The access electrical resistance of a charged pore in both neutral and charged membranes was studied using FEM calculations. These were then compared with previously existing theories, and a new theory that was derived in this thesis. In the second study, the continuum assumption was relaxed using MD simulations. A previously existing algorithm was first modified to function at high solute concentrations, which was subsequently used to study non-continuum and non-ideal effects on the access diffusio-omsotic resistance in the third study. The results of the MD simulations were compared with a new theory of access diffusio-osmotic resistance developed in this thesis, which was first verified by comparing with FEM simulations.

In order to calculate the access electrical resistance of pores immersed in electrolyte solutions, different methods were investigated. These were the slip method, the length method, and the potential drop method. It was found that the potential drop method was the simplest and most accurate method. Using this method the access electrical resistance was shown to agree with the equation by Hall under most conditions when the pore was charged but the outer-membrane wall was neutral. However, for a charged pore inserted into a charged membrane the results showed completely different scaling with surface charge density, salt concentration, and pore radius than is given by the Hall equation. The scaling was found to follow an existing equation derived by Lee et al.,[7] but with a modified numerical pre-factor. However, this pre-factor was found to depend on the pore radius. In order to address this a new theory was developed that considered the access electrical resistance to be half the total electrical resistance of a circular orifice in an infinitesimally thin membrane. The theory was compared with finite element method (FEM) calculations carried out under conditions for which it was expected to work, and excellent agreement with the theory was observed. In particular, the new theory was able to explain to some extent the radius-dependence of the numerical pre-factor used in the equation by Lee et al.

For the MD simulations an algorithm, called the non-periodic energy step method,[8] was used to simulate a concentration-gradient-driven flow. In the original algorithm forces are applied to solute particles in thin regions at the ends of the simulation cell in order to maintain a target concentration ratio. However, this was found to require a modification at high solute concentrations, which had not previously been considered. In the modified algorithm an external force was applied to the solvent particles such that the pressure difference across the reservoirs on either side of the pore converge to zero. The modified algorithm was verified by comparing it with an existing theory for concentration-gradient-driven flow.[20]

The modified algorithm was then used to simulate diffusio-osmotic flows across pores of different lengths in order to calculate the access diffusio-osmotic resistance from the total diffusio-osmotic resistance in the limit of zero pore length. New equations for diffusio-osmosis were derived that take into account the access diffusio-osmotic resistance. The new theory considers the total diffusio-osmotic resistance to be the diffusio-osmotic resistance of a long cylindrical pore with no ends added in series with the diffusio-osmotic resistance of a circular orifice in an infinitesimally thin membrane. The assumptions made in deriving the theory included continuum theory and a dilute solution. This theory was first verified by comparing it with FEM calculations and showed quantitative agreement for the pore

diffusio-osmotic resistance, and approximately the correct qualitative scaling for the access diffusio-osmotic resistance. The theory was then compared with MD simulations carried out at two different solute concentrations. The theory showed a significant quantitative disagreement with the MD results, likely due to non-continuum effects. Nevertheless, the same qualitative scaling, as given by the simplified theory (using a step-function solute–wall potential), was observed for the MD results.

In this thesis two new theories were derived, one for the access electrical resistance, and one for the access diffusio-osmotic resistance. In both cases it was shown that the access resistance is separable from the total resistance, and that the access resistance can become a significant fraction of the total resistance for low-aspect-ratio pores. Low-aspect-ratio pores exist in real porous membranes such as graphene and hexagonal boron nitride, which may be useful for harvesting energy from salinity gradients.[93] Therefore, understanding how the access resistance impacts solution transport on a fundamental level may have a great impact on improving renewable energy.

APPENDIX

A.1 DEFINITIONS OF GRADIENT AND LAPLACIAN IN OBLATE SPHEROIDAL COORDINATES

To calculate the gradient in oblate spheroidal coordinates the general gradient in an orthogonal curvilinear coordinate system was used,

$$\nabla = \frac{\hat{i}_1}{h_1}\frac{\partial}{\partial q_1} + \frac{\hat{i}_1}{h_2}\frac{\partial}{\partial q_2} + \frac{\hat{i}_1}{h_3}\frac{\partial}{\partial q_3}, \tag{A.1}$$

where $\hat{i}_1$, $\hat{i}_2$, and $\hat{i}_3$ are the Cartesian unit vectors, q_1, q_2, and q_3 are the orthogonal curvilinear coordinates, and h_1, h_2, and h_3 are their respective Lamé coefficients. Similarly, for the Laplacian,

$$\nabla^2 = \frac{1}{h_1 h_2 h_3}\left[\frac{\partial}{\partial q_1}\left(\frac{h_2 h_3}{h_1}\frac{\partial}{\partial q_1}\right) + \frac{\partial}{\partial q_2}\left(\frac{h_3 h_1}{h_2}\frac{\partial}{\partial q_2}\right) + \frac{\partial}{\partial q_3}\left(\frac{h_1 h_2}{h_3}\frac{\partial}{\partial q_3}\right)\right]. \tag{A.2}$$

Considering oblate spheroidal coordinates with $q_1 = \nu$, $q_2 = \zeta$, $q_3 = \theta$, $h_1 = a\sqrt{(\nu^2 + \zeta^2)/(1 + \nu^2)}$, $h_2 = a\sqrt{(\nu^2 + \zeta^2)/(1 - \zeta^2)}$, and $h_3 = a\sqrt{(1 + \nu^2)(1 - \zeta^2)}$ (a is the pore radius), the gradient in oblate spheroidal coordinates is

$$\nabla = \frac{\hat{\nu}}{a\sqrt{\frac{\nu^2 + \zeta^2}{1 + \nu^2}}}\frac{\partial}{\partial \nu} + \frac{\hat{\zeta}}{a\sqrt{\frac{\nu^2 + \zeta^2}{1 - \zeta^2}}}\frac{\partial}{\partial \zeta} + \frac{\hat{\theta}}{a\sqrt{(1 + \nu^2)(1 - \zeta^2)}}\frac{\partial}{\partial \theta}, \tag{A.3}$$

where $\hat{\nu}$, $\hat{\zeta}$, and $\hat{\theta}$ are the oblate spheroidal unit vectors. Similarly, the Laplacian in oblate spheroidal coordinates is

$$\nabla^2 = \frac{1}{a(\nu^2 + \zeta^2)}\left[\frac{\partial}{\partial \nu}(1 + \nu^2)\frac{\partial}{\partial \nu} + \frac{\partial}{\partial \zeta}(1 - \zeta^2)\frac{\partial}{\partial \zeta} + \frac{(\nu^2 + \zeta^2)}{(1 + \nu^2)(1 - \zeta^2)}\frac{\partial^2}{\partial \theta^2}\right]. \tag{A.4}$$

A.2 VERIFYING THE Z-INDEPENDENCE OF THE SCALED MD CONCENTRATION PROFILES

In order to derive the theory for diffusio-osmosis it was assumed that the solute concentration profile divided by the average solute concentration is independent of the axial (z) coordinate. Figure A.1 shows the solute concentration profile within a pore that has a radius of 4.48σ and a length of 31.8σ (taking into account shear plane), a solute molar fraction of 0.2, and an applied concentration ratio of $c_H/c_L = 33$. As shown, the solute concentration divided by the "bulk" solute concentration inside the pore is approximately constant with z. The "bulk" solute concentration is the average solute concentration measured far from the pore surface. It is dependent on the z coordinate. The percentage difference between the green curve and the black curve is around 15%.
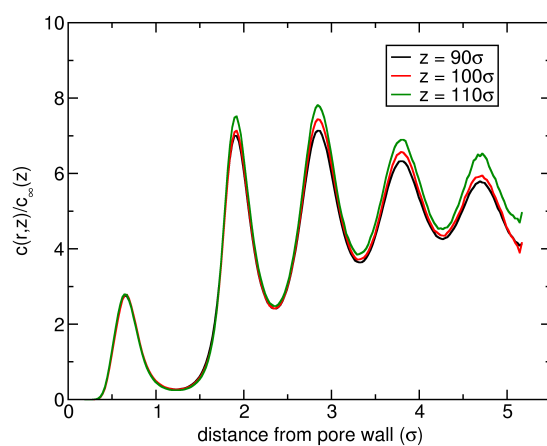
Figure A.1: Solute concentration profile relative to "bulk" solute concentration at different positions along pore. The pore radius is 4.48σ and its length is 31.8σ (taking into account shear plane position). The solute molar fraction was 0.2, while the applied concentration ratio was $c_H/c_L = 33$.

REFERENCES

[1] Rankin, D. J.; Huang, D. M. *Langmuir* **2016**, *32*, 3420–3432.

[2] Hille, B. *Journal of General Physiology* **1967**, *51*, 199–219.

[3] Hall, J. E. *Journal of General Physiology* **1975**, *66*, 531–532.

[4] Peskoff, A.; Bers, D. *Biophysical Journal* **1988**, *53*, 863–875.

[5] Levadny, V.; Aguilella, V. M.; Belaya, M. *Biochimica et Biophysica Acta (BBA) - Biomembranes* **1998**, *1368*, 338 – 342.

[6] Aguilella-Arzo, M.; Aguilella, V.; Eisenberg, R. *European Biophysics Journal* **2005**, *34*, 314–322.

[7] Lee, C.; Joly, L.; Siria, A.; Biance, A.-L.; Fulcrand, R.; Bocquet, L. *Nano Letters* **2012**, *12*, 4037–4044.

[8] Khalili-Araghi, F.; Ziervogel, B.; Gumbart, J. C.; Roux, B. *Journal of General Physiology* **2013**, *142*, 465–475.

[9] Marbach, S.; Bocquet, L. *Physical Review X* **2016**, *6*, 031008.

[10] Elimelech, M.; Phillip, W. A. *Science* **2011**, *333*, 712–717.

[11] Schroeder, T. B. H.; Guha, A.; Lamoureux, A.; VanRenterghem, G.; Sept, D.; Shtein, M.; Yang, J.; Mayer, M. *Nature* **2017**, *552*, 214–218.

[12] Bocquet, L.; Tabeling, P. *Lab on a Chip* **2014**, *14*, 3143–3158.

[13] Charting Our Water Future; Economic Frameworks to Inform Decision-making. 2009.

[14] Bose, B. K. *IEEE Industrial Electronics Magazine* **2010**, *4*, 6–17.

[15] Getpreecharsawas, J.; McGrath, J. L.; Borkholder, D. A. *Nanotechnology* **2015**, *26*, 045704.

[16] Alcaraz, A.; López, M. L.; Queralt-Martín, M.; Aguilella, V. M. *ACS Nano* **2017**, *11*, 10392–10400.

[17] Melnikov, D. V.; Hulings, Z. K.; Gracheva, M. E. *Physical Review E* **2017**, *95*, 063105.

[18] Fair, J. C.; Osterle, J. F. *J. Chem. Phys.* **1971**, *54*, 3307–3316.

[19] Strong, S. E.; Eaves, J. D. *The Journal of Physical Chemistry B* **2017**, *121*, 189–207, PMID: 28009520.

[20] Marbach, S.; Yoshida, H.; Bocquet, L. *The Journal of Chemical Physics* **2017**, *146*, 194701.

[21] Derjaguin, B.; Dukhin, S.; Koptelova, M. *Journal of Colloid and Interface Science* **1972**, *38*, 584–595.

[22] Anderson, J. L.; Lowell, M. E.; Prieve, D. C. *Journal of Fluid Mechanics* **1982**, *117*, 107–121.

[23] Ajdari, A.; Bocquet, L. *Physical Review Letters* **2006**, *96*, 186102.

[24] Mao, M.; Sherwood, J. D.; Ghosal, S. *Journal of Fluid Mechanics* **2014**, *749*, 167–183.

[25] Sherwood, J. D.; Mao, M.; Ghosal, S. *Langmuir* **2014**, *30*, 9261–9272.

[26] Durst, F. *Fluid Mechanics: An Introduction to the Theory of Fluid Flows*; Springer-Verlag, 2008.

[27] Shen, M.; Ye, F.; Liu, R.; Chen, K.; Yang, M.; Ripoll, M. *The Journal of Chemical Physics* **2016**, *145*.

[28] Lee, C.; Cottin-Bizonne, C.; Fulcrand, R.; Joly, L.; Ybert, C. *The Journal of Physical Chemistry Letters* **2017**, *8*, 478–483, PMID: 28067521.

[29] Karniadakis, G.; Beskok, A.; Aluru, N. In *Microflows and Nanoflows: Fundamentals and Simulation*; Antman, S., J.E., M., Sirovich, L., Eds.; Springer New York: 233 Spring Street, New York, NY 10013, USA, 2005; Vol. 29; pp 258–260.

[30] Huang, D. M.; Cottin-Bizonne, C. e.; Ybert, C.; Bocquet, L. e. *Langmuir* **2008**, *24*, 1442–1450, PMID: 18052395.

[31] Yoshida, H.; Marbach, S.; Bocquet, L. *The Journal of Chemical Physics* **2017**, *146*, 194702.

[32] van der Heyden, F. H. J.; Bonthuis, D. J.; Stein, D.; Meyer, C.; Dekker, C. *Nano Lett.* **2007**, *7*, 1022–1025, PMID: 17352506.

[33] Alizadeh, S.; Mani, A. *Langmuir* **2017**, *33*, 6205–6219, PMID: 28498669.

[34] Kedem, O.; Katchalsky, A. *Transactions of the Faraday Society* **1963**, *59*, 1918–1930.

[35] Chen, B.; Jiang, H.; Liu, X.; Hu, X. *ACS Applied Materials & Interfaces* **2017**, *9*, 22826–22836, PMID: 28640581.

[36] Celebi, K.; Buchheim, J.; Wyss, R. M.; Droudian, A.; Gasser, P.; Shorubalko, I.; Kye, J.-I.; Lee, C.; Park, H. G. *Science* **2014**, *344*, 289–292.

[37] Yan, Y.; Sheng, Q.; Wang, C.; Xue, J.; Chang, H.-C. *The Journal of Physical Chemistry C* **2013**, *117*, 8050–8061.

[38] Sahu, S.; Zwolak, M. *Physical Review E* **2018**, *98*, 012404.

[39] Kowalczyk, S. W.; Grosberg, A. Y.; Rabin, Y.; Dekker, C. *Nanotechnology* **2011**, *22*, 315101.

[40] Luan, B. *Nanotechnology* **2015**, *26*, 055502.

[41] Sampson, R. A. *Philosophical Transactions of the Royal Society of London A: Mathematical, Physical and Engineering Sciences* **1891**, *182*, 449–518.

[42] Daiguji, H. *Chemical Society Reviews* **2010**, *39*, 901–911.

[43] Joly, L. *The Journal of Chemical Physics* **2011**, *135*, 214705.

[44] Gravelle, S.; Joly, L.; Detcheverry, F.; Ybert, C.; Cottin-Bizonne, C.; Bocquet, L. *Proceedings of the National Academy of Sciences* **2013**, *110*, 16367–16372.

[45] Gravelle, S.; Joly, L.; Ybert, C.; Bocquet, L. *The Journal of Chemical Physics* **2014**, *141*, 18C526.

[46] Yoshida, H.; Bocquet, L. *J. Chem. Phys.* **2016**, *144*.

[47] Liu, L.; Nicholson, D.; Bhatia, S. K. *The Journal of Physical Chemistry C* **2016**, *120*, 26363–26373.

[48] Gravelle, S.; Yoshida, H.; Joly, L.; Ybert, C.; Bocquet, L. *The Journal of Chemical Physics* **2016**, *145*, 124708.

[49] Belin, C.; Joly, L.; Detcheverry, F. m. c. *Phys. Rev. Fluids* **2016**, *1*, 054103.

[50] Fu, L.; Merabia, S.; Joly, L. *Physical Review Letters* **2017**, *119*, 214501.

[51] Bocquet, L.; Charlaix, E. *Chemical Society Reviews* **2010**, *39*, 1073–1095.

[52] Sparreboom, W.; van den Berg, A.; Eijkel, J. C. T. *New Journal of Physics* **2010**, *12*, 015004.

[53] Im, W.; Roux, B. *Journal of Molecular Biology* **2002**, *322*, 851 – 869.

[54] Frenkel, D.; Smit, B. *Understanding Molecular Simulation*; Academic Press, 2002.

[55] Maginn, E. J.; Bell, A. T.; Theodorou, D. N. *The Journal of Physical Chemistry* **1993**, *97*, 4173–4181.

[56] Kalra, A.; Garde, S.; Hummer, G. *Proceedings of the National Academy of Sciences of the United States of America* **2003**, *100*, 10175–10180.

[57] Feng, J.; Graf, M.; Liu, K.; Ovchinnikov, D.; Dumcenco, D.; Heiranian, M.; Nandigana, V.; Aluru, N. R.; Kis, A.; Radenovic, A. *Nature* **2016**, *536*, 197–200.

[58] Heffelfinger, G. S.; Swol, F. v. *The Journal of Chemical Physics* **1994**, *100*, 7548–7552.

[59] Cracknell, R. F.; Nicholson, D.; Quirke, N. *Physical Review Letters* **1995**, *74*, 2463–2466.

[60] Kutzner, C.; Grubm uller, H.; de Groot, B.; Zachariae, U. *Biophysical Journal* **2011**, *101*, 809–817.

[61]Ható, Z.; Ákos Kaviczki,; Kristóf, T. *Molecular Simulation* **2016**, *42*, 71–80.

[62] Zheng, J.; Lennon, E. M.; Tsao, H.-K.; Sheng, Y.-J.; Jiang, S. *The Journal of Chemical Physics* **2005**, *122*, 214702.

[63] Ozcan, A.; Perego, C.; Salvalaglio, M.; Parrinello, M.; Yazaydin, O. *Chemical Science* **2017**, *8*, 3858–3865.

[64] Picallo, C. B.; Gravelle, S.; Joly, L.; Charlaix, E.; Bocquet, L. *Phys. Rev. Lett.* **2013**, *111*, 244501.

[65] Comsol 4.3a, http://www.comsol.com.

[66] Altalhi, T.; Kumeria, T.; Santos, A.; Losic, D. *Carbon* **2013**, *63*, 423–433.

[67] Gadaleta, A.; Sempere, C.; Gravelle, S.; Siria, A.; Fulcrand, R.; Ybert, C.; Bocquet, L. *Physics of Fluids* **2014**, *26*.

[68] Nosé, S. *Molecular Physics* **1984**, *100*, 191–198.

[69] Evans, D. J.; Morriss, G. P. *Physical Review Letters* **1986**, *56*, 2172–2175.

[70] Evans, D. J.; Morriss, G. P. *Statistical Mechanics of Nonequilibrium Liquids*; ANU Press, 2007.

[71] Bernardi, S.; Todd, B. D.; Searles, D. J. *The Journal of Chemical Physics* **2010**, *132*, 244706.

[72] http://www.moltemplate.org/.

[73] Stukowski, A. *Modelling and Simulation in Materials Science and Engineering* **2010**, *18*, 015012.

[74] Flyvbjerg, H.; Petersen, H. G. *The Journal of Chemical Physics* **1989**, *91*, 461–466.

[75] Khair, A. S.; Squires, T. M. *Journal of Fluid Mechanics* **2008**, *615*, 323–334.

[76] Yoshida, H.; Mizuno, H.; Kinjo, T.; Washizu, H.; Barrat, J.-L. *The Journal of Chemical Physics* **2014**, *140*, 214701.

[77] Losic, D.; Velleman, L.; Kant, K.; Kumeria, T.; Gulati, K.; Shapter, J. G.; Beattie, D. A.; Simovic, S. *Aust. J. Chem.* **2011**, *64*, 294–301.

[78] www.pardiso-project.org/.

[79] Wright, M. R. *An Introduction to Aqueous Electrolyte Solutions*; John Wiley & Sons, Ltd, 2007.

[80] Russell, T. W. F.; Hodgson, G. W.; Govier, G. W. *The Canadian Journal of Chemical Engineering* **1959**, *37*, 9–17.

[81] Samson, E.; Marchand, J.; Snyder, K. A. *Materials and Structures* **2003**, *36*, 156–165.

[82] Happel, J.; Brenner, H. In *Low Reynolds number hydrodynamics*; Moreau, R., Ed.; Martinus Nijhoff Publishers, 1983.

[83] Sherwood, J. D.; Stone, H. A. *Physics of Fluids* **1995**, *7*, 697–705.

[84] Logan, B. E.; Elimelech, M. *Nature* **2012**, *488*, 313–319.

[85] Plimpton, S. *The Journal of Computational Physics* **1995**, *117*, 1–19.

[86] Onsager, L. *Physical Review* **1931**, *37*, 405–426.

[87] Sisan, T.; Lichter, S. *Microfluidics and Nanofluidics* **2011**, *11*, 787–791.

[88] Tunuguntla, R. H.; Henley, R. Y.; Yao, Y.-C.; Pham, T. A.; Wanunu, M.; Noy, A. *Science* **2017**, *357*, 792–796.

[89] http://graal.ens-lyon.fr/MUMPS/.

[90] Morse, P. M.; Feshbach, H. *Methods in Theoretical Physics*; McGraw-Hill, 1953; Vol. 2, p1292.

[91] Garaj, S.; Hubbard, W.; Reina, A.; Kong, J.; Branton, D.; Golovchenko, J. A. *Nature* **2010**, *467*, 190–193.

[92] Zhang, J.; Hansen, J. S.; Todd, B. D.; Daivis, P. J. *The Journal of Chemical Physics* **2007**, *126*, 144907.

[93] Siria, A.; Bocquet, M.-L.; Bocquet, L. *Nature Reviews Chemistry* **2017**, *1*, 0091.